Hadron Spectra in Au+Au Collisions at the BNL AGS

By
Michael David Heffner
B.S. (Purdue University, West Lafayette) 1995
M.S. (University of California, Davis) 1996

DISSERTATION
Submitted in partial satisfaction of the requirements for the degree of
DOCTOR OF PHILOSOPHY
in
Physics
in the
OFFICE OF GRADUATE STUDIES
of the
UNIVERSITY OF CALIFORNIA
DAVIS

Approved:

Committee in Charge
2000

Michael David Heffner
September 2000
Physics

Hadron Spectra in Au+Au Collisions at the BNL AGS

Abstract

The E895 experiment at Brookhaven National Laboratory is the study of dense nuclear matter using nuclear collisions to generate hot dense fireballs of hadrons. Gold nuclei are collided in a fixed target experiment with beam energies of 1.85, 3.91, 6.0, and 8.0 AGeV. The unique nature of these accelerator experiments is that we have the opportunity to study the collisions in an environment where starting conditions, such as beam energy, are controlled. The hope is that these experiments will further our understanding of the nuclear forces that are currently well described by Quantum Chromodynamics (QCD). This knowledge could then be applied to understanding astrophysical objects such as neutron stars, supernovae, and even the origin of the universe itself (the big bang).

This dissertation describes one aspect of the nuclear collisions, namely radial flow. This is the collective motion of the fireball transverse to the beam direction. The EOS TPC is used to measure the mid-rapidity spectra for protons, pions and helions. These spectra are then fit to a simple thermal model to extract the temperature and expansion velocity of the system at last hard scattering, also known as freeze-out. It is found that the temperature is consistent with a leveling off or saturation in the energy range of this experiment, especially when compared with other experiments at lower energies.

Dedicated to my family

Acknowledgements

The nature of the work presented in this dissertation necessitates the work of collaborations, and therefore I would like to thank everyone in the E895 collaboration for their work on this experiment. I would especially like to acknowledge the people that helped me directly and provided an environment to develop as a scientist. Daniel Cebra, my graduate advisor, has spend many hours with me helping with the tough details of the analysis presented here, and has always kept a positive, ambitious attitude towards the work that has now paid off. I would also like to thank Jennifer Klay who has also been involved with this project from the beginning. Jenn has done a large amount of work for this project, and she has always been great to talk with about issues related to this topic. I would also like to thank my dissertation readers James Draper and Paul Brady. They have provided many comments on this work.

I would like to thank all of my friends and family for their support. I would especially like to thank my immediate family since they have provided endless encouragement since I was very young. Without their support I would have never made it this far. Thank you Matt, Mom and Dad. I would like to thank my grandmother, Katherine, for her enthusiasm and interest in my life. I would like to thank my girlfriend Caroline for being with me and withstanding the stress in the last few months. This has been the most stressful time of my graduate school experience, and she has really helped me out. THANK YOU ALL!

Contents

List of Figures

List of Tables

Chapter 1

Introduction to Heavy Ion Collisions

1.1 Motivation

The study of the atomic nucleus has most of its roots in the 20th century. One might say the the origin of nuclear physics is the discovery of radioactivity in 1896 by Becquerel, but Rutherford really set the idea of a nucleus on firm ground with his famous α particle scattering experiments in 1911[Ruth11]. Since this time, many details of the nucleus have been studied and understood[Kran88][Wong94]. We know the size and density of the nucleus, we know about the excited states, the spin, and have cataloged many of these properties. It would be fair to say that many of the properties of normal nuclear matter have been studied. This work is very interesting in itself, and it has been of general scientific benefit in a number of ways. A few examples to underline this point are our understanding of solar nucleosynthesis, the capability to build nuclear power reactors, and our ability to diagnose medical problems with isotope and NMRI imaging. All of these benefits come from the understanding that has been developed about the nucleus.

The work presented in this paper is focused on studying nuclear matter far from the normal state. Before the use of accelerators in the early 1980's to produce highly excited nuclear matter, much of the study focused on nuclear matter in the state that is close to that found naturally. There were many studies that would excite the matter by small amounts, but not much more than the binding energy ($\sim$8MeV). The latest accelerator experiments are now delivering to the collision region up to 2.68 to

4.27 GeV per nucleon at the AGS, over 17 GeV per nucleon at CERN, and the newest accelerator at RHIC[Harr98] will soon produce collisions with 200 GeV per nucleon in the center of mass. The densities are measured well above the normal nuclear density[Petr95]. The central densities for head on collisions have been estimated to be 6-8 ρ_0 (where ρ_0 is the normal nuclear density) at the AGS[Dani98][Li96][Kaha96] and 20-30 ρ_0 [Jaco00] [Albe95]at CERN. This is certainly far from the ground state of the stable nuclear matter.

Matter in this dense state is interesting for a number of reasons. First it is simply interesting to study a system in a state that has not been explored. Quantum Chromodynamics (QCD) is a successful field theory that describes the interaction of the quarks that make up nucleons; the nucleons are the constituents of the nuclei. With QCD, one could in principle compute the properties of nuclear matter. QCD does makes some predictions, at low baryon density, about how matter will behave under these extreme conditions, but until it is measured we can't really know whether there will be any surprises. Studying these hot dense nuclear states will allow us to test QCD in conditions that have before been unavailable. Furthermore it is speculated that the nuclear matter could undergo a phase transition in to a quark-gluon plasma[Sing93]. This could have implications for how we think about astrophysical objects, and even the universe itself. It is thought that the centers of neutron stars and supernova reach high densities as a result of the gravitational pressure[Cser94].

Although the exact conditions are different, possibly some information about these objects can be gleaned from the study of accelerator-produced matter. For those that believe that there was a Big Bang, this study has special importance. It is thought that normal nuclear matter would have to be in a quark-gluon state in the first few μ seconds[Wein93]. Studying this in the lab could give us more information about the origin of the universe.

1.2 Quark-Gluon Plasma

We know from observation that the nucleons that make up the nucleus are composed of quarks held together by gluons. Also from observation it is found that quarks form hadrons from either a quark anti-quark pair or 3 quarks, but no other combination (at least at the valence level; there also exists sea quarks in the hadrons). When one tries to pull two quarks apart, the energy becomes large enough that the bond breaks producing a quark anti-quark pair from the vacuum. This idea that a single quark can not be isolated is called confinement. The question that arises is what happens if a number of nucleons are pushed together so they are overlapping. It is commonly believed that if the pressure is high enough, the quarks will start to interact with the quarks of the other hadrons as they would with the hadron that they belong to. The hadron bags would dissolve, and the group of quarks would freely interact within the high density region. This type of quark deconfinement is called a

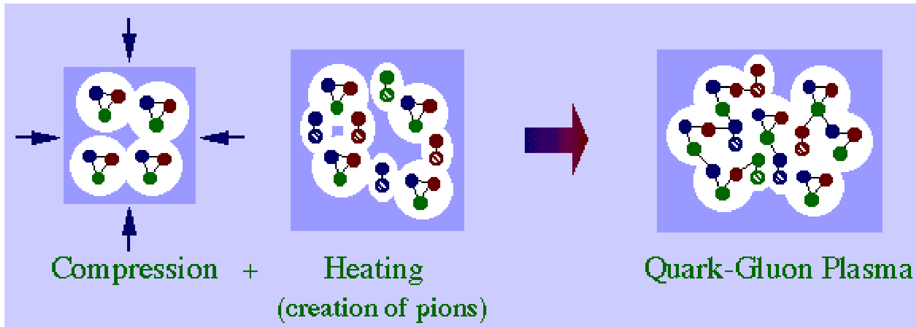

Figure 1.1: Phase transition in nuclear matter. The left-most picture shows the individual nucleons in the nucleus, each with three quarks. In the next slide they are heated and compressed. Pions are created in the process as the energy density increases. Lastly, with enough heating and compression the individual hadrons dissolve into a QGP.

quark-gluon plasma(QGP)[Sing93]. Figure 1.1 shows a cartoon of this process.

In simple terms, a quark-gluon plasma is simply a different phase of nuclear matter, as steam is a different phase of water. Heated and/or compressed nuclear matter becomes a quark-gluon plasma when the constituent quarks are deconfined and free to interact directly with other quarks in the plasma. A phase diagram of nuclear matter should look something like Fig.1.2. Common nuclear matter would be at densities where $\rho/\rho_0 = 1$, and a temperature essentially zero on this diagram. Moving up in temperature the nucleons gain enough energy that the bonds are broken by collisions and a hadron gas is formed. The gas also has other non-nucleon hadrons that are formed from the vacuum when the energy density or temperature is high enough. This transition from a liquid-like nucleus to a gas like phase is analogous to the liquid/gas phase transition. Further heating or compression will move the matter into the QGP.

This transition is not well understood, and the recent analysis from the CERN-SPS program has only suggested that it exists[Jaco00].

The analysis and interpretation is complicated for many reasons. The fireballs generated in the collisions are on the order of the nuclear diameter. The size limits the ability to observe the collision, but even more fundamentally problematic is that the finite size of the system makes the idea of equilibration, and phase transitions unclear. One normally thinks of roughly Avogadro's number of particles in the system, but here we have only a few hundred to a few thousand in the most energetic systems. The lifetimes are also rather short, on the order of a few to tens of fm/c. This again limits the ability to reach equilibrium, but amazingly some equilibrium is reached. Quantum Chromodynamics QCD describes the nuclear forces rather well, but complications arise in the calculations from the high baryon density in the collision for AGS and SPS results. The RHIC results should be easier to interpret with QCD due to the expected low baryon density. Also difficult for the theorists to model is the so called "hadronization". This is the process through which the QGP cools and returns to normal matter. Our detectors see the hadrons after hadronization, and therefore, first the hadronization must be understood before one can start to study the processes that come before it.

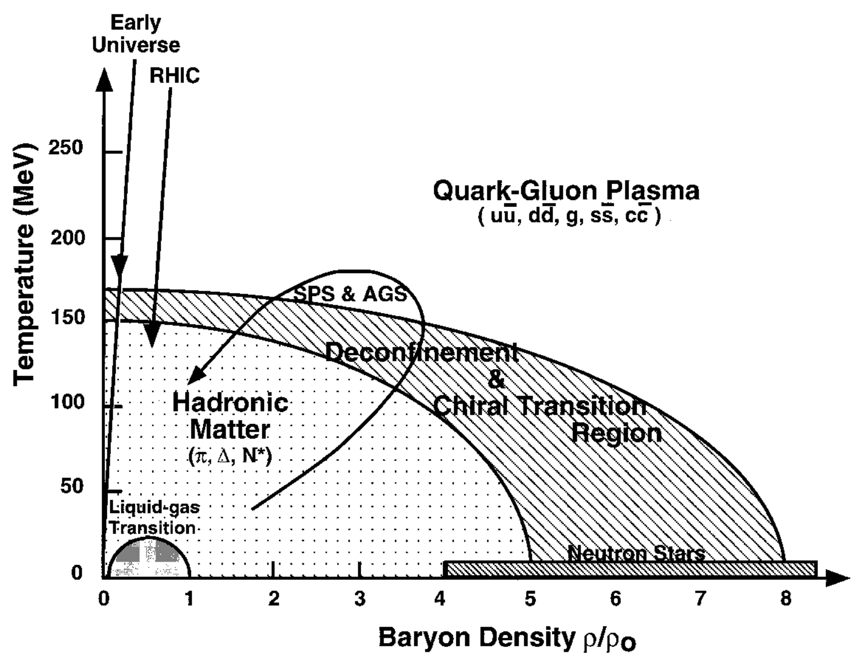

Figure 1.2: The phase diagram for excited nuclear matter.[Harr98] Common nuclear matter in the atoms that make up our world would be at ρ/ρ_0 of 1 and a temperature of about zero on this plot. Roughly where the paths of cooling nuclear matter from the early universe, and from various accelerator experiments are shown. It is still a matter of debate whether the SPS and AGS accelerators cross into the QGP phase.

1.3 Hadron Spectra

Hadron momentum spectra are one method to study the nuclear collisions. One measures the momentum and species of particles from the collision and summarizes the distributions typically in histograms. The shape of the distribution has information about the temperature of the collision at the last hard scattering, and the collective motion of the particles leaving the collision region, also called flow. This observable allows one to measure the final state of the expansion of the fire ball that is produced in the collision. This is further discussed in Chapter 6. Integrating the distributions gives the total number of particles, and this can be used to estimate the energy and, given the collision volume, the energy density reached in the collision.

Chapter 2

The E895 Experiment

2.1 The AGS accelerator

The Alternating Gradient Synchrotron(AGS) is a machine capable of producing heavy ions at large kinetic energy. Ions are injected into the accelerator from smaller accelerators that have already fully stripped the electrons from the atoms. The ions are accelerated in electric fields within the accelerator and magnets are placed around the beam to cause the beam to travel in a 250m diameter circle. As the nuclei travel around the accelerator they are accelerated until the required kinetic energy is obtained. They are then kicked from the accelerator ring to be delivered to the experiments as shown in Fig.2.1. This accelerator is located at Brookhaven National Lab(BNL) on Long Island, and can produce ^{197}Au nuclei with a maximum kinetic energy of 10.8 AGeV. In the E895 experiment, Au beams of 2, 4, 6, 8 AGeV were produced at a rate of $\sim$10 spills/min with about 1000 particles/spill.

2.2 The Target

The target is the piece of material, that contains the nuclei, that the accelerated gold nuclei collide with to produce the dense nuclear matter. In the case of the E895 experiment, gold was the primary target. Small data samples with copper, silver and beryllium were also taken in the experiment. The target is thin enough that the beam from the accelerator impinges one side of the target, and the resulting fragments from

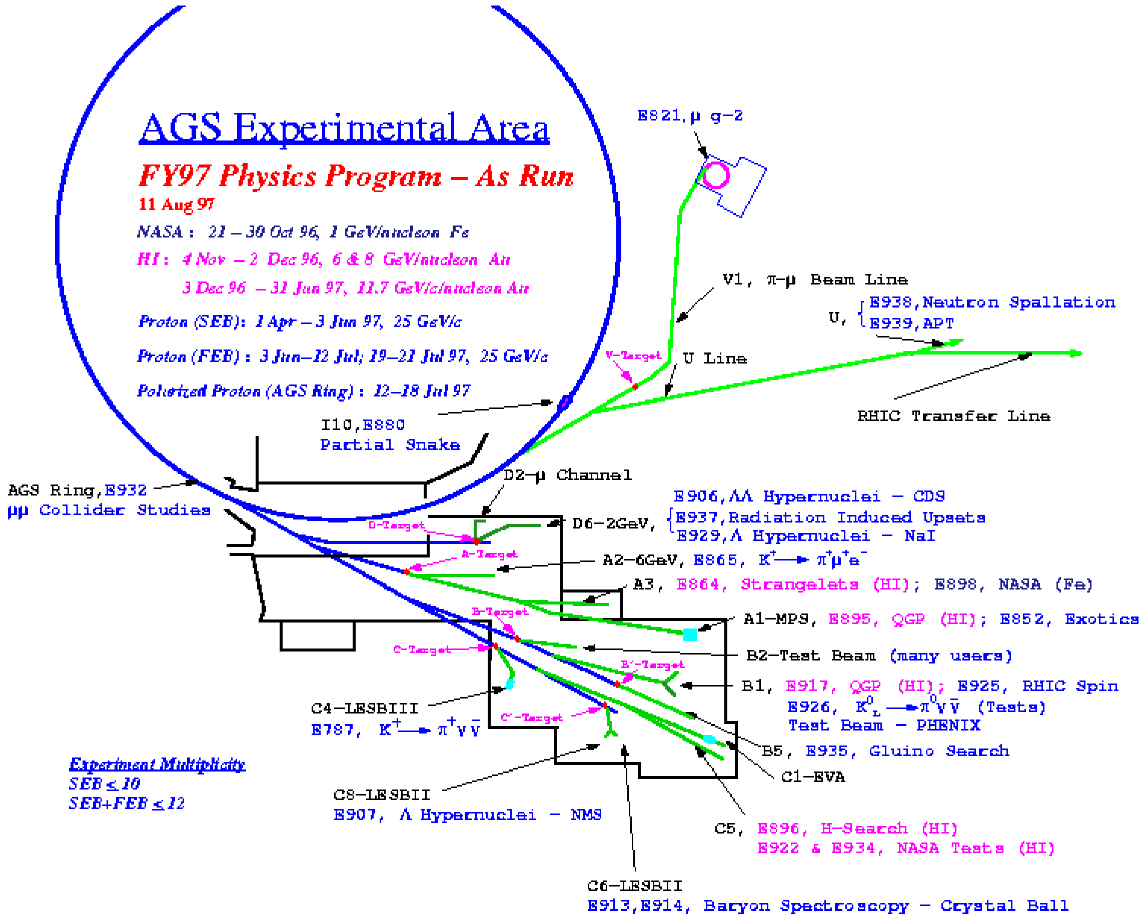

Figure 2.1: The AGS accelerator complex. If you look closely, you can see the E895 experiment on the A-1 beam line.

a collision emanate from the other side. Three thickness were used for the gold targets, 10mil, 20mil, and 30mil. The probability of an incoming gold nucleus colliding with a nucleus in the target was 0.93%, 1.86%, and 2.79% respectively. The choice of target thickness is a balance between getting enough interactions and having more than one reaction. In addition, interactions between the target and the products of a collision degrade the measurement of collision products, and therefore compel one to keep the target as thin as possible. The data sets with a beam energy of 2 A-GeV ran with the 20mil target and the other energies ran with the 30mil target.

2.3 The detector

When a gold nucleus from the accelerator beam collides with a nucleus in the target the result is hundreds of particles exiting the target. The purpose of the detector is to measure the results of the collision, by measuring properties of the outgoing particles. The detector in the E895 experiment consists of sub-detectors that each give information about the collision. The multi-purpose nature of the detector allows for a number of experiments[Lisa00][Pink99][Liu00].

2.3.1 Trigger

The trigger is the hardware and software that is used to determine whether a desired event has occurred. The need for the trigger arises from the fact that most of the incoming beam doesn't react with the target, and that the TPC requires a signal to read out the contents. In addition, the trigger can preselect events to make the data processing more efficient. The most important tuning of the trigger is for the selection of events based on the impact parameter. The details of the impact parameter are discussed in section 3.4.

The trigger hardware consists of a number of scintillators and the associated photo tubes to collect the emitted photons. The arrangement is shown in Fig. 2.2. The beam of ^{197}Au nuclei enters the experiment from the right indicated by the dotted line. The first set of four scintillators determines whether there is a good beam particle. S1 and S2 should give a signal and V1 and V2 should not if the beam particle is traveling in the correct direction and has not fragmented in any of the part of the beam delivery system. The ^{197}Au then collides with the target. The ST scintillator located shortly after the target determines whether the incoming beam has interacted with the target. ST operates on the basis that the amount of scintillator light produced is roughly proportional to the amount of energy deposited in the material, and the energy deposited for relativistic particles is roughly proportional to the sum of charge squared(Z^2) of the particles that are passing through. A simple example to see how is works is as follows. The energy deposit for a uninteracted ^{197}Au is 79^2 or 6241 in some units. For the same nucleus broken into two pieces one would get an energy output of say 40^2+39^2 or 3121, about half the light output. Further breakup lowers the light

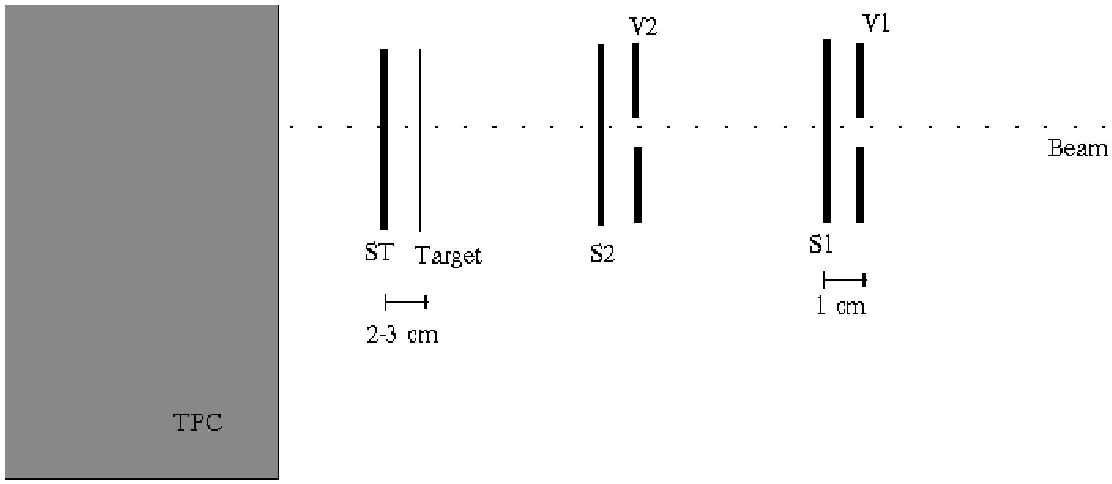

Figure 2.2: Detail of the trigger setup. The solid vertical lines represent scintillator paddles placed in the path of the gold beam. The paddles labeled with an S (S1,S2,ST) flash when a gold nucleus passes through. The paddles labeled with a V(V1,V2) have a hole in the middle so that a nucleus on the correct path will not make a signal in these paddles. The relative location of the target and TPC are also shown. Not to scale.

output. The magnitude of the light output of ST effectively allows one to not only determine whether a gold beam interacted, but also allows approximate but quick determination of the centrality of the collision. The more central the collision, the more fragments are expected and the lower the light output level. The signals from the scintillators are quickly read out and a logic circuit determines whether a desired interaction occurred. The logic circuit output is then used to determine whether the TPC should write the event to tape.

2.3.2 TPC

The Time Projection Chamber(TPC) is the centerpiece of the experiment. This gas detector measures the density and location (in 3 dimensions) of the ionization tracks of charged particles that pass through its 150cm X 96cm X 75cm active volume. The TPC was built originally for the EOS[Rai90] experiment at Lawrence Berkeley National Lab (LBNL), and later shipped to Brookhaven National Lab (BNL) where the E895 experiment took place. The TPC was placed between the pole tips of the Multi-Particle Spectrometer(MPS) magnet that provided up to a 1 Tesla field. The curvature of the tracks in the magnet field and the intensity of the ionizations allows one to determine the momentum and species of each particle that passes through the active volume. Figure 2.3 shows a sectioned view of this detector.

The active volume of the TPC starts 13cm directly behind the target and measures the majority of particles produced from the collisions in the target. The kinematics of the collision are such that most of the products of the collision are carried forward allowing the TPC to "see" most of the particles.

2.3.2.1 Gas Ionization

The TPC "sees" particles passing through it by the electromagnetic interactions of the charged particle with the gas atoms in the TPC. The typical interaction in a gas at STP is ionization of the gas atoms that are near the path of the charged

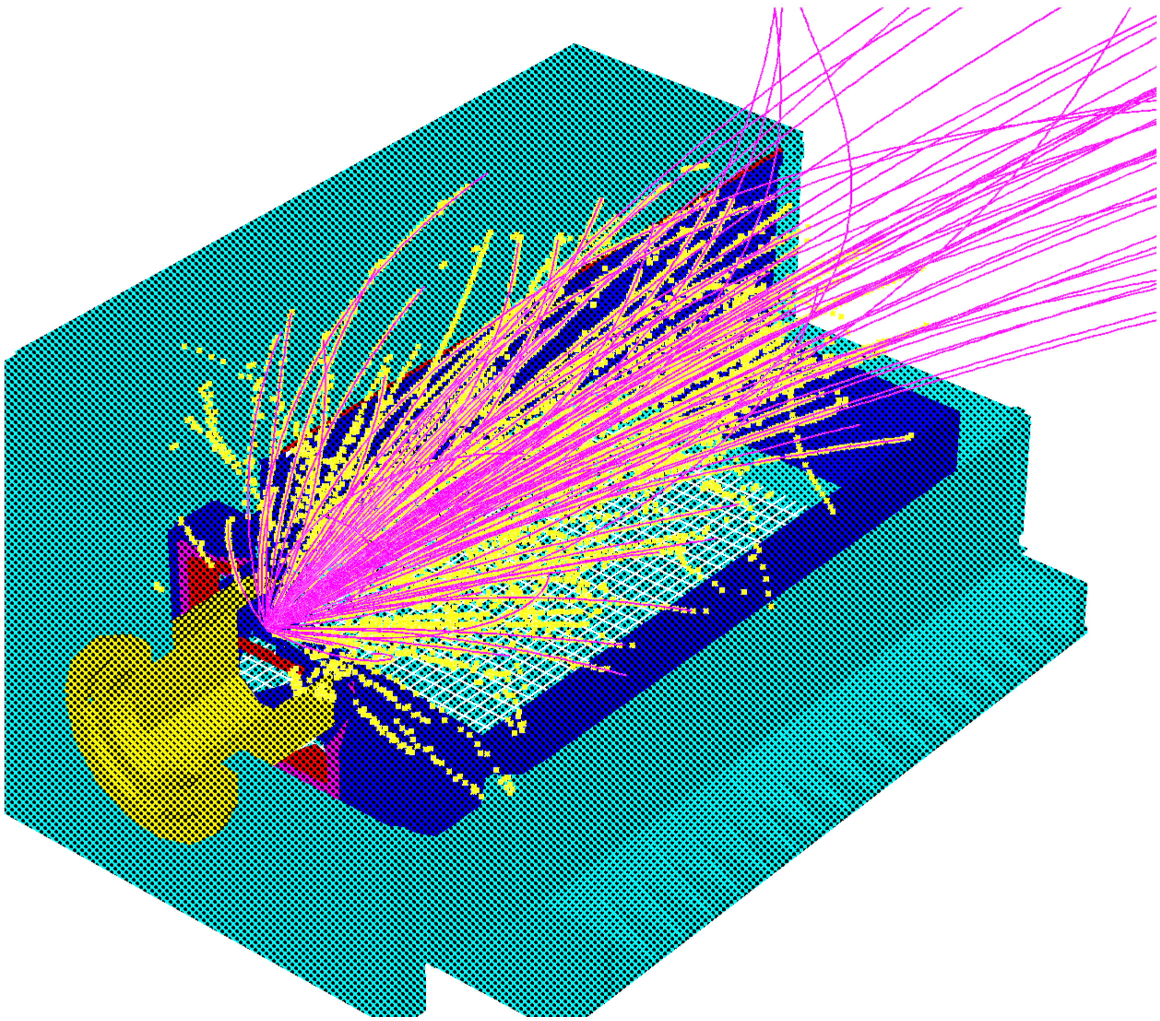

Figure 2.3: Sectional view of the EOS TPC. The target is in the middle of the left side facing you. The crosses show hits found by the hit finder, and the lines are the tracks found by the tracker.

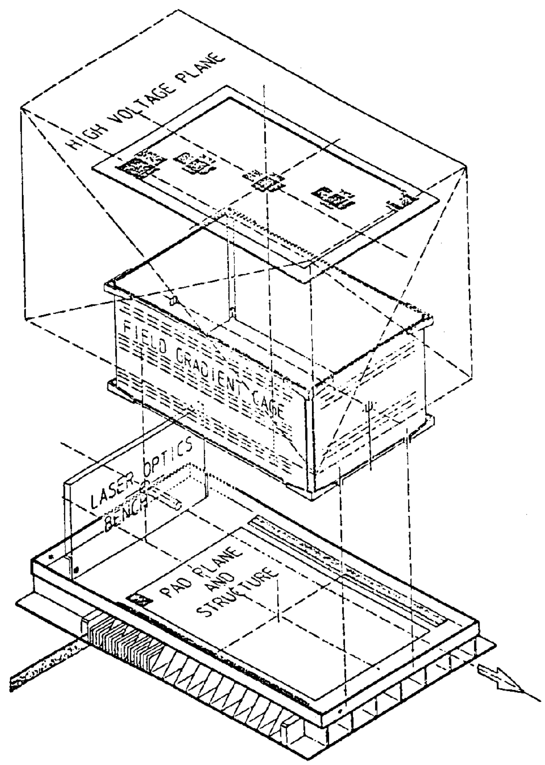

Figure 2.4: An exploded view of the EOS TPC.[Rai90] The pad plane, laser table, field cage, high voltage plane, and gas enclosure can all be clearly seen in this view.

particle. This ionization, also known as dE/dx, is well understood and explained in many text books[Fern92][Leo94]. The term dE/dx refers to the specific energy loss (energy loss per length). Any gas will produce tracks of ionization with the passage of a charged particle, but some gases have better properties than others. For example, gases such as oxygen and water vapor are very undesirable as they have a high affinity for electrons. These gases will ionize, but the resulting electrons are quickly reabsorbed before they can be drifted, amplified and detected. Even small amounts of such gases can seriously reduce the signal. Noble gases are desired for their low working voltage in the ionization amplification that occurs in the wire chamber section of the TPC, see 2.3.2.3. Argon is popular because of low cost and high specific ionization potential[Leo94]. The gas used in this detector is P10, a mixture of 90% argon(Ar) and 10% methane(CH_4). The purpose of the methane is also for the charge amplification and is also explained in 2.3.2.3

2.3.2.2 The field cage and Electron Drift in electric and Magnetic fields

After a charged particle has passed through the P10 and left a track, it must be detected. This is done with a wire chamber that is described below. In order for the wire chamber to measure the ionization, the ionization must be moved from the active gas volume of the TPC to the entrance of the wire chamber. This is accomplished with an electric field that separates the electrons from the ions and starts the electrons drifting in the direction of the wire chamber. The wire chamber is located at the bottom of the TPC, and the electrons (not the positive ions) need to move or "drift" in that direction. This requires an $\overrightarrow{E}$ field pointing in the upward direction. The $125V/cm\overrightarrow{E}$ field is generated with a 10kV potential difference set up between the top of the TPC and the ground grid plane of the wire chamber. A field cage is needed around the remaining four sides of the detector to keep the field lines straight in the vertical direction. The field cage consists of copper strips on a kapton backing. The copper strips are oriented horizontally and are connected with a resistor chain that steps down the potential of each successive strip.

The magnetic field is oriented in the same direction as the electric field. This effects the drift by reducing the diffusion of an electron cloud in the direction transverse to the drift direction.

2.3.2.3 Wire chamber (with pad readout)

The wire chamber at the bottom of the TPC consists of four parallel planes. In Fig. 2.5 the ionizing track is shown with the the path of the drifting electrons. The Gating Grid is the entrance of the wire chamber. The purpose of this wire grid is to act as a window that can be open or shut to the incoming electrons. In the open configuration the wires are set to a potential that is equal the potential they would have if the grid were not there. In the closed configuration, the wires are set to alternating potentials that cause the field lines to terminate on the Gating Grid, and the electrons are then carried off by the power supply. The electric field lines of the entire wire chamber are shown in both open and closed configuration in Fig. 2.6.

The next grid in the wire chamber is the Ground Grid. As the name implies, these wires are at ground potential. This grid separates the large drifting region above from the amplification region below. This plane helps keeps the field lines in the drift region straight, and contains the positive ions that are generated in the amplification region.

The anode/sense wires are where the amplification occurs. We need amplification before we can detect the electrons because there are only about 48 electrons per cm of track from the initial track ionization of a typical track. The anode wires are very small in diameter (typically about $20\mu m$), and in the case of the EOS TPC are at a potential of about +1170 volts. This configuration produces a 1/r field near the wire, and because of the small wire diameter, there is a very large electric field near the surface of the wire. As the electrons drift towards the wire they gain momentum, and within a few wire diameters they have enough momentum to start to ionize the gas in a avalanche fashion. This avalanche in the EOS TPC was designed to produce a gain of 3000, and the resulting number of ion pairs should be proportional to the number of incoming electrons. In the space between the anode wires there are larger diameter field wires. The purpose of these wires is to shape the field, lower the anode voltages, and lessen the crosstalk between neighboring anode wires.

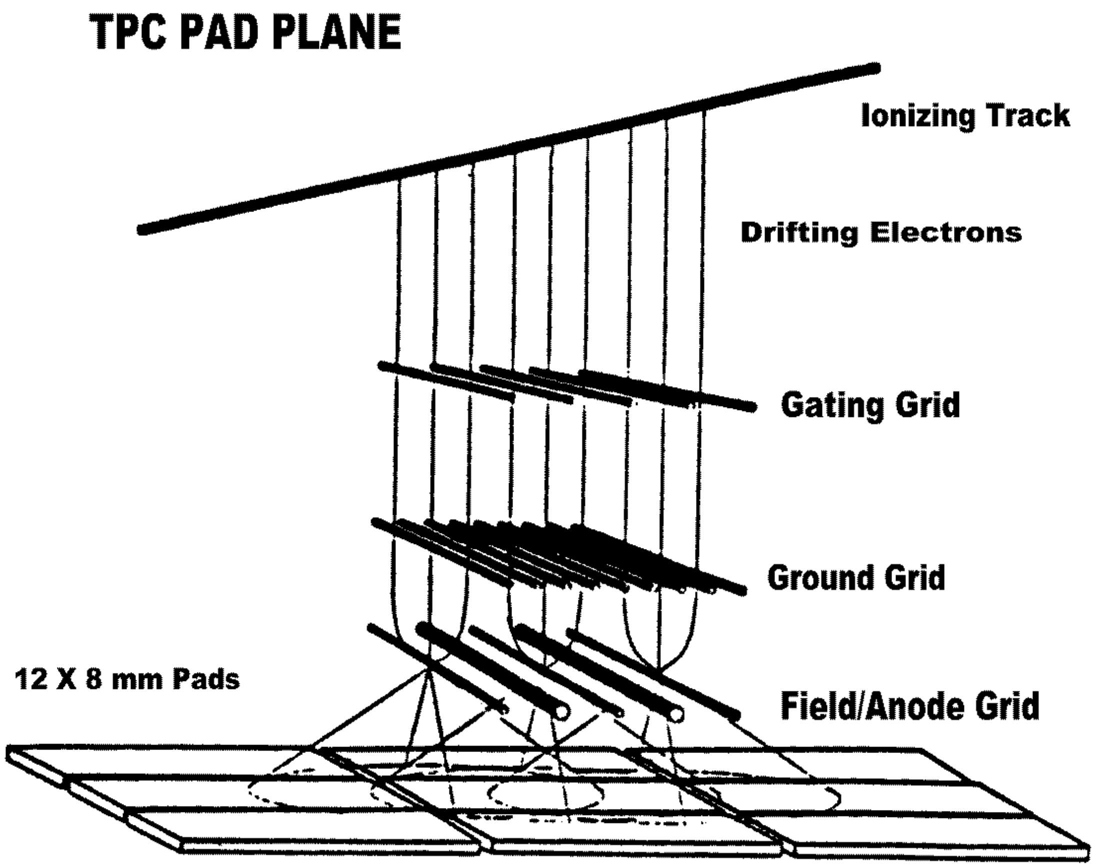

Figure 2.5: Enlarged picture of the wire chamber in the EOS TPC. The wire chamber is where the drifting electrons from the ionizing track are amplified for the electronics attached to the pads (the tiled structure on the bottom).

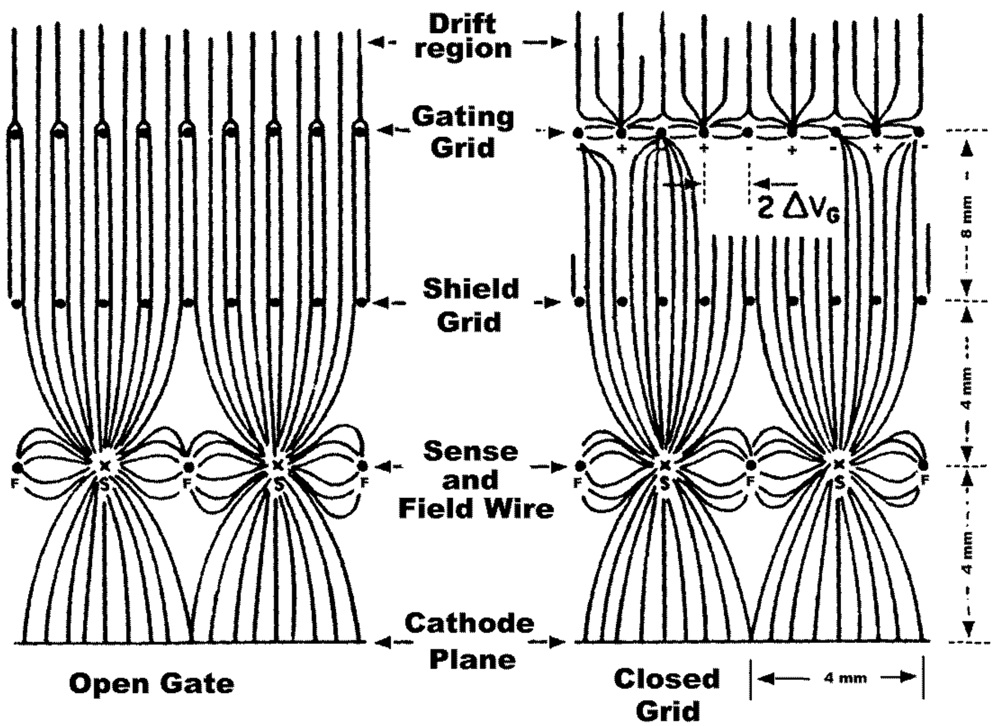

Figure 2.6: Picture of the field lines in the wire chamber in the two gating grid configurations.

Now that the number of electrons has been amplified by 3000 times, the signal can be read out as soon as the neutralizing positive ions begin to move up. This is accomplished with the fourth plane in the wire chamber. The Pad Plane consists of epoxy circuit board with copper pads on the surface, see Fig. 2.5. These pads are also at ground potential similar to the Ground Grid. They are inductively connected to the charges produced at the wires because of their proximity, and therefore have a signal that is pixelized over the entire surface of the wire chamber. The majority of the pad signal is from the relatively slow movement of the positive ions that drift up to the Ground Grid. The result is a pad signal of about 9231 electrons for the original 48 electrons/cm from a track. A nice summary of the pad signal is in Table 2.1.

The avalanche near the anode wire produces a large amount of excited argon that emits photons. These photons can then hit the cathode and produce many more electrons. This effect limits the gain in pure argon to about 10^3-10^4. The addition of a polyatomic molecules such as methane has the effect of quenching the gas by absorbing the photons and dissipating the energy by elastic collisions.

The signal on the pad is then processed as shown in Fig. 2.7. Each pad is connected electrically to its own preamp located below the wire chamber. The signal is then shaped and stored in switched capacitor arrays(sca). When a signal to take data arrives from the trigger electronics, the data in the sca's are encoded into an

Pad Signal for a Centered Minimum Ionizing Particle	
dE/dx (eV/cm)	1250
Pad Length (cm)	1.2
Energy Loss / Ion Pair (eV)	26
Gas Gain	3000
Efficiency of Charge Collection Due to the Integration Time	0.4
Wire-Pad Coupling	0.16
Total Pad Signal (electrons)	11000

Table 2.1: Pad signal for a typical track[Rai90]. This table details the performance and specs of the wire chamber.

optical fiber and sent to the counting house where the data are decoded and written to tape.

2.3.2.4 Laser Calibration

The magnetic field lines have noticeable bend due to the relative size of the pole tips and the gap between them. This has the effect of changing the path of the drifting electrons and distorting the reconstruction of the tracks. The build up of space charge and mechanical misalignments could also distort the reconstruction. The purpose of a laser calibration is to determine the distortions and therefore allow for spatial corrections to be made during the reconstruction. The 266nm laser light ionizes the gas in a straight line since it is not effected by the magnetic field. Reconstructing the tracks and looking for curvature in the tracks allows one to see the distortions and take corrective action.

The laser system also allows one to measure the drift velocity of the electrons in

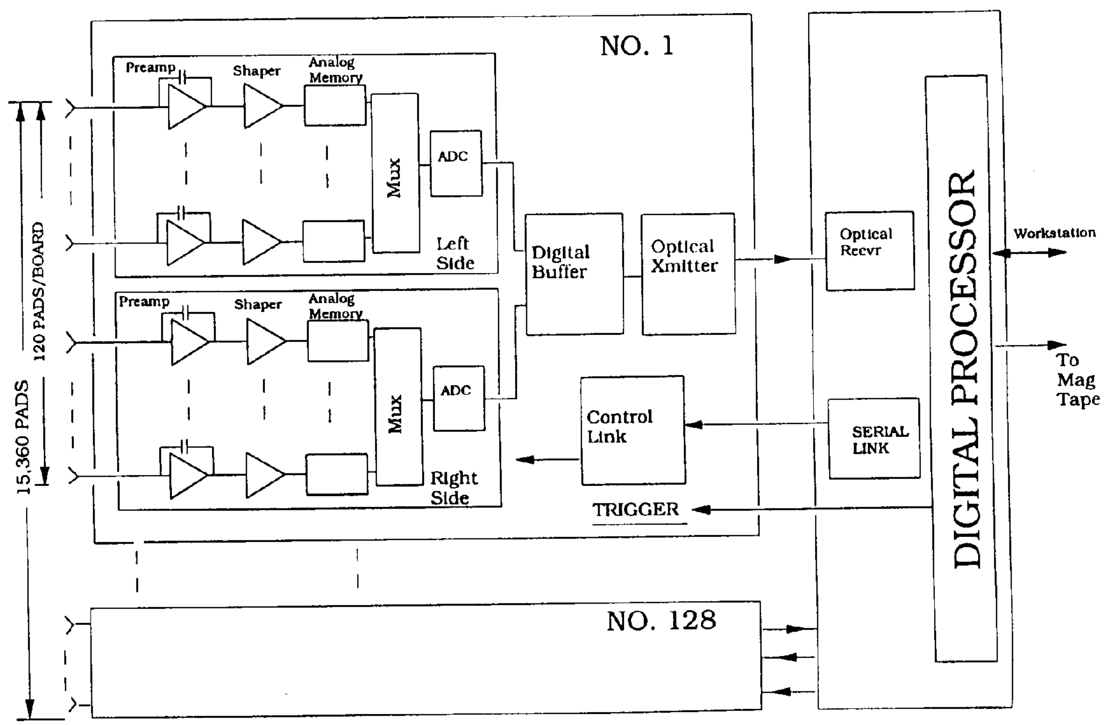

Figure 2.7: Block diagram of the TPC front end electronics[Rai90][Naka91]. The signals from the pads enter from the left into preamp/shapers. The signals are then stored in the analog memory, also known as bucket brigades or switch capacitor arrays. When a signal to take data is made, the analog memory is read out through the multiplexer and analog to digital converter (ADC). The digital signal is encoded into a optical fiber that runs to the counting house to be decoded and recorded to tape.

the gas. A laser event has only a few tracks, from 2 to about 6, and the positions are well known. This allows one to calculate the time from the laser pulse to the detection of electrons in the wire chamber. From this drift time and the known positions of the lasers, one can calculate the drift velocity. The drift velocity is important for the reconstruction of tracks. The position of tracks in the z-direction is determined by the time of arrival at the wire chamber times the drift velocity.

2.3.3 Canary

The canary is a dedicated device (similar to the TPC but smaller) to measure the drift velocity and attenuation of electrons in the gas. Gas from the TPC is continuously replaced. Some of the exhaust gas was diverted to the canary for analysis. In drift velocity mode, a 337nm nitrogen laser illuminated the top of the field cage and the wire chamber in the canary. Through the photo-electric effect electrons were produced on the metal surfaces. The electrons from the top of the field cage drifted to the bottom where the wire chamber detected the arrival. This setup produces two signals: first the prompt signal from the laser light hitting the wire chamber, and second from the drifting electrons. The time difference is the time to drift. Dividing the drift time by the distance gave us the velocity. The result of this is a plot of the drift velocity over time shown in Fig. 2.8.

The canary is also capable of measuring the attenuation of electrons in the gas.

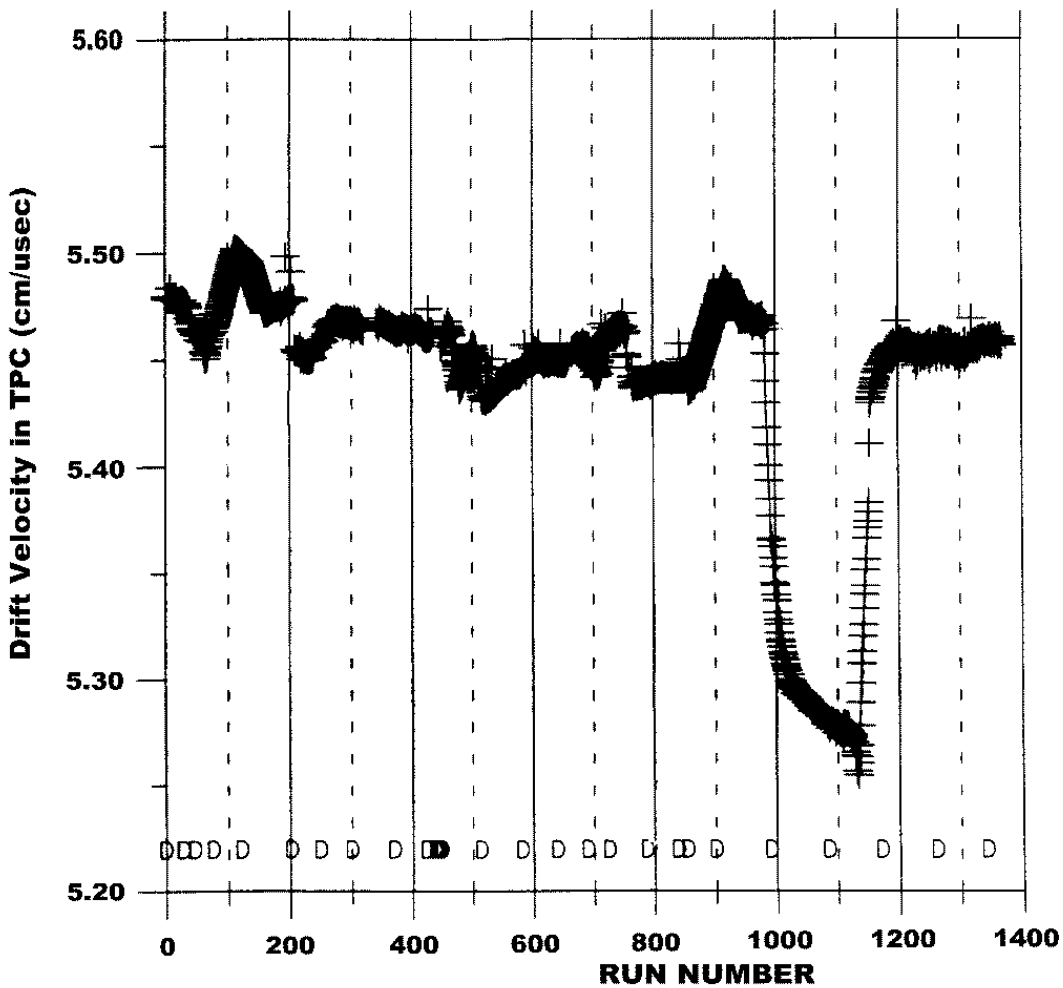

Figure 2.8: Drift velocity vs. run number from the canary. This plot produced by Jim Draper, shows the drift velocity measured by the canary as a function of run number(time).

The attenuation is due mostly to contamination of the gas with either O_2 or H_2O. Either of these gases will trap the drifting electrons before they reach the wire chamber at the bottom. The canary could measure this with the use of an electron source ^{109}Cd. By placing the source at different heights in the field cage and looking at the relative change in the signal at the wire chamber the attenuation can be computed.

Chapter 3

Basic Data Processing

The result of data collection is magnetic tape with the raw pixelized information about ionization in the TPC, trigger information, canary information, etc... The data contains the information about the tracks that passed through it, but not in an easily accessible format. The goal of basic data processing is to summarize this information so that it can later be accessed in a reasonable way for the more advanced physics analysis. The hit finding and tracking described below represent a large computing task that was run on computer farms at a number of the collaborator locations.

3.1 Hit finding

The ionizing track that passes through the TPC generates small clouds of electrons in its path. These clouds are the physical objects that drift in the TPC, and they have some spatial size. When a cloud reaches the wire chamber it generally falls over a few pads, and extends a few time buckets in the drift direction. The ionization in each of the 3-dimensional pixels (2-d pads (z,x), time (y)) is recorded, and thus the cloud is recorded digitally. A collection of contiguous pixels with ionization from a cloud is called a cluster. A hit is the center of gravity of the cluster (a coordinate in three space) and the energy deposited in the cluster (dE). It has no spatial size, and represents the most probable location of the path of the particle that produced the cluster. A software module called the Hit Finder computes a hit for every cluster in each event for all events.

In the simplest case an ionization cloud generated from one track drifts to the wire chamber and induces charge on a few pads. The hit finder simply identifies the cluster, and then computes its center and the total size using the amplitude information on pads. A more difficult but common situation is where two tracks cross and a cluster is generated from the sum of the ionization of both. The hit finder must recognize this situation and deconvolute the cluster to assign the two hits from the one cluster.

3.2 Tracking

Once we have the hits, the tracks are constructed with a software module called the Tracker. The problem of tracking is a specific case of a more general problem of pattern recognition [Bock90]. The Kalmann Filter[Bock90] idea was used in the tracking algorithm. The basic idea is that the tracker takes combinations of the hits in the last few rows of the TPC and projects back to the target using a helix model. It then looks for other hits that may belong to the track. If there is high probability that it belongs, then it is added. The track is then reprojected and the process repeats until the track is complete or there are no more hits. Once all of the hits are assigned to the track, the rigidity(r) of the track can be calculated from the curvature(ρ) of the track and the magnitude of the magnetic field(B).

$$r = \rho B \tag{3.1}$$

The specific energy loss (dE/dx) is also computed in this stage. The energy in each hit is stored with the hit, so all that has to be done is add up the energy from all the hits on the track and divide by the length of the track. There is one complication. The distribution of energy in an interaction with the gas follows a Landau distribution. The average of this distribution is not well defined, and therefore the average mentioned above will not work. The solution was to truncate the distribution by removing the top 20%, and averaging the remaining hits.

3.3 Vertexing

Once we have all of the tracks reconstructed, a vertex can be calculated that is consistent with the observed tracks. This is accomplished with a least squares fit to a linear track model in the area of the expected target. This important step allows one to determine where the interaction originated and what tracks came from it. The trigger can not determine where the interaction occurred. It could, for example, occur in the ST scintillator that is designed to detect the collision in the target.

The other important information from the vertexing is the distance of closest approach (dca). The dca is the closest distance from a reconstructed track to the vertex when a track is projected back towards the target. This parameter has a value for each track in an event and it allows a determination of what tracks are from the Au+Au collision and which tracks are likely from other background. A typical dca distribution, see Fig. 3.1, is peaked around zero as one would expect, and a value of 2.5 cm was chosen as a cut off for good tracks for the analysis in this work.

3.4 Impact Parameter

The impact parameter is the distance between the centers of the gold nuclei projected in the direction perpendicular to the velocity vector of the beam. Figure 3.2 shows a cartoon of the collision illustrating the impact parameter. In this experiment we do not have control of the impact parameter, nor can we measure it directly. We rely on the monotonic relationship of the event multiplicity to the impact parameter. A more central collision (smaller impact parameter) will produce higher multiplicity.

The first step in computing the relationship between the impact parameter and multiplicity is to determine the total cross section of the trigger setting. The inelastic cross section of two gold nuclei is a fixed number, but since the experiment is triggered by the target scintillator we don't see the entire cross section. By setting the target scintillator window lower the cross section becomes smaller, and the centrality of the events become greater. Information from the trigger allows one to compute the cross section.

The number of beam particles that enter the experiment is counted by the scintillator S1. This information is stored in scalers along with the number of good event triggers (scalers 8 and 6 for 2-4AGeV and scalers 9 and 4 for 6-8 AGeV). Using Equa-

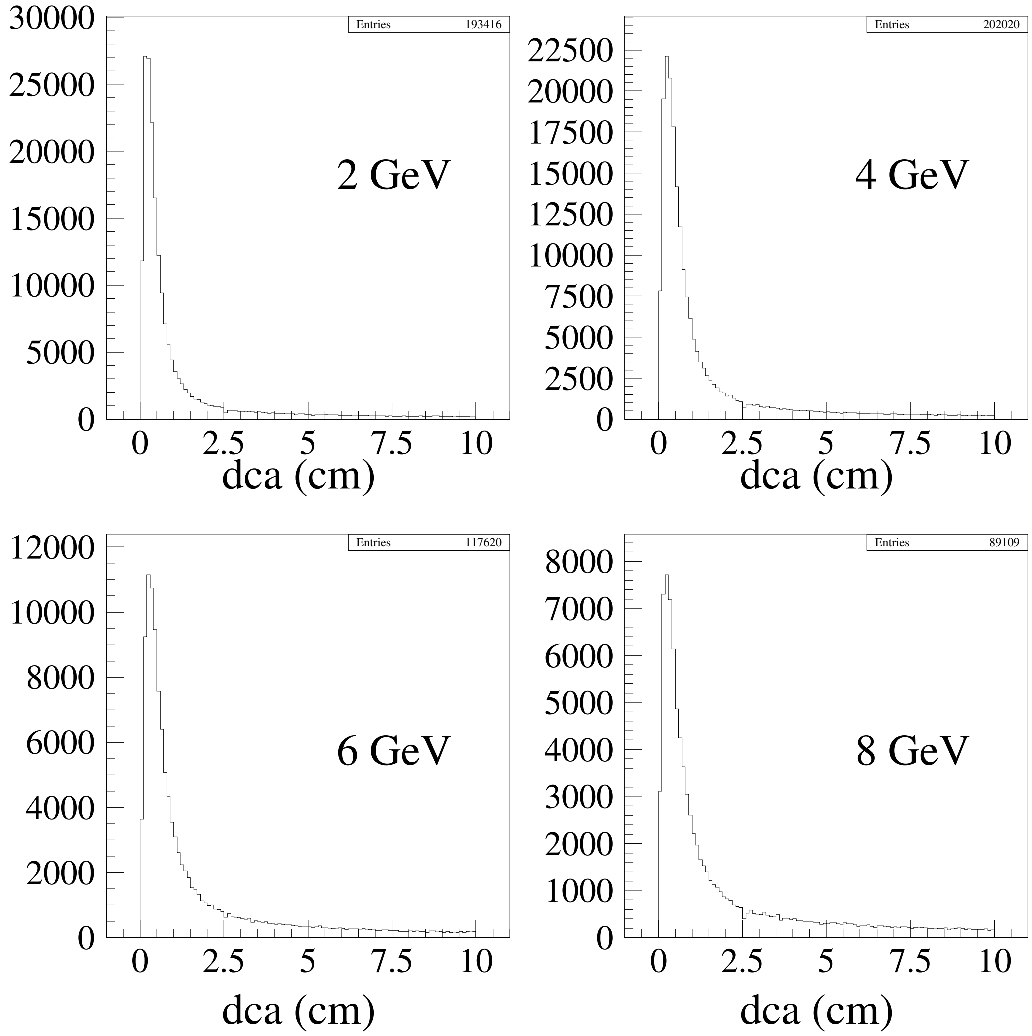

Figure 3.1: Typical distance of closest approach (dca) to the vertex distributions. After a main vertex is computed from the tracks in a given event, the distance of each track to the found vertex it computed. This number is used to select good tracks that came from the vertex.

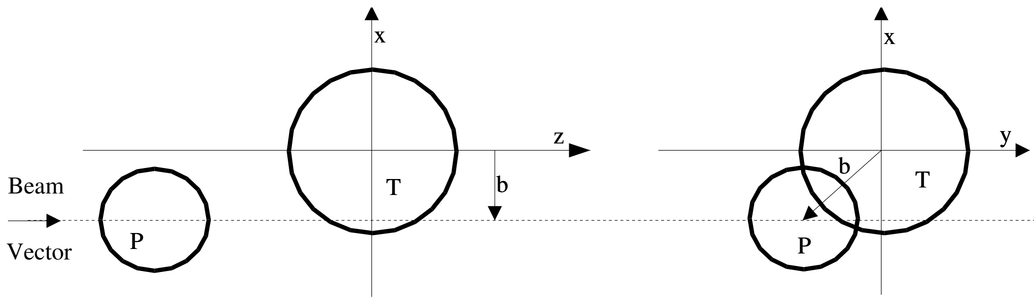

Figure 3.2: The impact parameter $\vec{b}$ is defined as the two dimensional vector in the x y plane, pointing from the center of the target(T) to the center of the projectile(P). This cartoon shows the impact parameter for a peripheral collision.

tion 3.2, the properties of the target, and the numbers stored in the scalers, the cross section is computed.

$$\sigma = \frac{N_{scatter}}{N_{incident}\rho_{aerial}} \tag{3.2}$$

Where $N_{scatter}$is the number of gold collisions recorded by the trigger, $N_{incident}$ is the number of incoming particles and ρ_{aerial} is the aerial density of the target defined in Equation 3.3.

$$\rho_{aerial} = \frac{\rho N_a t_{target}}{A_w} \tag{3.3}$$

where ρ is the density, N_a is Avogadro's number, t_{target} is the target thickness, and A_w is the atomic weight. The trigger cross section, $\sigma_{trigger}$, can then be calculated with equations 3.2, 3.3, and written in explicit form using the numbers from the scalers that are recorded in the experiment.

$$\sigma_{trigger} = \frac{\int Scaler6}{\int Scaler8 \cdot \rho_{aerial}}$$

for 2 and 4 AGeV, and

$$\sigma_{trigger} = \frac{\int Scaler9}{\int Scaler4 \cdot \rho_{aerial}}$$

for the 6 and 8 AGeV beam energies.

The final step is to calibrate the multiplicity to the centrality of the collision. We assume that the lowest multiplicity events correspond to the trigger cross section calculated above, and that the largest multiplicities correspond to to a small cross section representing the most central collisions. In addition, we assume a monotonic relationship between the multiplicity and centrality of the collision. With these assumptions and the information about the trigger cross section, the relationship of multiplicity and centrality can be determined with Equation 3.4.

$$\%\sigma = \frac{\sigma_{trigger}}{\sigma_{Au\ total}} \frac{\int_{M_{cut}}^{\infty} \frac{dN}{dm} dm}{\int_{0}^{\infty} \frac{dN}{dm} dm} \tag{3.4}$$

where $\%\sigma$ is the percent cross section in relation to the total cross section for Au+Au, M_{cut} is the multiplicity cut, $\sigma_{trigger}$ is the trigger cross section, $\sigma_{Au\ total}$ is the total cross section for two gold nuclei, and $\frac{dN}{dm}$ is the multiplicity distribution. From the experiment, and as discussed in the previous paragraph, we know $\sigma_{trigger}$ and $\frac{dN}{dm}$ is simply measured. In a simple geometric model $\sigma_{Au\ total}$ is $\pi(r_1 + r_2)^2$ where r_1 and

	2 AGeV	4AGeV	6AGeV	8AGeV
2fm (1.8%)	190	260	285	320
3fm (4.2%)	175	235	260	290
4fm (7.4%)	160	210	230	260
5fm (12%)	140	180	200	225
6fm (17%)	125	155	170	190
7fm (23%)	105	120	135	145
8fm (30%)	85	90	95	105
9fm (38%)	60	60	60	60

Table 3.1: Filtered track multiplicity for different impact parameters. Percent cross section in relation to the total of measured Au+Au is in parentheses. DCA cut is 2.5cm, and the tracker is jtf.

r_2 are the radii of the two colliding nuclei. Only two variables remain, $\%\sigma$ and M_{cut}. One simply picks values for either $\%\sigma$, or M_{cut} and calculates the other variable. Table 3.1 shows the result of this study.

The centrality can also be expressed in the simple geometric model as an impact parameter. The magnitude of the impact parameter is the distance between the centers of the colliding nuclei. There exists an impact parameter magnitude for each $\%\sigma$ and is expressed as,

$$\frac{\pi b^2}{\sigma_{Au\ total}} = \%\sigma$$

where b is the impact parameter.

3.5 Particle identification

The TPC gives information about the momentum and specific dE/dx of each of the tracks in an event[Blum93]. The information that is interesting physically is the momentum and the particle type. The dE/dx of a particle is well understood from basic principles of electromagnetic interactions between the particle and the gas that is ionized. A simple equation that describes the dE/dx rather well is the Bethe-Bloch Equation3.5.

$$-\frac{dE}{dx} = 2\pi N_a r_e^2 m_e c^2 \rho \frac{Z}{A}\frac{z^2}{\beta^2}\left[\ln\left(\frac{2m_e\gamma^2 v^2 W_{max}}{I^2}\right) - 2\beta^2\right] \tag{3.5}$$

with

r_e	:	*classical electron radius*	ρ	:	*density of absorbing material*
m_e	:	*electron mass*	z	:	*charge of incident particle*
N_a	:	*Avogadro's number*	β	:	*v/c of incident particle*
I	:	*mean excitation potential*	γ	:	$1/\sqrt{1-\beta^2}$
Z	:	*atomic number of absorber*	W_{max}	:	*max energy transfer in a collision*
A	:	*atomic weight of absorber*			

The important thing to notice in this equation is that for a given material that the particle passes through, the dE/dx is only a function of the velocity of the particle and its charge. Since the velocity and momentum are related by the mass of the particle, we can distinguish the different particle species even if they have the same momentum. (The mass and charge come in discrete values, and this is necessary to separate the particle species.) The easiest way to see this is when one plots dE/dx vs. rigidity, see Fig. 3.3. Each band represents a particle species, and when the bands are separated one simply makes a cut around a band and that will separated the different types. Difficulty arises when the bands are not completely separated, as in Fig. 3.3. The complexity of separating the different particle species becomes much more difficult and is the subject of Chapter4.

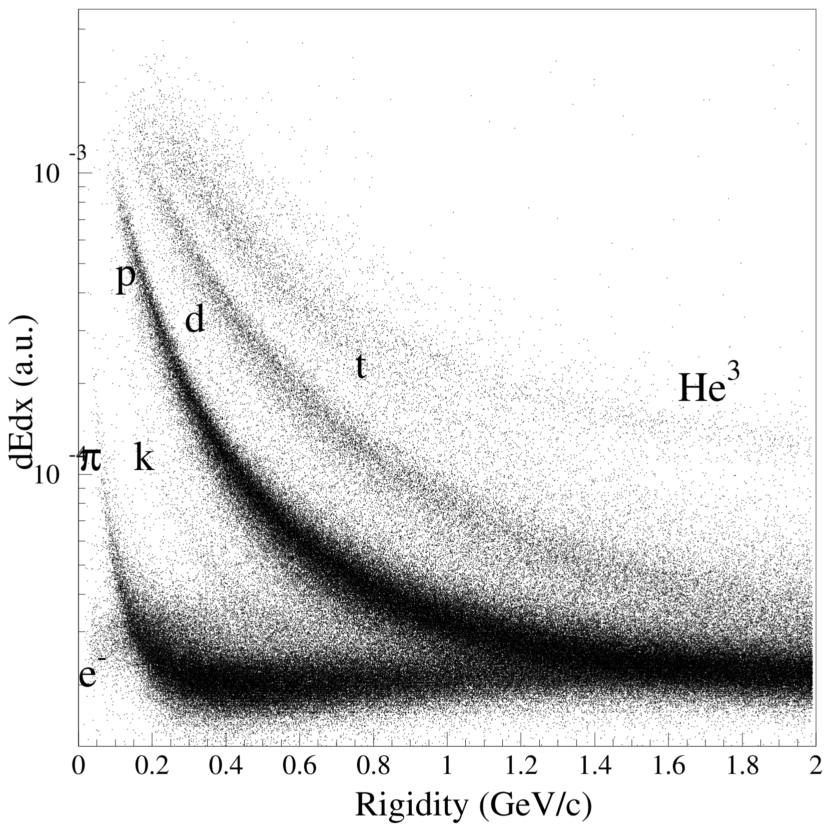

Figure 3.3: Particle identification plot with dEdx. Each particle band is marked with the species that it represents. 4GeV data, jtf tracker, dca<2.5 cut.

Chapter 4

Particle Identification via dE/dx

Particle identification, also known as pid, has been the crux of this work. The pid allows one to separate and therefore study each of the particle species. This is important as will be clear in discussions on the particle spectra. This Chapter will explain how the pid was accomplished for the spectra presented.

4.1 Advanced PID

There are various ways to identify the mass of a particles exiting a collision of Au nuclei, and it usually boils down to measuring the velocity of the particle, its charge, and the momentum or energy. The momentum divided by the charge is measured by the curvature in a magnetic field, the energy in a calorimeter, and the velocity is measured in a number of ways, Cherenkov detectors, time of flight walls, dE/dx, etc... The only method available to the E895 experiment was the dE/dx, and curvature in a magnetic field.

Looking at Fig. 3.3, we see that the bands of particles have some finite width and cross at some momentum. It turns out that at mid rapidity many of the particles are near or at the crossover region. For this reason, it is not possible to simply draw band cuts around the dE/dx vs. rigidity distribution of the particle of interest and select them that way. What is done instead is to make slices of the dE/dx vs. rigidity distribution in the rigidity parameter and look at the dE/dx distribution for that slice. Figure 4.1 is a few example slices. Notice that in some slices the particles are

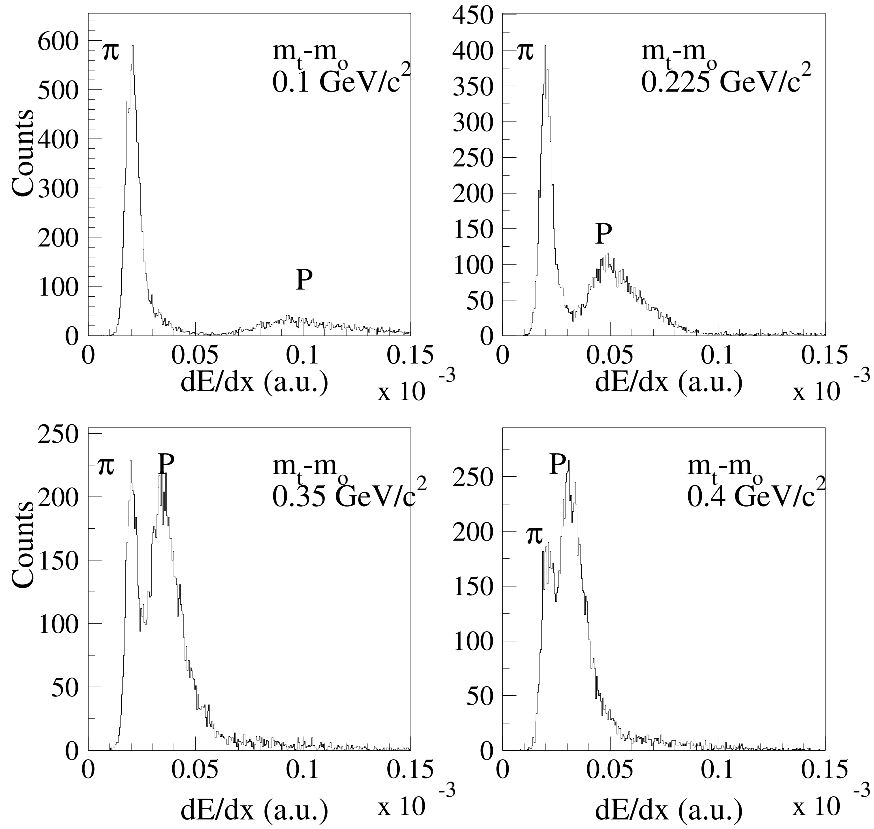

Figure 4.1: Example dE/dx spectra selected on a $m_t - m_o$ and a θ_{cm} cut using the pion mass assumption. The merging of the dE/dx distribution of the pions and protons is clear as the $m_t - m_o$ becomes larger.

more separated than in others.

If the peaks are separated enough one can simply count up all of the particles in a peak and that can be used to compute the spectra for that rigidity slice. This is what is done for the ^3He (where the α contribution to z=2 particle band is an order of magnitude smaller than the ^3He). The π^+ and the protons require a more complicated fit that deconvolutes the two particles. The UCDpid module was developed to deal with this deconvolution in the overlap region. It was later realized that the general methods used in the UCDpid module were not sufficient for the spectra analysis. The radial flow analysis only uses the mid-rapidity spectra, therefore other rapidity particles are contaminates in the spectra and effect the particle identification process. In order to avoid such difficulties in this work, the spectra are first selected from mid-rapidity and then the dE/dx deconvolution is performed. This is explained in more detail in the next section.

4.2 A few more Details on the Slices

4.2.1 Mass Assumption

There are a few more details that effect how the slices are analyzed. The first is that the radial flow analysis only needs particles that are emitted near mid-rapidity. This provides a bit of a problem, since we do not yet know the identity of the particles we can not determine which are from the central rapidity. Remember that we know the momentum in the lab frame, but one needs the mass (or velocity) of the particle to boost this momentum to the center of mass. If the undesired particles are not removed before the slice fit, there will not be any obvious way to remove them after. The solution implemented was to assume that all of the particles have the mass of the particle of interest. Then they can be boosted to the center of mass and the cut can be made. The dE/dx amplitude spectrum for a slice assuming a given particle of interest would be fit to determine the contribution from all the possible particle species including the particle of interest. However, only the fit to the particle of interest is integrated to determine the observed yield in a given slice, and the fits to the other particle species would be used to remove their contribution to the spectrum. The details of how the fits are accomplished are explained in section 4.3. Then this process is repeated for each of the particle types. This multiplies the number of slices to be fit by the number of species of interest, but allows one to select mid-rapidity particles before the dE/dx selection is made.

4.2.2 Slice Axis

The second item is more of a convenience. As we will see, the spectra are plotted as a function of E_{cm}^{kin}, the kinetic energy in the center of mass. This is related to rigidity in the following way,

$$E_{cm}^{kin} = \sqrt{(zr)^2 + mass^2} - mass \tag{4.1}$$

where z is the charge of the particle, r is the rigidity, and mass is the mass of the particle. Plotting the dE/dx against E_{cm}^{kin} instead of rigidity makes the analysis much easier. Each slice in E_{cm}^{kin} represents a single data point in the final E_{cm}^{kin} spectra for a given particle species, and therefore no complicated transformations are needed, and the data bins are evenly spaced in the results. This is a legitimate thing to do, since it is clear from Equation 4.1 that there is a one to one analytical map from r to E_{cm}^{kin} .

4.3 Slice Fitting

As mentioned before, the dE/dx spectrum for each slice needs to be fit to determine the yield of the particle of interest as well as the contributions from the other particle species. To do this, one needs to know the form of the dE/dx distribution with which to fit the spectrum. It turns out to be a little complicated. The size of a single deposit of dE/dx energy in the TPC gas has the probability distribution that is well approximated by the Landau distribution. Figure 4.2 shows the Landau distribution. It is similar to a Gaussian distribution, with a tail that extends to higher energy. Each of the deposits are summed to provide an average dE/dx value for the entire track. From the central limit theorem we know that if many such samples are taken, the final distribution will be Gaussian. For this experiment, the number of samples varies from about 7 to 128. We also know that if the initial distribution is close to Gaussian, the convergence to a Gaussian average will require fewer data points. Since the number of data points is not that large, an attempt is made to make the initial distribution more Gaussian like. This is done by removing the upper 20% of the distribution when the average is made. This improves the Gaussian shape, but

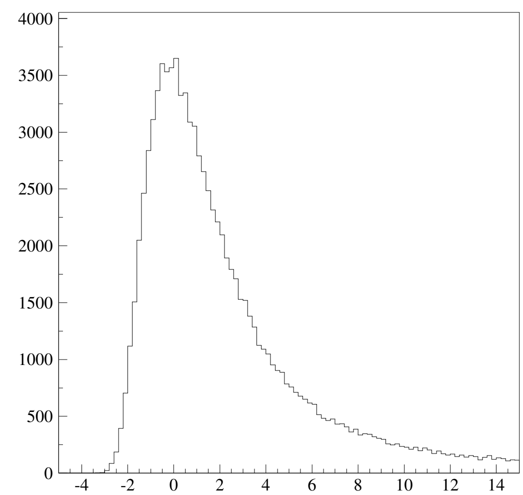

Figure 4.2: Landau distribution. The probability that a charged particle loses a quantity of energy as it passes through a gas is approximated well by the Landau distribution.

some of the asymmetry of the initial Landau shape comes through. This is handled with a two Gaussian model.

The two Gaussian model represents the asymmetry of the dE/dx distribution with a large Gaussian that represents the majority of the distribution, and a small side Gaussian that represents the small asymmetry. The idea is that the ratio of the side peak to main peak parameters are determined in the regions where the particle bands are not near each other, and then fixed to deconvolute the bands when they are close.

4.4 Pion Subtraction from Protons

At momenta that correspond to mid-rapidity and low m_t for protons, the dE/dx distributions for π^+ and protons are entangled beyond what the two Gaussian model can undo. This entanglement is due to the relativistic rise in the energy loss. In a dE/dx vs. rigidity plot the bands cross, and at the point of crossing the particles are indistinguishable. The momentum resolution and dE/dx resolution widen the crossing point so there is a range where the particles are effectively unresolvable with just information about the dE/dx and rigidity. At this crossing region we must use a different method to define the π^+ contribution which must be subtracted in order to determine the yield of the protons. The negative pions are easily identified from the majority of the other particles because of their negative charge. This gives them the opposite curvature in the magnetic field. By studying the ratio of the $\pi^+$and π^- as a function of y and $m_t - m_o$ in the momentum area where the π^+ is clearly separated from the protons, one can determine the appropriate pion ratio to use to subtract π^+ from the mid-rapidity proton dE/dx spectra. We use the forward-backward symmetry of the collision and a small amount of extrapolation to determine the ratios. The errors in this technique are largest where the pion contamination is the largest in the protons, at low m_t. A complete set of dE/dx spectra is fit assuming the proton mass, but requiring a negative charge. This yields clean dE/dx spectra of the π^-s. By multiplying the π^- dE/dx spectra by the appropriate $\frac{\pi^+}{\pi^-}$ ratio, one can define the π^+ yield to the proton mass assumption dE/dx spectra. This allows for the clean removal of the π^+ contribution to the proton spectra even in regions where the proton and π^+ dE/dx distributions completely overlap.

Chapter 5

Momentum Spectra

5.1 E_{cm}^{kin} Spectra

The spectra analyzed in this dissertation are the kinetic energy of particles emitted transverse to the beam direction in the center of mass frame(E_{cm}^{kin}).

$$E_{cm}^{kin} = \sqrt{momentum^2 + mass^2} - mass$$

Another quantity that is also commonly used is the transverse mass minus the mass, $m_t - m_0$. These two quantities are equivalent in the center of mass frame, transverse to the beam direction, because the momentum is the transverse momentum.

$$m_t - m_0 = \sqrt{p_t^2 + mass^2} - mass$$

The species measured are the π^-, proton and ^3He. These three can be reasonably identified as described in Chapter 4. The deuterons and tritions would be useful to add to this analysis and are in sufficient number, but are lost in the protons at their mid-rapidity. For species beyond the ^3He, the production drops off rapidly for increasing A at mid-rapidity.

The spectra are shown in Fig.5.1,5.2,5.3. The total number of events in this analysis is shown in Table 5.1. The events selected are only central collisions with an impact parameter <3.3 fm as determined from multiplicity which corresponds to 5% of the total cross section. The tracks within an event are further selected from the mid rapidity region. The cut used to obtain mid rapidity particles is $\theta_{cm} = 90° \pm 15°$.

	2 GeV	4 GeV	6 GeV	8 GeV
events	10598	10927	16211	11576

Table 5.1: Number of events used in this analysis.

The reasons for an angle cut instead of a rapidity cut are for the radial flow models. This will be discussed in the radial flow section.

5.2 Corrections

Once the particles of interest are deconvoluted from other particle species and the spectra histograms are produced, there are detector corrections that are made. The detector has good, but not perfect, efficiency in the portion of phase space of interest. Efficiency is defined as the percentage of real particles that passed through the active region of the detector that are actually correctly measured. In addition, the momentum is not perfectly reconstructed, and this is a function of total lab momentum. Both of these detector biases will effect the shape of the spectrum. GEANT Monte Carlo simulations are run to determine how large the effect is from each of these sources, and the E_{cm}^{kin} spectra can then be corrected. The corrections to the spectra are modest in size, and have small effects on the T and beta measurement. Figure 5.4 is an example of the efficiency correction.

The Monte Carlo that was used is called the slow simulator due to the amount of detail that is involved and associated amount of computer resources needed to run it.

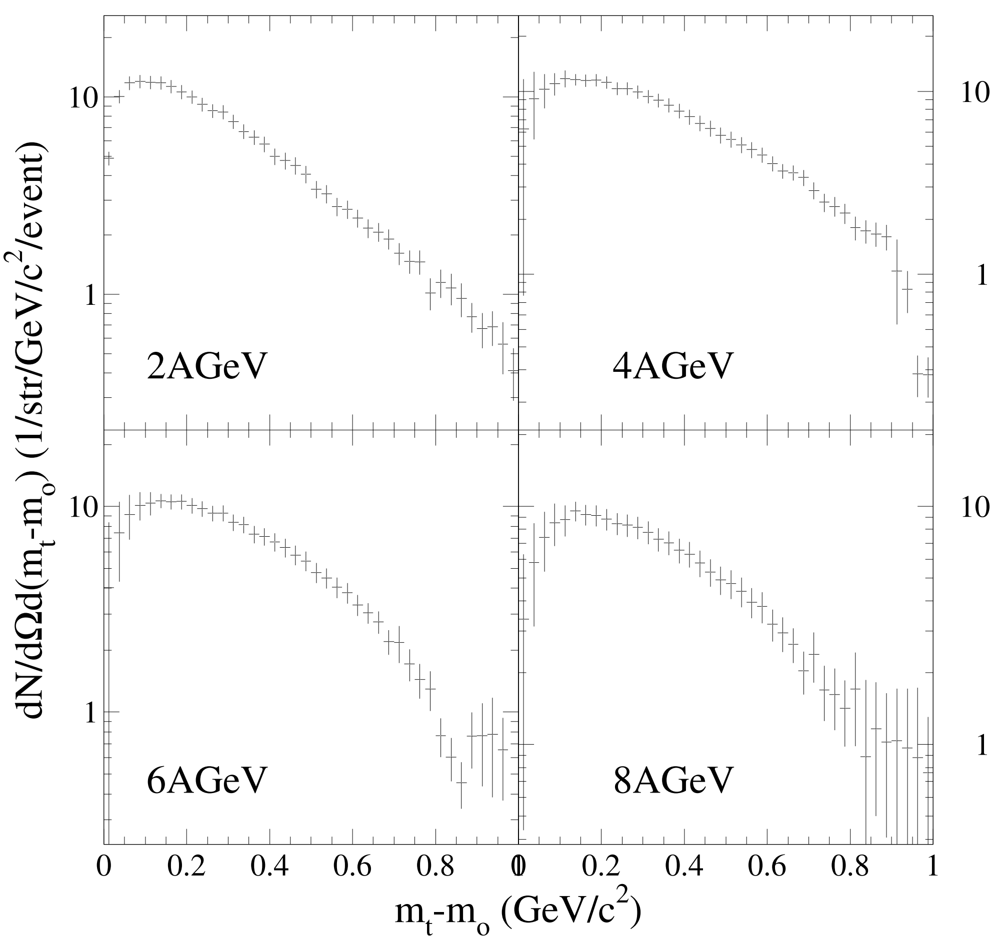

Figure 5.1: Proton spectra from data.

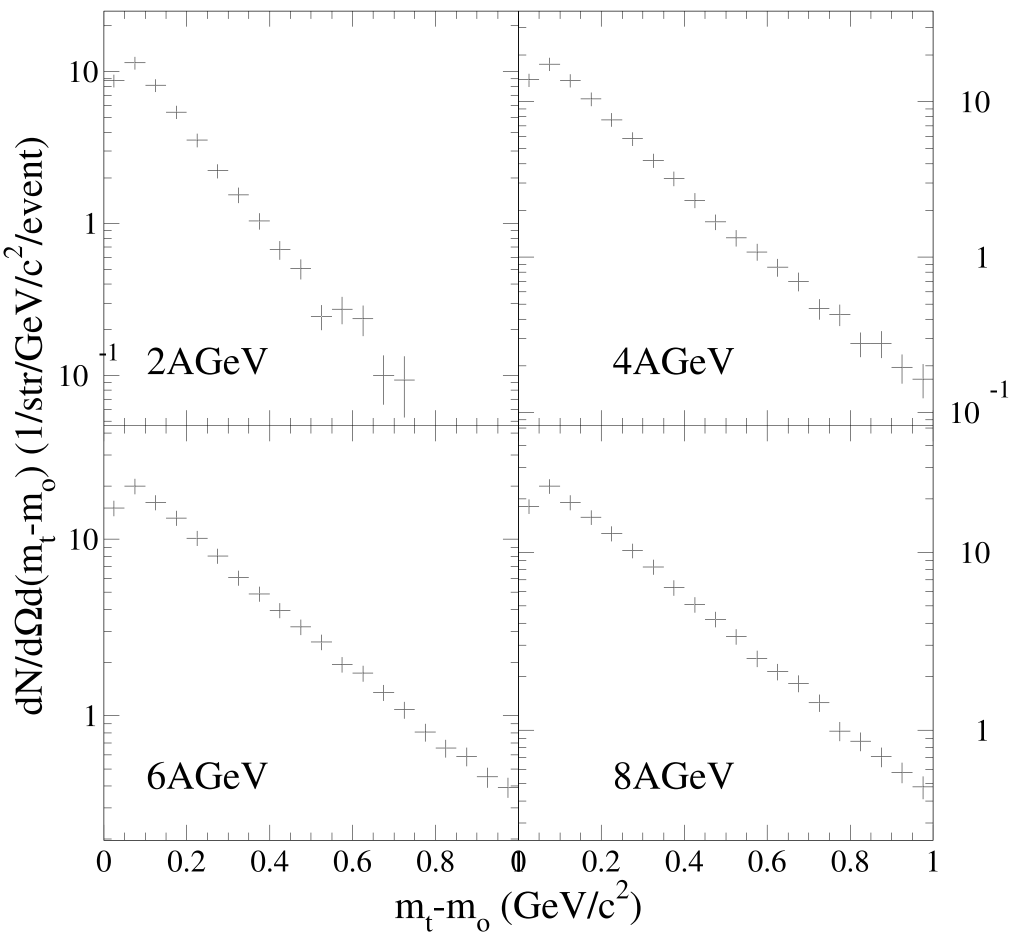

Figure 5.2: Pion spectra from data.

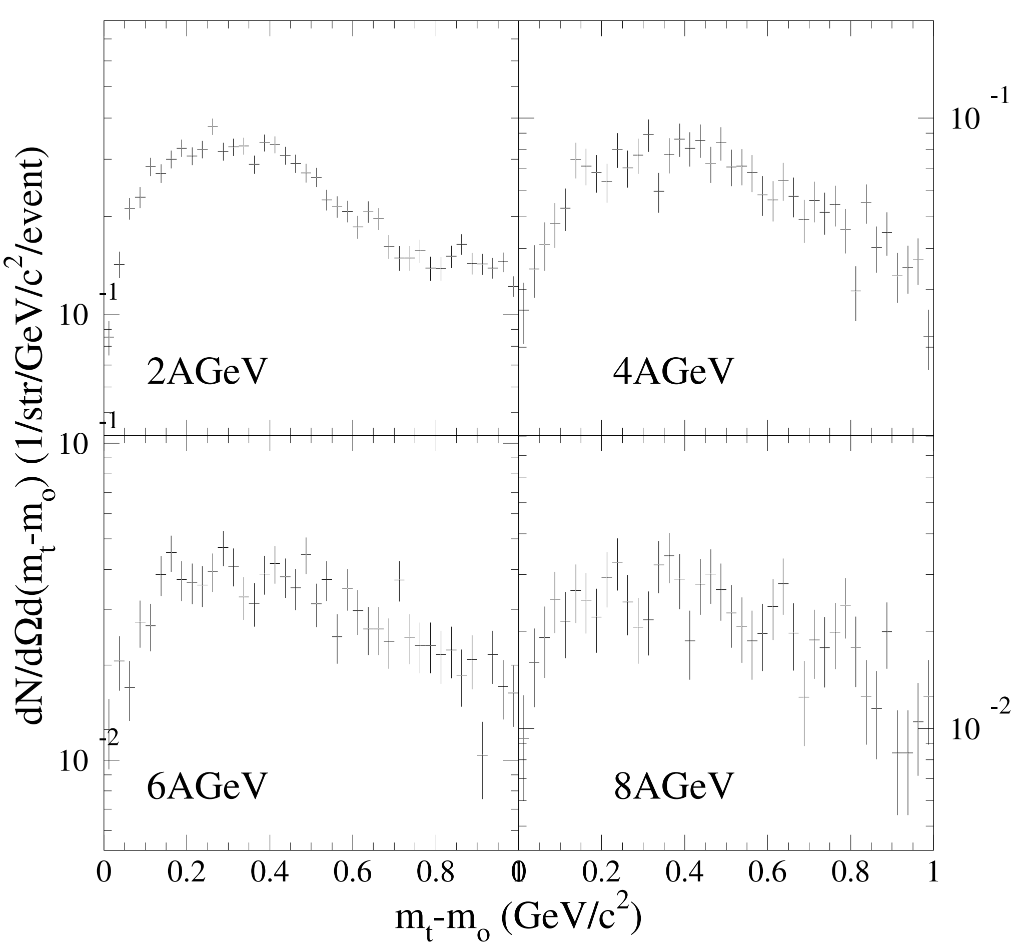

Figure 5.3: Helion spectra from data.

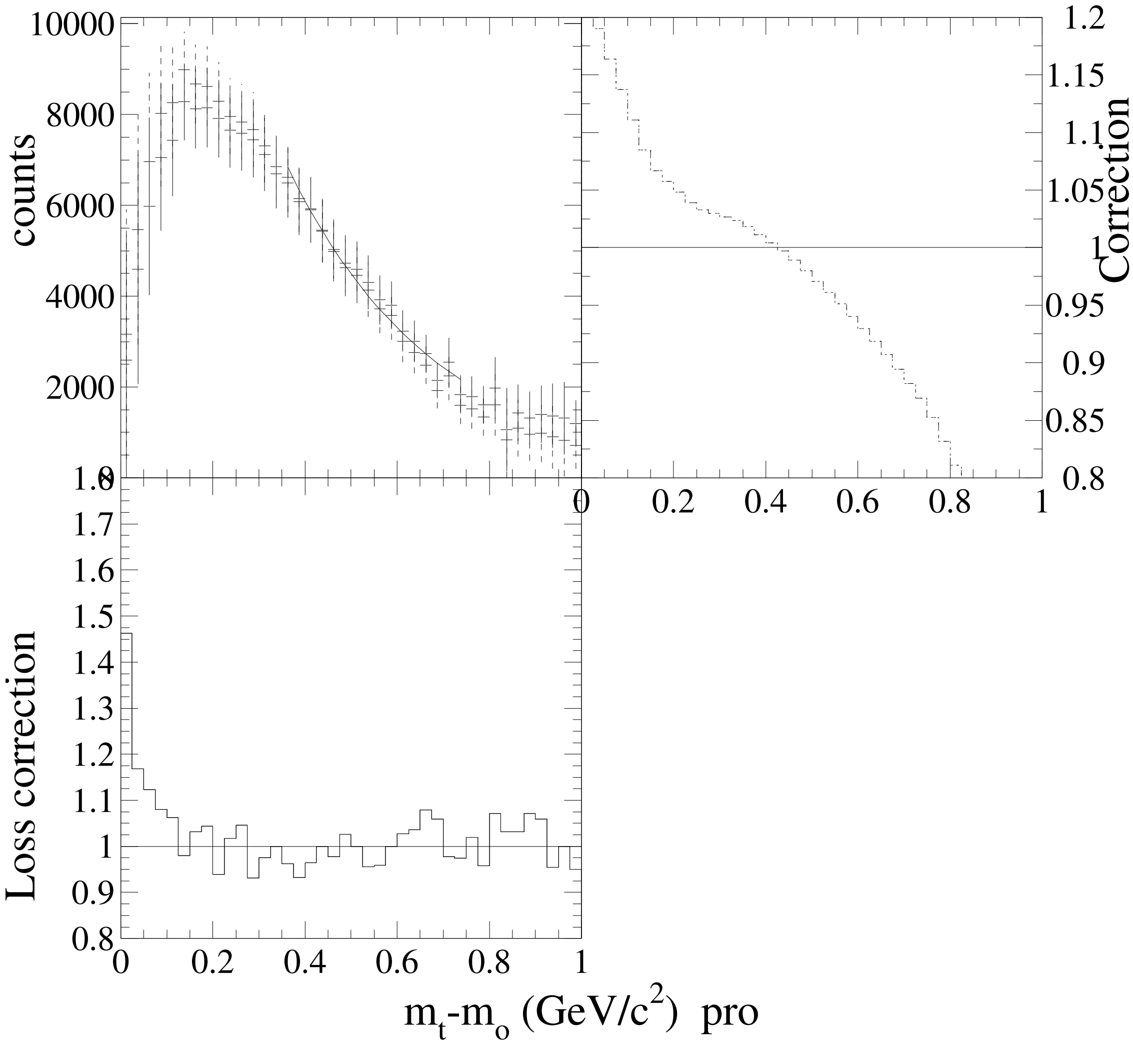

Figure 5.4: Correction for protons at 8AGeV. The upper left plot shows the uncorrected(solid symbols)and corrected(dashed symbols) spectra. The upper right plot is the total correction factor that corrects both distortions caused by efficiency and distortions caused by momentum resolution. The lower left panel shows just the correction due to efficiency.

The simulation works by embedding simulated tracks in real events and studying the output of the reconstruction to determine what happens to the input tracks. The first step of the simulation is to generate a random distribution of tracks in the momentum space of interest. In the case of the radial flow that is mid-rapidity. The phi(polar) distribution was a flat random distribution, and the $m_t - m_o$ distribution is also flat from 0 to 1. The tracks are embedded in real events in sets of four, so each set of four is also checked that they do not lie within 0.5 GeV/c of each other so there is no interaction between simulated tracks. The reason for embedding more than one is to speed up processing, and with typical multiplicities of 200-300 four extra tracks do not change the tracking environment much.

Once tracks are generated and fit the criteria above, they are then processed by the EOSGX simulation software. This software is a collection of modules that include GEANT simulation and the reconstruction software. The tracks are first processed by GEANT that simulates the electromagnetic interactions of the track with the detector, and returns the ionization that would be expected in the TPC. This is then processed by the slow simulator that simulates how the ionization will drift in the TPC. This is then mixed with real events, and the combination is then run through the full reconstruction chain. The real events into which are embedded are selected to be of the same type of events as those that will be corrected. The beam energy, multiplicity (impact parameter), target, etc. are all the same for the events that are

Beam Energy	Runs
2 AGeV	queue2, runs 1198,1201,1202,1205
4 AGeV	queue0, runs 1092,1094,1100
6 AGeV	queue0, runs 260-265
8 AGeV	queue2 1133-1139

Table 5.2: Listing of runs used for embedding purposes.

used for embedding as the events that are analyzed. Table 5.2 shows the exact events that are used for the embedding.

After the tracks are reconstructed the events are analyzed to determine whether the embedded tracks are found with the correct momentum in the output. This is accomplished by requiring that all of the tracks pass the quality cuts for the real spectra, and in addition the GEANT tracks must be reconstructed with more than 70% of the original GEANT hits. This is an important selection, but it has been found that the efficiencies change very little over a range of 50% to 95%.

The Monte Carlo showed that there are two major effects that need to be corrected in the spectra. The actual efficiency (loss of particles) and the momentum resolution. The lower left plot in Fig. 5.4 shows the correction necessary for loss of particles. This distribution is generated taking the ratio of the input Monte Carlo tracks, and dividing by the number of tracks found after the Monte Carlo for each bin in $m_t - m_o$. The momentum resolution does not enter into this plot since the reconstructed momentum is not used. This would be the correction if the momentum resolution were perfect. This efficiency correction is significant mostly at low m_t.

The upper right plot shows the total correction from both the momentum resolution and the efficiency loss. This is generated by taking the ratio of the input Monte Carlo distribution divided by the reconstructed distribution. Now that the reconstructed momentum is used, the momentum resolution effects are included. One can see that the momentum smearing is a significant effect. The magnitude of the momentum smearing can be seen in Fig. 5.5, 5.6, 5.7. It is important to note that the momentum resolution is a strong function of the number of hits on a track (nhits). The resolution plots in this thesis do not have a separate cut on the minimum number of hits per track cut (nhits), and therefore include tracks with as little as 7 hits as this is the minimum that the tracker will return. One finds that increasing the nhits cut, will dramatically improve the momentum resolution, but this improvement in momentum resolution is overshadowed by the spectrum distortion due to the nhits cut. (See Appendix D.) For this reason, the spectra are generated with the open nhits cut (nhits>7). The corrections must also be generated with the same cuts; therefore, the momentum resolution measured in this analysis is a bit poorer than one would get with tighter cuts that enable the detector to have regions where the resolution is better than 1%.

The effect of the worsening momentum resolution with increasing m_t and the shape of the distribution is to over-populate the low m_t bins. This occurs despite the efficiency loss in the low m_t region. For this reason, the flat m_t distributions that were

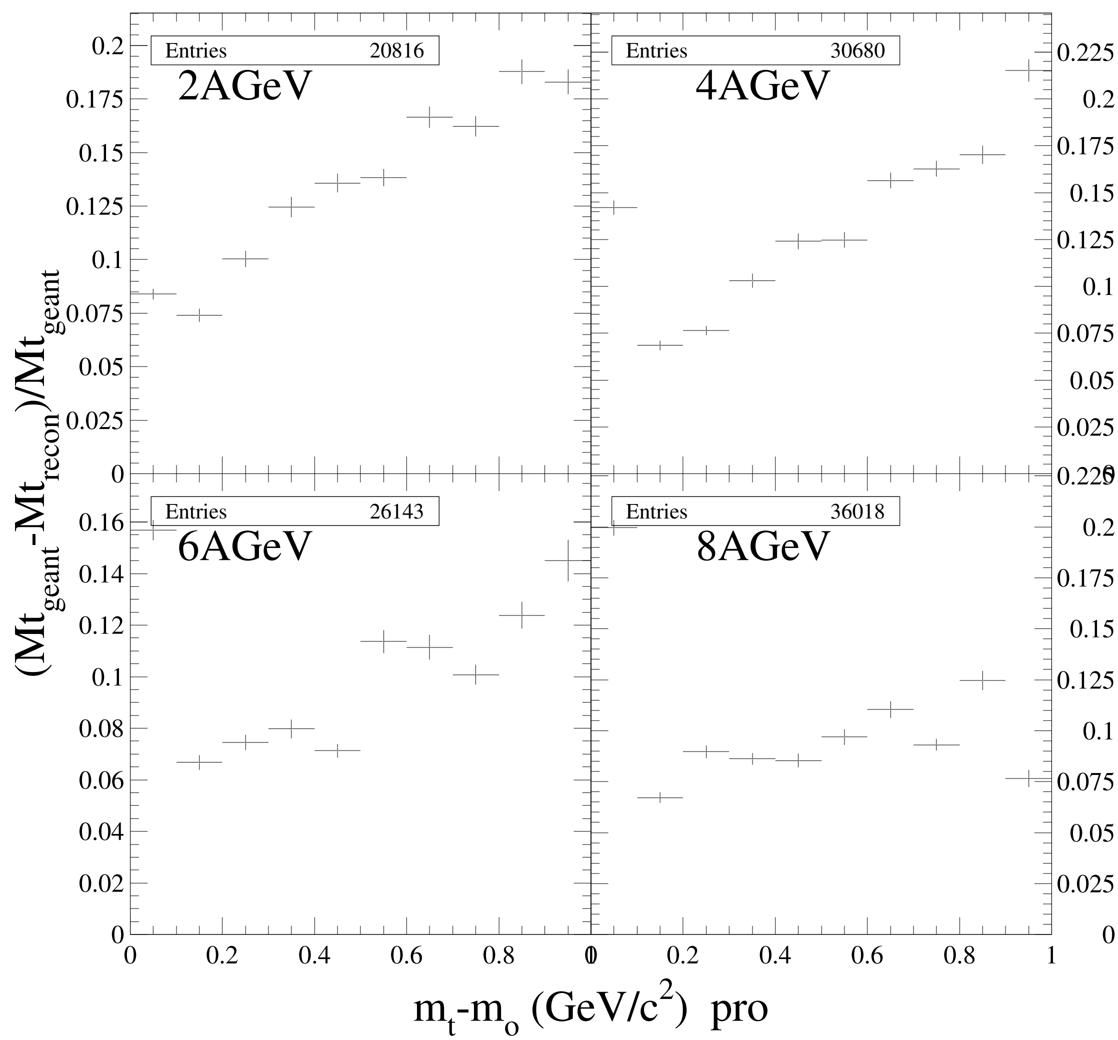

Figure 5.5: Proton momentum smearing.

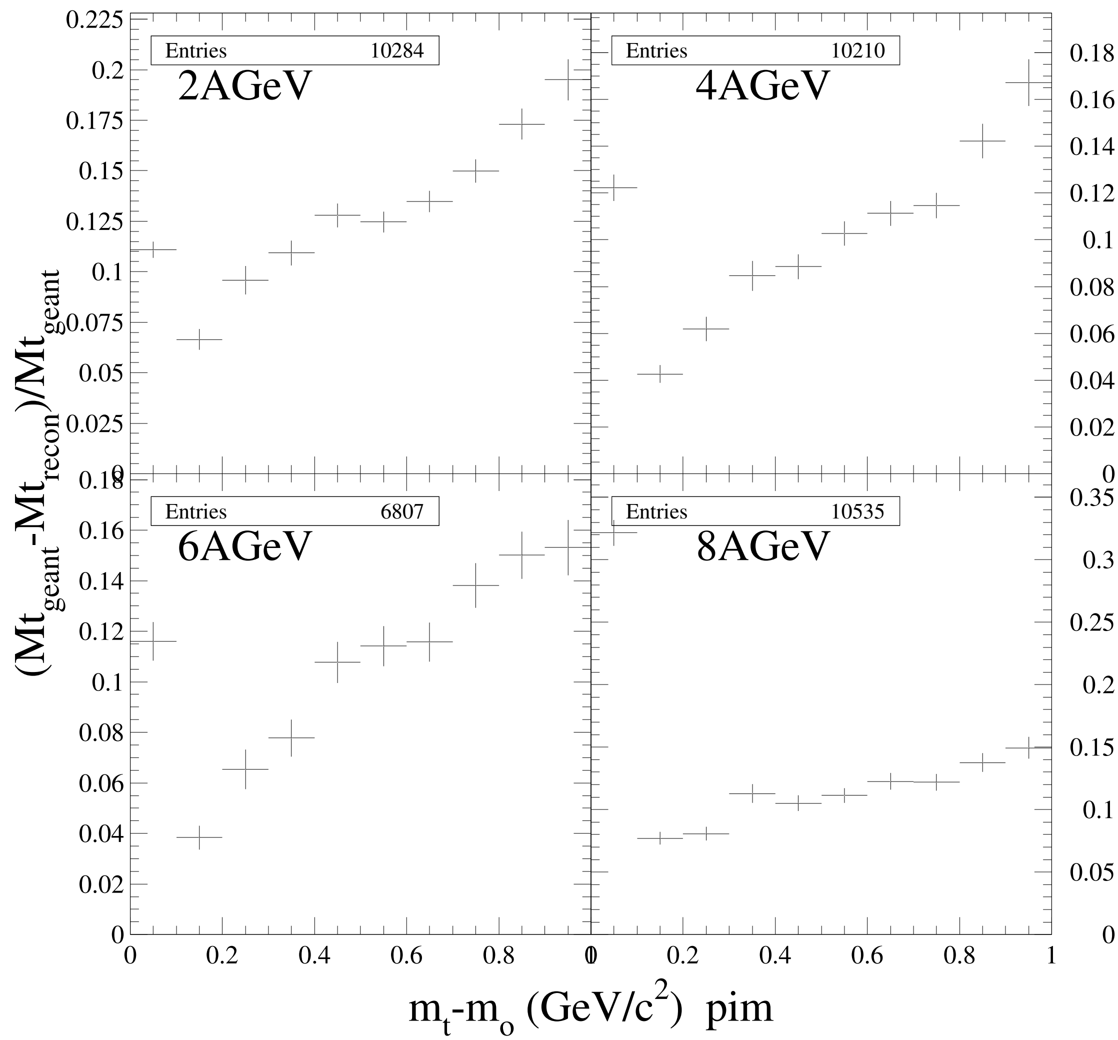

Figure 5.6: Pion momentum smearing.

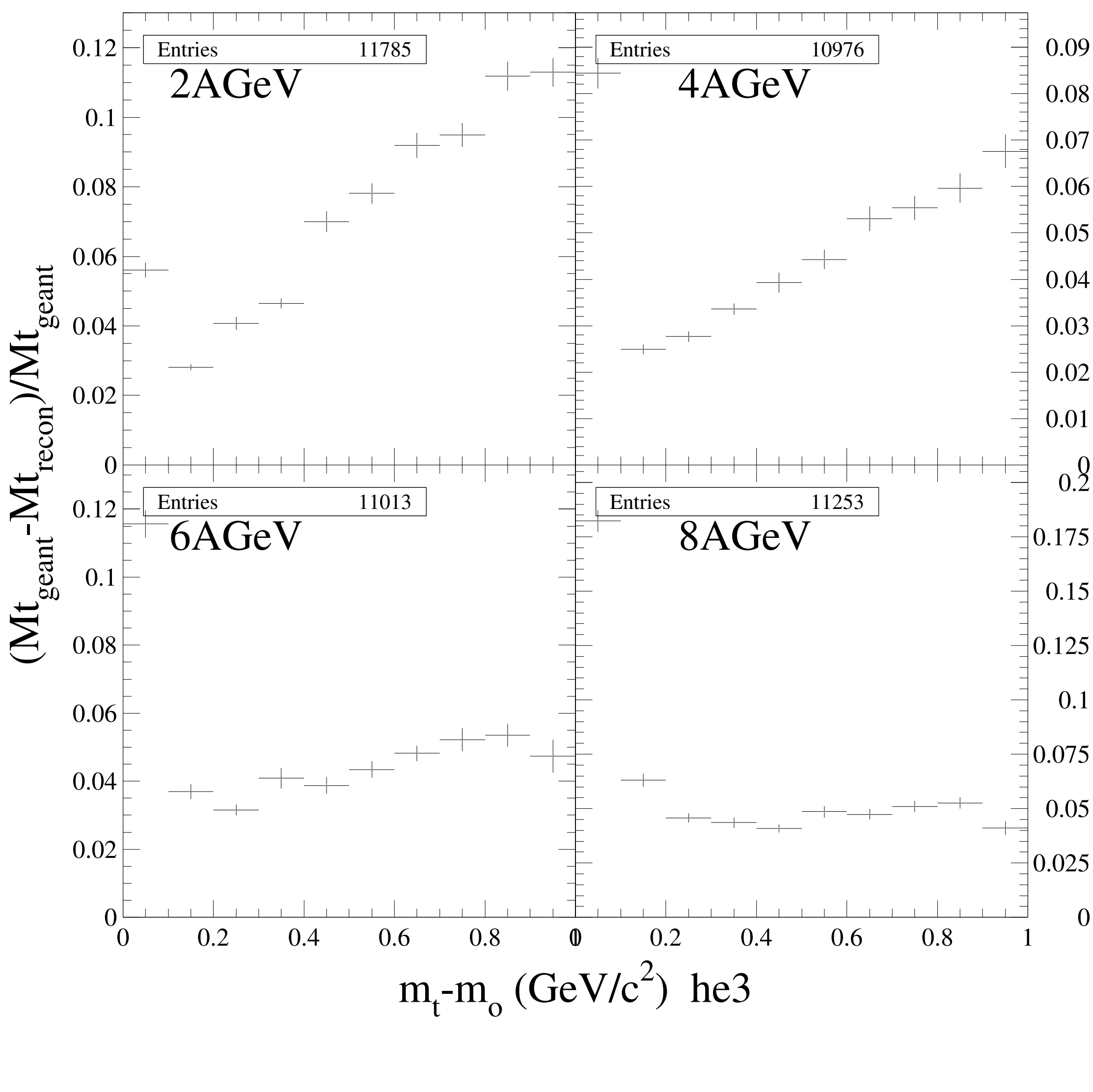

Figure 5.7: Helion momentum smearing.

used in the Monte Carlo will not correctly represent the efficiency of the detector if the input and output distributions are simply compared. One either needs to embed a distribution like the real distribution, or one needs to summarize the efficiency in a matrix so information is not lost. In this work a matrix is used.

The flat Monte Carlo was used in the following way. A TPC response matrix, $\mathbf{T}$, is constructed from the flat Monte Carlo such that,

$$\overrightarrow{S} = \mathbf{T}\overrightarrow{G} \tag{5.1}$$

where $\overrightarrow{G}$ is the vector of input momentum, and $\overrightarrow{S}$ is the result of the full Monte Carlo simulation. $\overrightarrow{G}$ and $\overrightarrow{S}$ are known so $\mathbf{T}$ is simply constructed from them. A plot of $\mathbf{T}$ is shown in Fig.5.8. One can see that $\mathbf{T}$ is almost diagonal with some spread about the diagonal, and a small amount of scatter further out from the diagonal in the matrix. If the TPC had perfect momentum resolution $\mathbf{T}$ would be exactly diagonal, and the corrections to the data would only come from lost particles. Since we have some finite momentum spreading, the correction to the data is more complicated. In principle, what we would like to have to correct the measured spectra is the inverse of $\mathbf{T}$. The correction of the data would then be a simple multiplication,

$$\overrightarrow{R} = \mathbf{T}^{-\mathbf{1}}\overrightarrow{M} \tag{5.2}$$

where $\overrightarrow{R}$ is the real physical distribution that we desire, and $\overrightarrow{M}$ is the measured

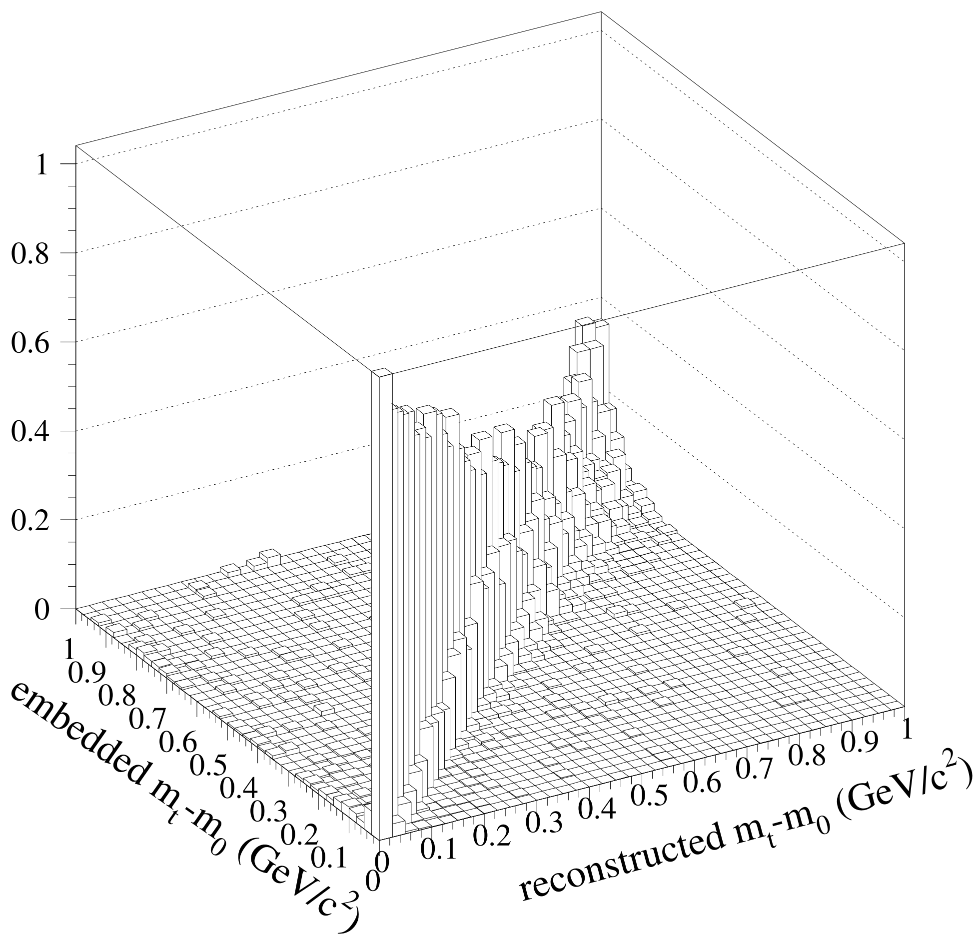

Figure 5.8: The TPC response matrix.

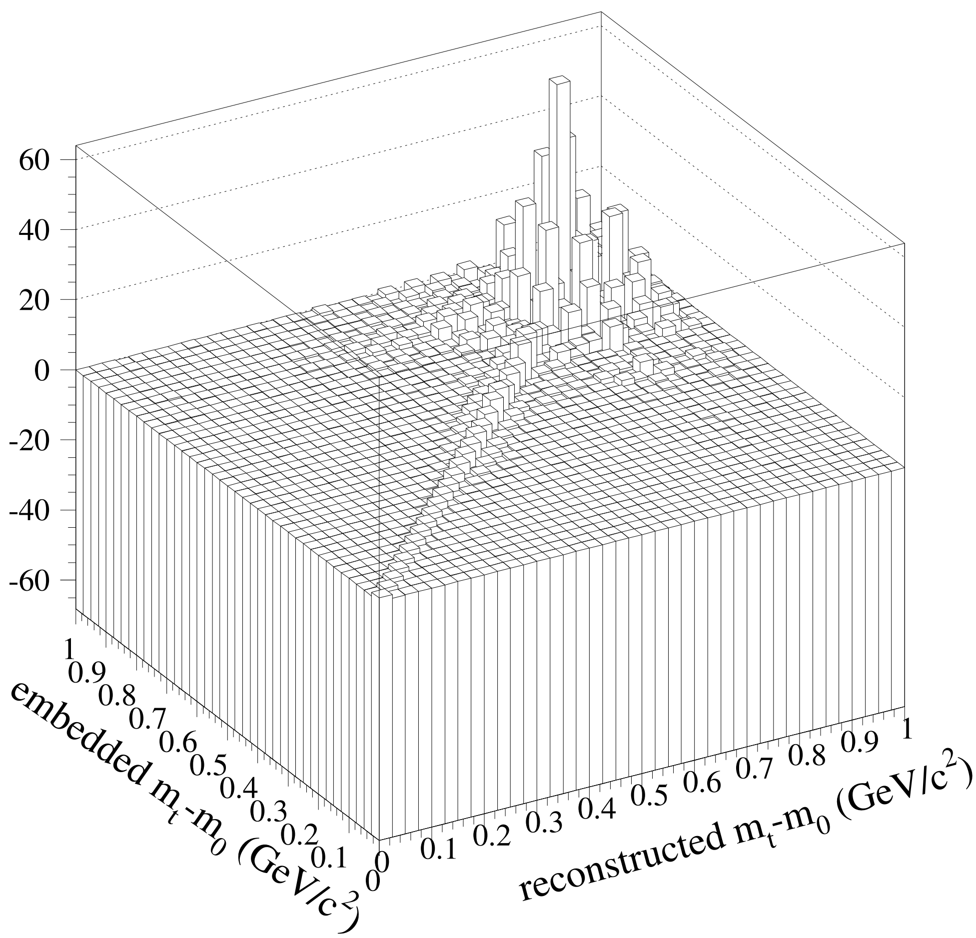

Figure 5.9: The inverse of the TPC response matrix.

distribution. It turns out that this is not a simple operation. If one simply takes the inverse of **T**, there are wild oscillations in the solution that are not physical (see Fig.5.9). This situation is a well studied problem that falls in to a category of "ill-posed" inversion problems, and this exact problem at hand is called the Fredholm Integral Equation of the First Kind.[Phil62][Twom65] This has also been used in other areas of nuclear physics[Cook63][John80]. The problem is possibly easier to see in the integral form of Equation 5.1.

$$S(x) = \int_a^b T(x,y)G(y)dy \tag{5.3}$$

In solving an equation such as 5.3 for the integrand, G(y), one has to contend with the problem that small errors in S(x) induce large errors in G(y), thus one has an ill posed problem. Techniques to solve this problem exist [Phil62][Twom65], and require the addition of information about the equation's solution. A common technique is to require the solution to be smooth, and the smoothness is dictated by the error in the data. This is equivalent to filtering the solution so that high frequencies (fast changing efficiencies), which we have little information about, do not interfere with the solution. This is a neat formalism, but it only was able to serve a guide since the solutions were not satisfactory. The Phillips solution[Phil62] to this problem is to invert **T**, then calculate a smoothed G. Once one has calculated G, one can use Equation 5.3 to calculate the corresponding S (call it S') for that G. Finally one

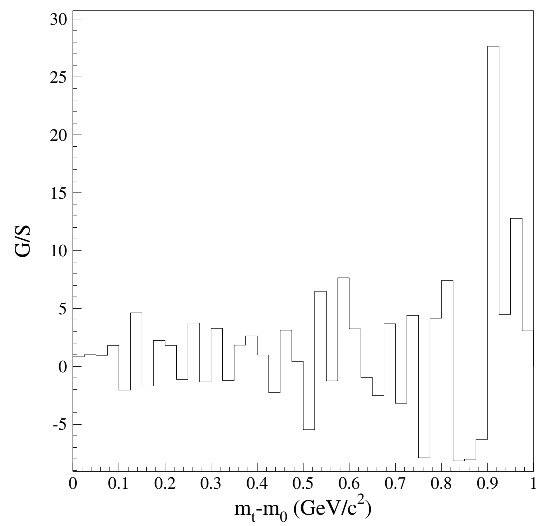

Figure 5.10: The correction using Phillip's method.

calculates the χ^2 from the difference between the original S and the S'. According to the Phillips method, the χ^2 is a measure of when the appropriate amount of smoothing has been done. Figure 5.10 shows the correction, (output/input) that is calculated from the Phillips method with a χ^2 of 1.1. It is clear that oscillations in the solution still exist. If one increases the smoothing to reduce the oscillations, the χ^2 becomes very large (over 1000) and therefore one losses the measure of how much smoothing to use.

The solution selected is much simpler and appears to represent the data well. The TPC response matrix is generated as before, Equation 5.1. Then it is true that

$$\mathbf{T}\overrightarrow{R} = \overrightarrow{M}$$

for any shape of $\overrightarrow{R}$ flat or otherwise. We then define $\overrightarrow{N}$ such that,

$$\mathbf{T}\overrightarrow{M} = \overrightarrow{N}$$

and then a diagonal matrix **D** is constructed such that,

$$\mathbf{D}\overrightarrow{M} = \overrightarrow{N}.$$

In terms of the elements, **D** is defined as,

$$D_{ii} = \frac{N_i}{M_i}; \quad D_{ij} = 0 \; for \; i \neq j.$$

Now assume that the effects of **D** approximate the same **T** since the off diagonal elements of **T** are also represented by the construction of **D**. With this assumption one can write,

$$\mathbf{D}\overrightarrow{R} = \overrightarrow{M}$$

and also the inverse,

$$\mathbf{D^{-1}}\overrightarrow{M} = \overrightarrow{R}$$

where the inverse of **D** is simply computed by taking the reciprocal of the elements of **D**. This is the approximate solution that is used in this dissertation to get the true or real physical distribution from the measured distribution. This procedure was tested on simulated data to verify the validity, and the result is in Fig. 5.11. The wide

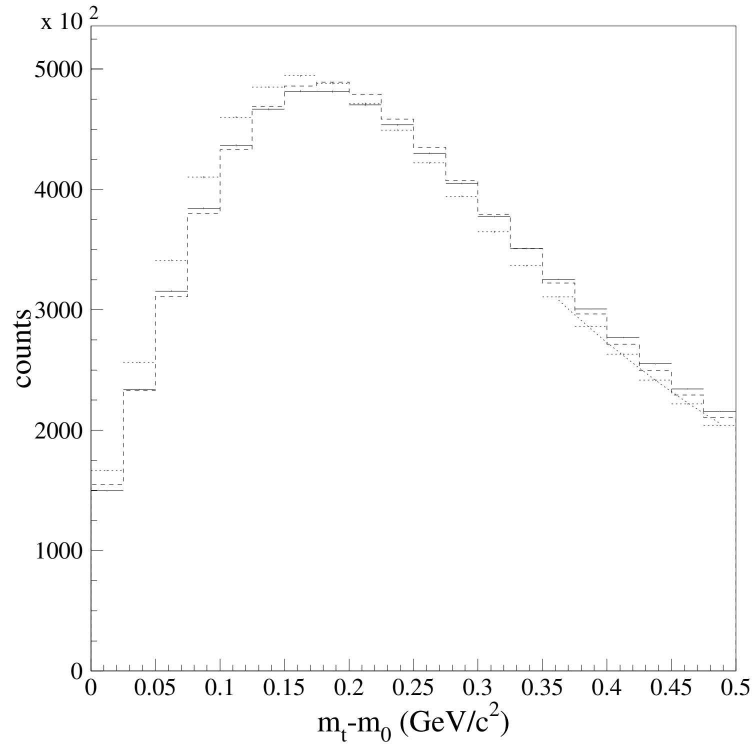

Figure 5.11: A test of the correction method. The wide dashed line is the true spectrum that the method is trying to reproduce. The thin dashed line is the true spectrum after the TPC has acted on it. The solid line is the correction to the spectrum using the correction method discussed in this dissertation.

dashed line is the hypothetical true or real physical distribution that is then acted on by the TPC response matrix to give a distribution that represents a measured spectrum (this is the thin dashed line). Now the simulated measured spectrum is corrected by the method above, and that is shown in the solid lines in the plot. One can see that the correction does in fact correct the TPC distorted spectrum.

To further test the correction used in this work I present figures 5.12, 5.13, 5.14, and 5.15. Figure 5.12 is a plot of the ratio of, the corrected spectrum multiplied by the TPC response matrix, to the measured spectrum. This ratio would be 1 if the corrections were perfect, and there were no statistical error. The flatness of the curves in the relevant region shows that the correction works. This same procedure is then repeated with a Siemens and Rasmussen fit to the data instead of the actual data. This is presented in Fig. 5.13. Again it is rather flat as expected. To test the effect of a 20% change in temperature or beta separately, the procedure is run again. The result of this is shown in Figs. 5.14 and 5.15. One can see a noticeable change from the plots compared to no change in the parameters. This indicates how well a 20% change in the temperature or in beta can be distinguished above the corrections.

5.3 Error Analysis

The error in the spectra has a number of sources. Each source is discussed below.

5.3.1 Statistical

The statistical error is on the order of 1% to 2% at the peak in the spectra for the protons and pions. The number of ^3He particles is smaller so the error is on the order of 5% to 30% at the peak of their distribution..

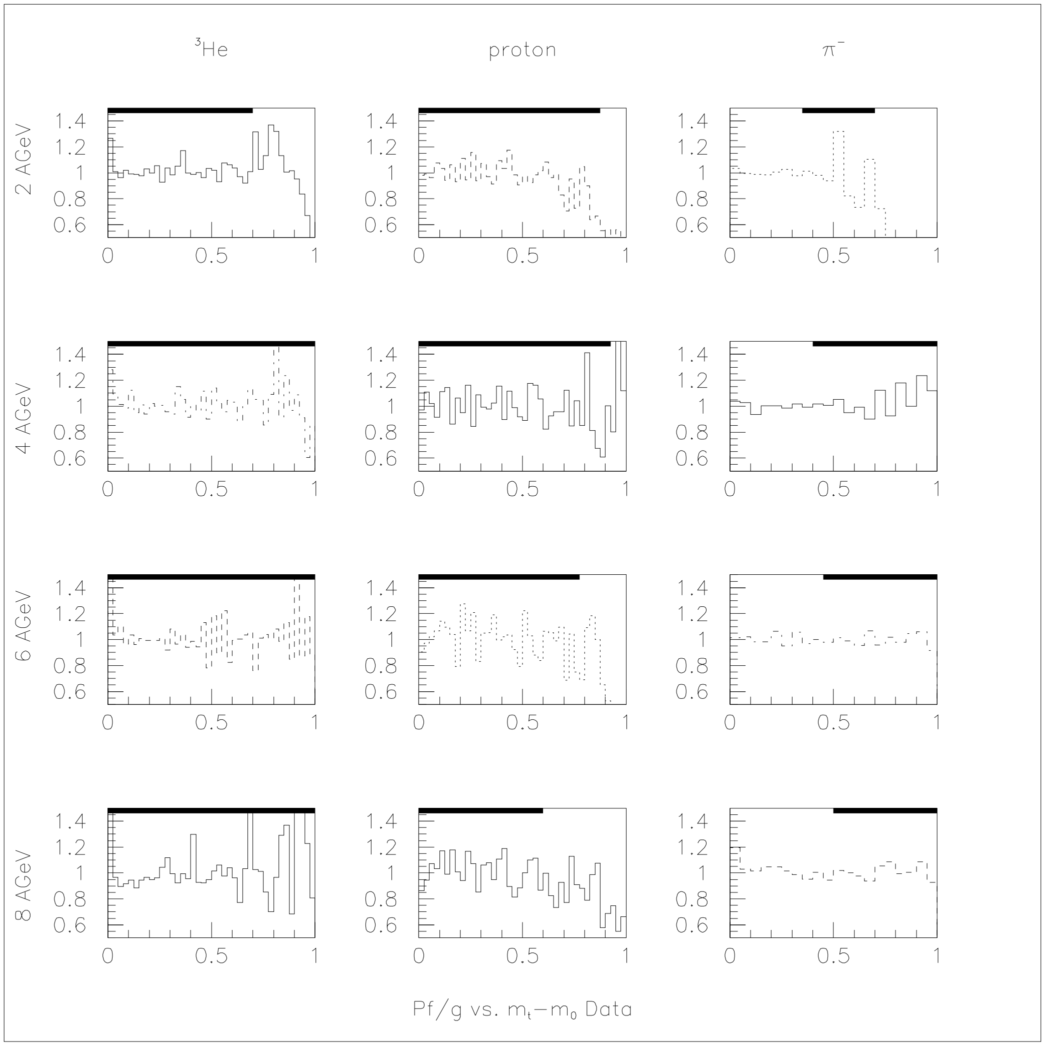

Figure 5.12: Further testing of the efficiency correction. The plot above is the reconstructed spectrum, f, operated on by the TPC response matrix, P, divided by the measured spectrum, g. If the correction is done properly, the plots above should be flat. The black line in the plot represents the range of the spectrum used in the fitting of temperatures and velocities.

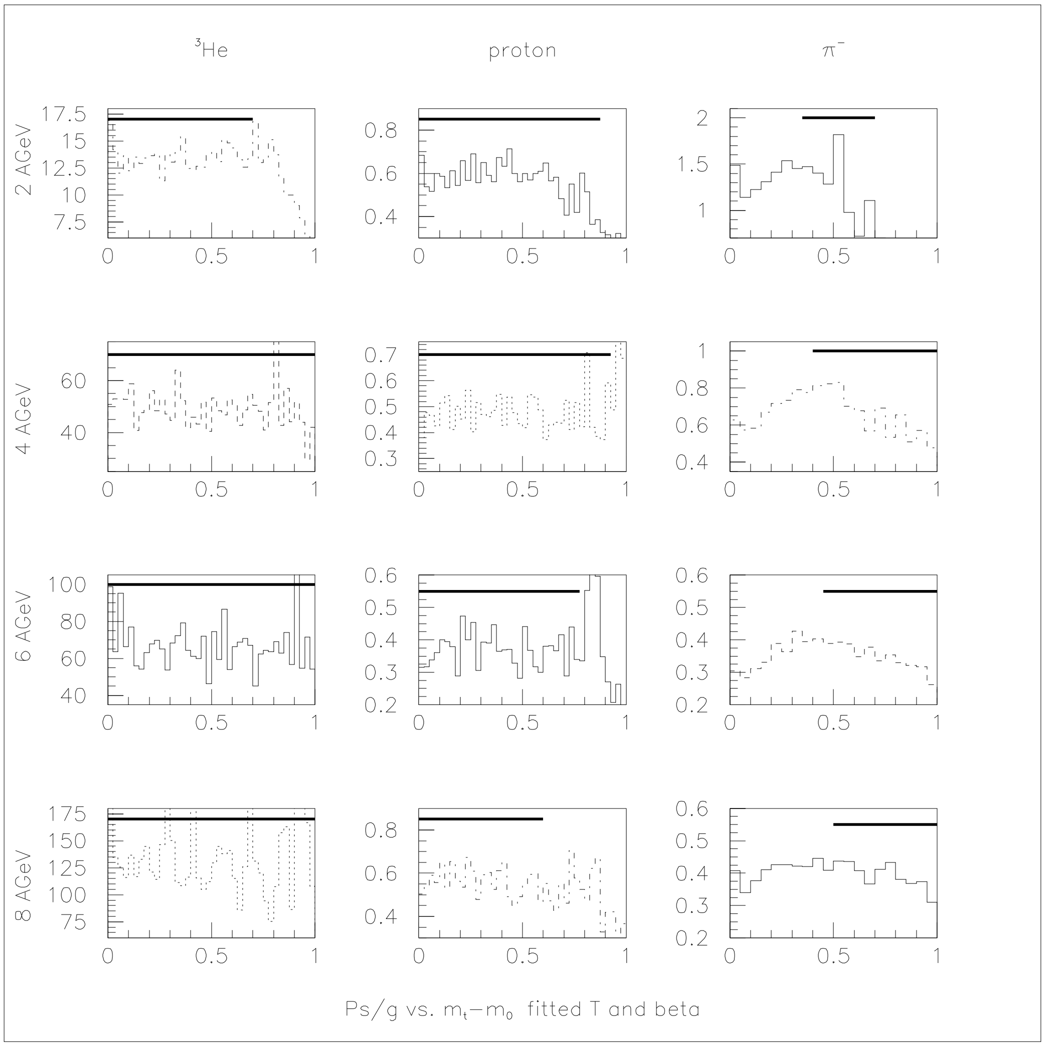

Figure 5.13: This is the same as Fig. 5.12 with the reconstructed spectrum replaced by the Siemens and Rasmussen fit.

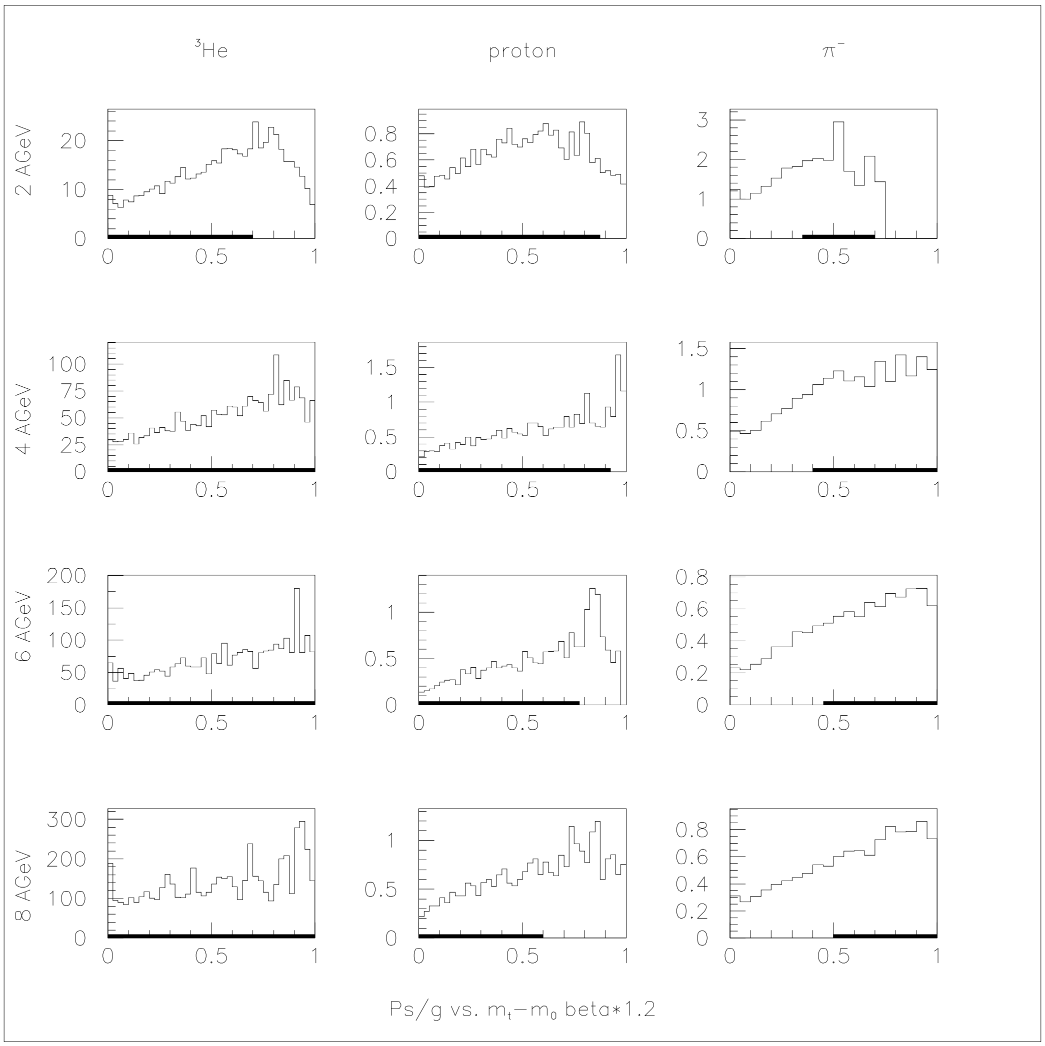

Figure 5.14: This is the same as Fig. 5.13 with the fitted beta multiplied by 1.2.

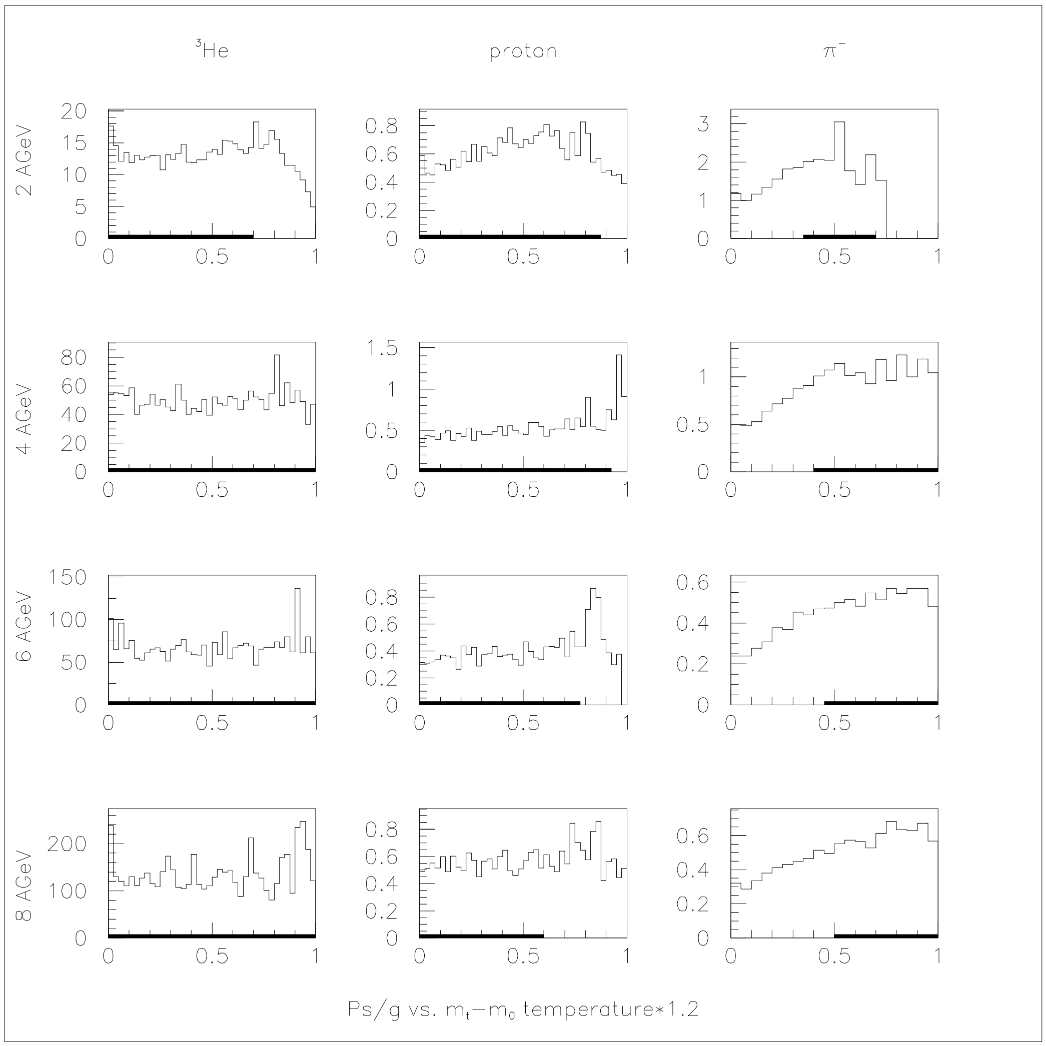

Figure 5.15: This is the same as Fig. 5.13 with the temperature multiplied by 1.2.

Beam Energy	% error on proton spectrum from kaons
8 A GeV	7.8%
6 A GeV	5.4%
4 A GeV	2.1%
2 A GeV	0.26%

Table 5.3: Systematic error of the proton spectrum measurement due to the kaon+ contamination.

5.3.2 Kaon Contamination

The kaons are not included in the fits done in dE/dx to extract particles. They therefore add a systematic error to the spectra. The contamination to the negative pions is small, on the order of 0.5% to 1% at all energies. This is determined from data taken from other experiments, E866 and E917[Ogil98] (see appendix C). These experiments had time of flight walls to differentiate particle species and hence measure the number of kaons, so these published kaon yields were simply compared to the number of pions that are measured in our experiment.

The K^+ contamination of the protons is larger, and varies with beam energy. This is due to the fact that as the energy goes up the number of kaons produced goes up, but the proton number essentially stays the same. Table 5.3 shows the contamination of kaons in the protons.

5.3.3 Two Gaussian Fit Model

The dE/dx spectra for the given $m_t - m_o$ slices are fit with a 2 Gaussian model (see section 4.3). The idea of the 2 Gaussian model is that the shape of the dE/dx spectra are almost Gaussian in shape but have a small tail caused by the fundamental shape of the energy loss, the number of dE/dx samples, and the method of truncation selected. This shape is approximated by a pair of Gaussians where the parameters of the small Gaussian are fixed in relation to the large Gaussian. The width, amplitude and centroid are all related to the main Gaussian parameters by fixed ratios that are determined in regions where the dE/dx of a single particle are clearly separated. This approximates the shape of the dE/dx in the E895 experiment, and is used simply to extract the number of particles in each rapidity slice. The error in using this model was explored by varying the parameters of this model and comparing the output. It was found that the parameter that describes the side Gaussian amplitude has error that propagates with the largest effect. This exercise has demonstrated that the error fitting the negative pions is about the same as the statistical error. For the protons the error ranges from about 5% at low m_t to about 18% at high m_t.

5.3.4 Pion Contamination

The dE/dx band for the π^+s crosses that for the protons at about 1.5 GeV/c, total momentum, which corresponds to $m_i - m_o = 0$ for mid-rapidity protons. Therefore,

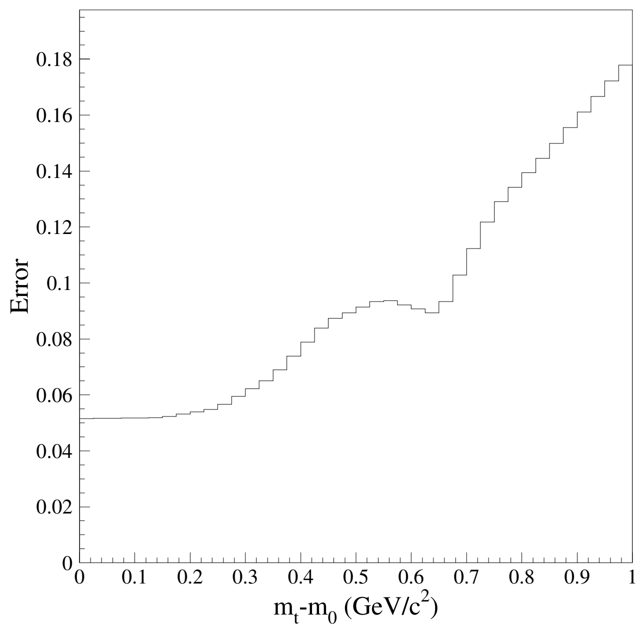

Figure 5.16: 6 GeV proton example of fractional model error, smoothed.

pions can not be removed from a fit to the dE/dx spectra generated with the proton mass assumption. They have to be subtracted using knowledge about the π^- and the ratio of $\frac{\pi^+}{\pi^-}$. The uncertainty in the $\frac{\pi^+}{\pi^-}$ induces error in this subtraction process. The error is a function of both the beam energy and the $m_t - m_o$ slice of interest. In Fig. 5.1 the larger error bars at low $m_t - m_o$ are due to this uncertainty.

5.3.5 Efficiency Error

The efficiency correction is rather small in most cases, but the low statistics of the Monte Carlo that produced it causes some error. For protons this is about 5% and for the other particles the error is more on the order of 10%.

5.3.6 Delta Resonances

The $\Delta(1232)$ is abundant at the AGS energies studied[Barr95]. This cools or softens (steeper slope in the spectra) the low $m_t - m_o$ portions of the pion spectrum. The cooling of the spectrum is simply caused by the kinematics of the Δ decay. The way to see this is with an example. We start with thinking of the Δ first in its rest frame. It will decay into the proton and pion each with the same momentum, 227 MeV/c each, (in opposite directions) due to momentum conservation. Since there is no preferential direction in the Δ rest frame, the decay axis will be randomly pointed. The result of this situation is that the average momentum for many decays is zero for both the proton and pion decay products in the Δ rest frame.

Now we consider the boost from the Δ rest frame to the center of mass frame of the collision,

$$p' = \gamma(p + \beta E)$$

where p' is the momentum in the center of mass of the collision, p is the momentum in the Δ frame, β is the boost velocity, $\gamma = \sqrt{1/(1-\beta^2)}$, and E is the total energy in the Δ frame. Since we know the average daughter momentum in the Δ rest frame is zero, we can use that to see what the average momenta look like in the center of mass of the collision. If p=0 then E=m (m is the mass) and the boost simply becomes,

$$p' = \gamma\beta m.$$

From this equation it is clear that the heavier (proton) particle will have the larger momentum in the center of mass frame of the collision since β and γ are fixed for a given boost. To further illustrate, a typical boost would be about .5c giving a γ of 1.155, and a $\beta\gamma$ of 0.5775. The mass of the proton is $0.938 MeV/c^2$ and the pion 0.1396 MeV/c^2. This results in final momenta of 0.542 MeV/c for the proton and 0.080619 MeV/c for the pion, which is the same ratio as the masses. The pion is obviously softer than the proton on average.

Chapter 6

Radial Flow

Radial flow has been described as azimuthally symmetric hydrodynamic collective motion of nuclear matter from the collision[Homb99][Volo97][Daff96][Hong98]. It occurs in central collisions where there is natural azimuthal symmetry about the beam axis. As the nuclei collide, the kinetic energy of the incident nucleons (from the translational motion given to them by the accelerator) is converted into random thermal motion, potential energy associated with the compression of the nuclear matter, and the production of new particles, mostly pions. The conversion of energy occurs from the elastic and inelastic NN collisions, and the amount of original beam energy that is converted into the fireball is dependent on the cross sections of these collisions. We know from other experiments that at AGS energies a large fraction of the beam energy in the incident nucleons is converted in the collision (stopping is large). This is currently under investigation for the E895 experiment, and the preliminary analysis indicates substantial stopping. Once a collision fireball is created it expands due to thermodynamic forces. As the system expands the density drops, and a blast wave is formed from the pressure gradient[Siem79]. At the point where the system density is low enough that there are no more strong interactions the system has reached the freeze out stage. This is the stage that the radial flow analysis images.

The thermal distributions of the particles are superimposed on the radial collective motion. A simple thermal fit to the data does not represent the data well because of the blast wave. The blast wave is the average collective motion radially outward that is caused by the hot nuclear matter expanding outward. The presence of a blast wave introduces a reduction or dip in the spectra at low $m_t - m_o$. The location, in $m_t - m_o$, of the peak or shoulder that is produced by the blast wave indicates the size of the blast velocity, and the slope of the distribution at high $m_t - m_o$ (well above the shoulder) contains information about the temperature of the system.

Simple models that have a combination of radial flow and thermal motion represent the data well [Lisa95][Siem79][Bear97][Reis97][Stac96][Agga99][Dobl99]. The Siemens and Rasmussen model gives a simple equation that can be fit to the data and the temperature and average expansion velocity can be extracted,

$$\frac{d^3N}{dEd^2\Omega} \sim pe^{-\gamma E/T}\left\{\frac{\sinh\alpha}{\alpha}(\gamma E + T) - T\cosh\alpha\right\} \tag{6.1}$$

where $\alpha = \gamma\beta p/T$, p is the momentum, $\gamma = 1/\sqrt{1-\beta^2}$, E is the total energy, and T and β are the temperature and expansion velocities. In the Siemens and Rasmussen model the fireball created in the collision is assumed to be spherically symmetric. The real data are cylindrically symmetric if we look at central collisions, and take an angular slice in the center of mass around $\theta_{cm} = 90°$ where 90° is perpendicular to the beam axis. In order to have some statistics we chose a slice 30°wide, 15° on either side. This range was also chosen by other experiments, and it aids in the comparison[Lisa95]. Fitting Equation 6.1 to the spectra allows one to determine the temperature and expansion velocity of the fire ball at freeze out.

The energy of particles leaving the collision has thermal and flow components. The energy in the thermal motion can be approximated by,

$$E_{thermal} = \frac{3}{2}T$$

where T is the temperature and $E_{thermal}$ is the the thermal energy. The kinetic flow energy can be approximated by,

$$E_{flow} = (\gamma - 1)m$$

where m is the mass, E_{flow} is the energy due to flow and $\gamma = (1 - \beta^2)^{-\frac{1}{2}}$. Using these definitions, the portion of the total kinetic energy that is from the flow can be computed.

$$\%E_{flow} = \frac{E_{flow}}{E_{flow} + E_{thermal}}$$

Typical values of T=110MeV and β=.45 c, are consistent with relatively large amounts of flow energy. The ^3He energy would be 67% from flow, the protons 40%, and the pions would be mostly thermal with only 9% of their kinetic energy from the flow. The large flow shows that considerable stopping and rescattering is occurring in the dense collision zone. The compression of the nuclear matter is then released in a collective motion in the radial direction. The more massive particles carry a larger percentage of the flow energy (common velocity), where the pions are mostly thermal due to their small mass.

6.1 Temperatures and Flow velocities

The spectra are fit with a χ^2 minimization technique to the Siemens and Rasmussen formula. The fitted spectra result in the temperatures and expansion velocities shown in Table 6.1. These are the best fits considering each species separately, and have large uncertainty due to a large correlation between the fitted temperature and expansion velocity. Small changes in the spectra values or errors can change these values substantially. With only this Table to look at one may conclude that the different particles are not in equilibrium. This is misleading since the fitted temperature and expansion velocity are so strongly correlated. It is perhaps better to look at the situation from a more global view.

An alternative to single particle fitting is to look at confidence levels in the fit parameter space to see how the area of good fit parameters compares for all of the particles. The 99% confidence levels that correspond to these fits are shown in Fig. 6.1. It is clear from the contours that there is a substantial correlation between the T and beta parameters. Each parameter represents some of the particle's energy, and therefore the correlation arises since the energy can be traded between the variables. This can be seen in Table 6.1 with the helions, for example. The temperature is rising with energy, but the expansion velocity is dropping. Knowing about the correlation one is unsure whether the energy is properly split between the thermal energy and the blast wave. The advantage of looking at a number of species is that the correlation

	2	4	6	8
T proton	115±37	115±15	93±12	103±21
β proton	.42±.07	.50±.04	.53±.03	.53±.04
T ^3He	141±13	161±23	174±34	216±135
β ^3He	0.41±.006	.44±.01	.43±.02	.40±.04
T π^-	54±15	67±10	76±13	77±17
β π^-	.52±.20	.60±.09	.64±.10	.64±.13
T total	117±4	128±5	125±6	133±9
β total	.41±.006	.46±.009	.45±.01	.44±.02

Table 6.1: Best temperature and flow velocities fitted for each species separately, and in the last two rows for all species together. T is in units of MeV and β is in c. Errors are from MINUIT fits to spectra with statistical and systematic error. They do not include systematics in fitting.

takes a different path in T,beta space depending on the mass of the particle. This has the potential to break this uncertainty. Looking at the contours in Fig. 6.1 one can see a region of overlap of the 99% contours. This overlap region is the allowed space in T, beta where a common temperature and beta describe the data.

There are two aspects to the contour plots in Fig. 6.1. The first is whether there is equilibrium within and among species, and this can be investigated by looking for crossing of the allowed-region bands. If they do not cross, then equilibrium is not reached. The second issue is: if they are in equilibrium, how can we best determine the temperature and expansion velocity. We want the overlap region to be as small as possible so the temperature and expansion velocity are determined as tightly as possible. This requires a range of masses. Each particle traces a different path in the T-β space, due to its mass, such that the very different slopes intersect at a relatively small region of temperature and expansion velocity.

A multi-particle fit to the data was performed, and the results are in the last two rows of Table 6.1. This fit was also a χ^2 minimization, but it was applied to all of the data. Figures 6.2, 6.3, 6.4, and 6.5 show the combined fit overlaid on the spectra. The model fits the data reasonably. Note that the pions are only fit in the upper bins due to Δ resonances, and that the upper few bins of the 2 AGeV helions are excluded in the fit due to problems with rapidly dropping acceptance.

6.2 Excitation Function

One of the nice features of the E895 experiment is that it scanned through four beam energies, and allows one to look at trends. The onset of interesting physics such as a change in phase should be more clearly displayed in such energy scans. The results from the multi-particle fits are displayed in Fig. 6.6. There is no clear trend of T or beta in the data, although the 2 AGeV point appears lower than the other points. The significance of this will be discussed in Chapter 7.

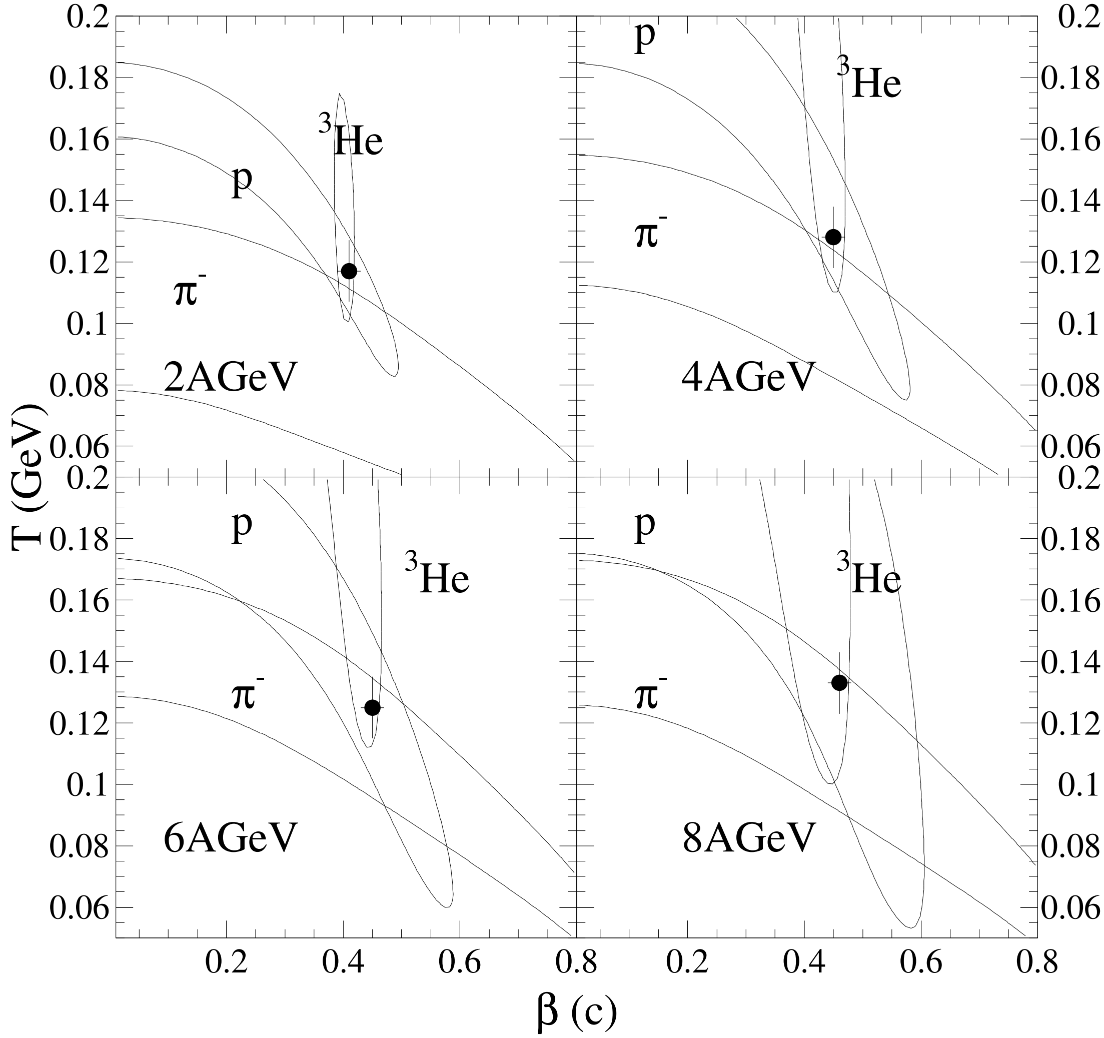

Figure 6.1: Contour plots of probability, 99% confidence level.

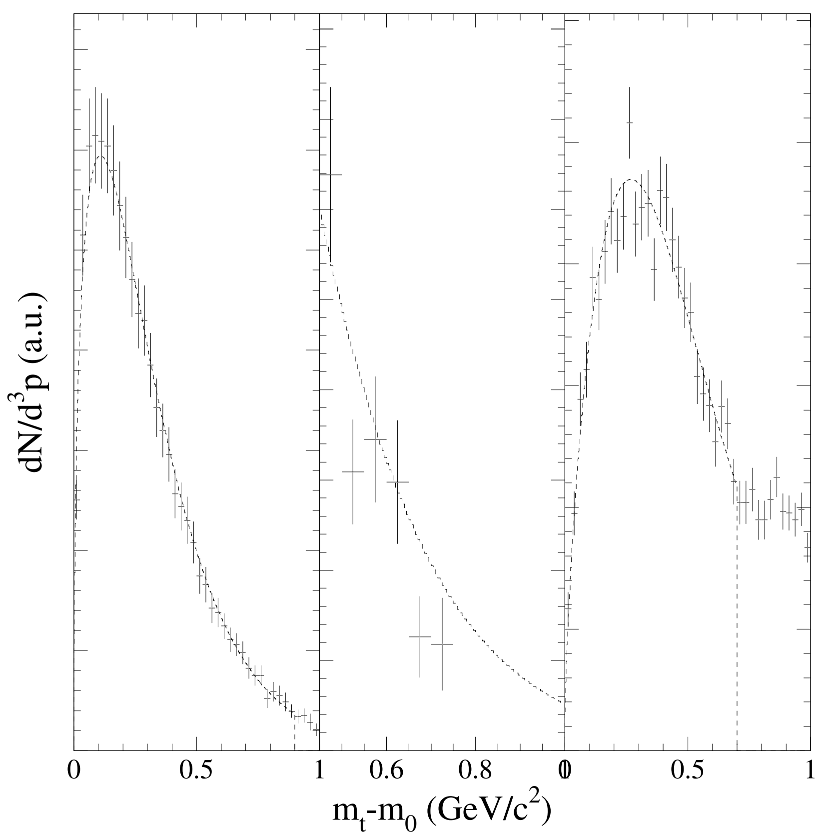

Figure 6.2: 2 AGeV spectra with multi-particle fit. The spectra are protons, π^-, and ^3He from left to right. The dotted line shows the $(m_t - m_0)$ region of fit.

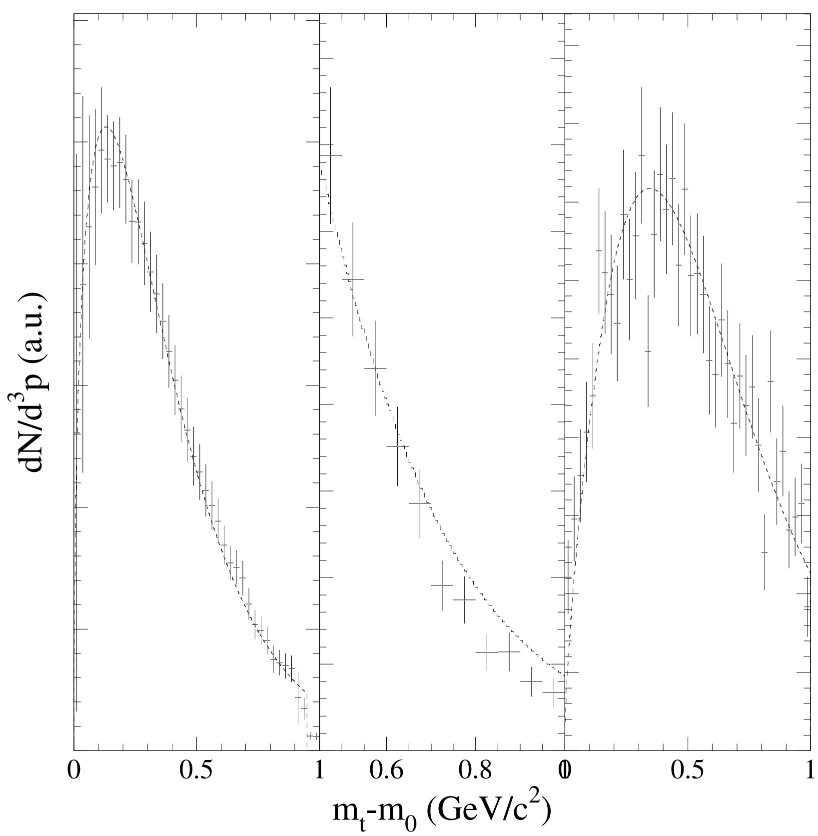

Figure 6.3: 4 AGeV spectra with multi-particle fit. The spectra are protons, π^-, and ^3He from left to right. The dotted line shows the $(m_t - m_0)$ region of fit.

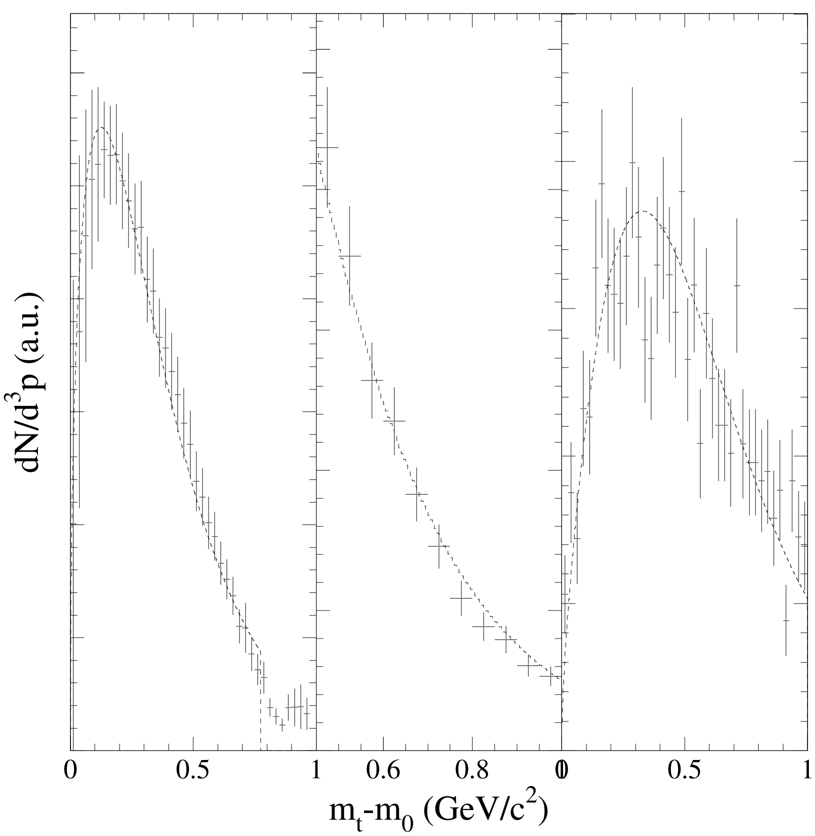

Figure 6.4: 6 AGeV spectra with multi-particle fit. The spectra are protons, π^-, and ^3He from left to right. The dotted line shows the $(m_t - m_0)$ region of fit.

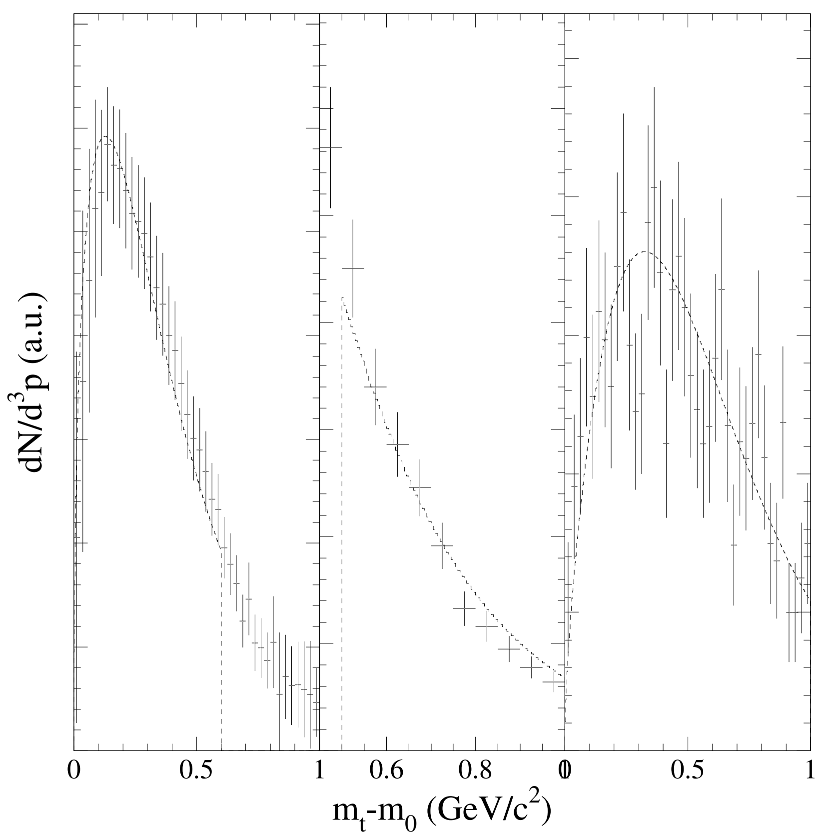

Figure 6.5: 8 AGeV spectra with multi-particle fit. The spectra are protons, π^-, and ^3He from left to right. The dotted line shows the $(m_t - m_0)$ region of fit.

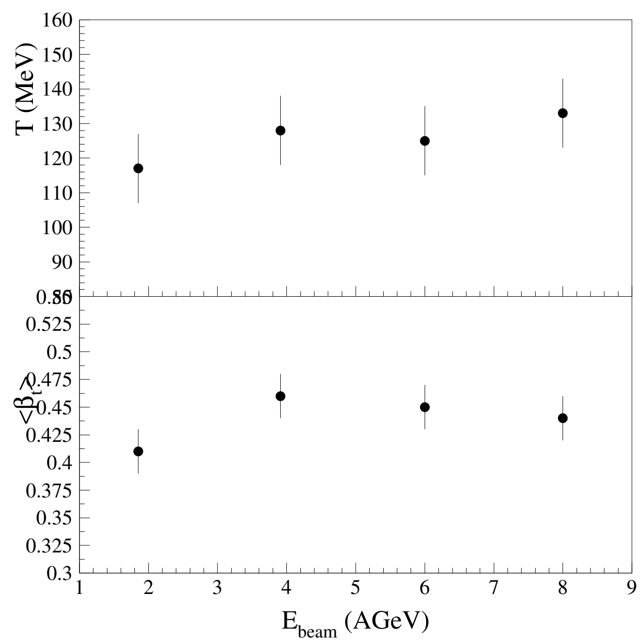

Figure 6.6: Temperature and radial expansion velocity for a combined fit to all particle types.

Chapter 7

Discussion

7.1 Equilibration?

One question that is commonly asked in such an analysis is, *is the system in equilibrium?* By looking at the T vs. β curves (Fig. 6.1) for the Siemens and Rasmussen fit, one can look for crossing of the probability curves to look for regions that are consistent with a common temperature and expansion velocity. Finding a consistent region, as in this work, hints at equilibration, but does not prove it. One can gather information from other sources that help to answer this question. The results from the E895 HBT[Lisa00] analysis could potentially provide some more hints at the validity of the equilibrium assumption. The simplest way to incorporate the HBT results is to look at the constraints in the T-β that HBT could make. The HBT parameter R_{side} in the Bertsch-Pratt parameterization is sensitive to the the radial expansion of the system. The value of R_{side} drops for increasing m_t due to this expansion. The correlation between two particles changes if they are on a surface that is rapidly moving. One way to think of this is that the particles from opposite sides are red-shifted with respect to each other, and this effects the correlation in a measurable way. This was modeled by Chapman, Nix, and Heinz[Chap95], and has a simple form.

$$R_{side} = R_G \left[1 + \frac{m_t \beta^2}{T} \cosh(y_{cm} - y) \right]^{-1/2}$$

where T is the temperature, β is the expansion velocity, y is the rapidity, R_G is the geometrical RMS radius of a Gaussian approximation to the source, and y_{cm} is the rapidity at the center of mass. We are interested in the radial flow at and near mid-rapidity, so the equation simplifies to

$$R_{side} = R_G \left[1 + \frac{m_t \beta^2}{T} \right]^{-1/2}.$$

This was fit to the data at CERN experiment NA49, and helped confine their results [Appe98]. In the E895 experiment, the HBT is limited to below about 0.3 GeV in p_t, due to two track resolution, and this turned out to not be enough range to make any substantial statements.

An other approach to determining whether equilibrium is reached, is to study the phase space density of the π^-[Bert94][Fere99]. The idea here is to compare the phase space density (in momentum and configuration space) with what one would expect from an ideal Bose-Einstein gas.

$$f(x,p) = \frac{1}{e^{p \cdot u(x)/T(x)} - 1}$$

where f(x,p) is the distribution function, p is the momentum 4-vector, u(x) is the rest frame 4-velocity at the point x in the frame of the blast, and T is the temperature also in the rest frame of the blast. This formula, assuming local thermal equilibrium, predicts the phase space density for a boson gas (the π^- in this case). This equation is then compared with the measured phase space density that is determined from the HBT analysis in conjunction with the momentum distributions over all momentum space (taking into account radial flow effects[Toma99]). The result is computed in the following way.

$$\langle f\rangle (p_t, y) = \sqrt{\lambda(p_t, y)}\frac{\frac{dn}{dy}\frac{1}{2\pi T_{eff}^2(y)}e^{-p_t/T_{eff}(y)}}{\pi^{-3/2}E_p R_s(p_t, y)\sqrt{R_o^2(p_t, y)R_l^2(p_t, y) - R_{ol}^4(p_t, y)}}$$

where $E_p = m_t \cosh y$, $\frac{dn}{dy}$ is the rapidity spectrum, $T_{eff}(y)$ is the effective temperature at a given slice in y, and R_s, R_o, R_l, R_{ol} are the HBT parameters. The denominator represents the space-time structure of the source while the numerator is the momentum space density. This method is a ongoing work, but preliminary results favor the equilibrated model of the collision. This is a welcome result from the HBT because it substantiates the premise used here in the Siemens and Rasmussen model of radial flow: the system is in at least local equilibrium.

Another issue with equilibrium is how the ^3He, with the small binding energy, can withstand the random thermal collisions of the hot hadron gas. If the ^3He were formed early in the fireball and then underwent many collisions (assuming the fireball's lifetime is long enough for that), eventually a collision would break it up. A scenario in which the ^3He could possibly survive , is formation by coalescence in the later stages and then undergoing only a few collisions to bring it into thermal equilibrium. It is also believed that the ^3He are formed by coalescence in the mid-rapidity region of central collisions[wang95].

A ^3He formed by coalescence would have a temperature 3 times the protons and neutrons from which it was formed. The ^3He would then collide with protons, neutrons and pions to reach equilibrium temperature. The kinetic energy transfer in a single collision can be large enough to bring the ^{3}He into equilibrium quickly. From simple kinematics one can calculate that in a head on collision of a proton and He, the average proton will transfer 75% of its kinetic energy to the ^{3}He in this most favorable case. This would bring the ^{3}He to the average kinetic energy in an average of 2.66 collisions with protons or neutrons at the equilibrium temperature. A pion could also work to thermalize the ^{3}He and it is capable of transferring up to 18% of its kinetic energy in a single collision.

The question that remains is then what is the probability that the ^{3}He breaks up in these collisions. The cross sections for the proton and pion on ^{3}He at this energy are not readily available, but one can find neutron on ^{3}He cross sections from 0-30 MeV from the EXFOR server on the web (the national nuclear data centre) that summarizes all of the nuclear cross sections measured. The elastic cross section in the EXFOR data is at least twice as big as the inelastic at 30 MeV, and even larger at lower energies. This means that at least in the tail of the thermal distribution the collisions would tend to thermalize the ^{3}He and not break them up. If we assume that the proton and pion cross sections are approximately similar to the neutron, the proton and pion would also contribute to the thermalization.

The temperature width of the ^{3}He contour in Fig.6.1 may derive from those nuclei that retain memory of the temperature 3T at the birth from coalescence.

7.2 Comparisons to other experiments

One strength of the E895 experiment is the availability of four beam energies. One can go further and compare similar analyses over many experiments. Figure 7.1 shows the E895 data with other experimental results in addition to the ones measured in this work. One can see in Fig.7.1 that the E895 results fit smoothly between the EOS data below and E866/E877 data above. The data are consistent with a leveling off in the freeze-out temperature, and define the elbow in the excitation function. This shape of the temperature as a function of beam energy was suggested by Hagedorn [Hage70] in what he called "Hadronic matter near the boiling point". His main idea is that particle production absorbs any extra energy instead of heating up the matter that already exists. Later papers have studied this idea in modern models (UrQMD) [Belk98] and found the same leveling off of temperature as a function of energy density.

The flow velocity also appears to level off with beam energy. The rising trend up to the level off can be reproduced in models [Li96], and appears to be more a function of the thermal pressure as fit by the Siemens and Rasmussen model, than due to a nuclear (NN) potential pressure. The E895 experiment is important, as it spans the energy range where the temperature and expansion velocity level off, and define the location of the elbow in the excitation function of T and beta.

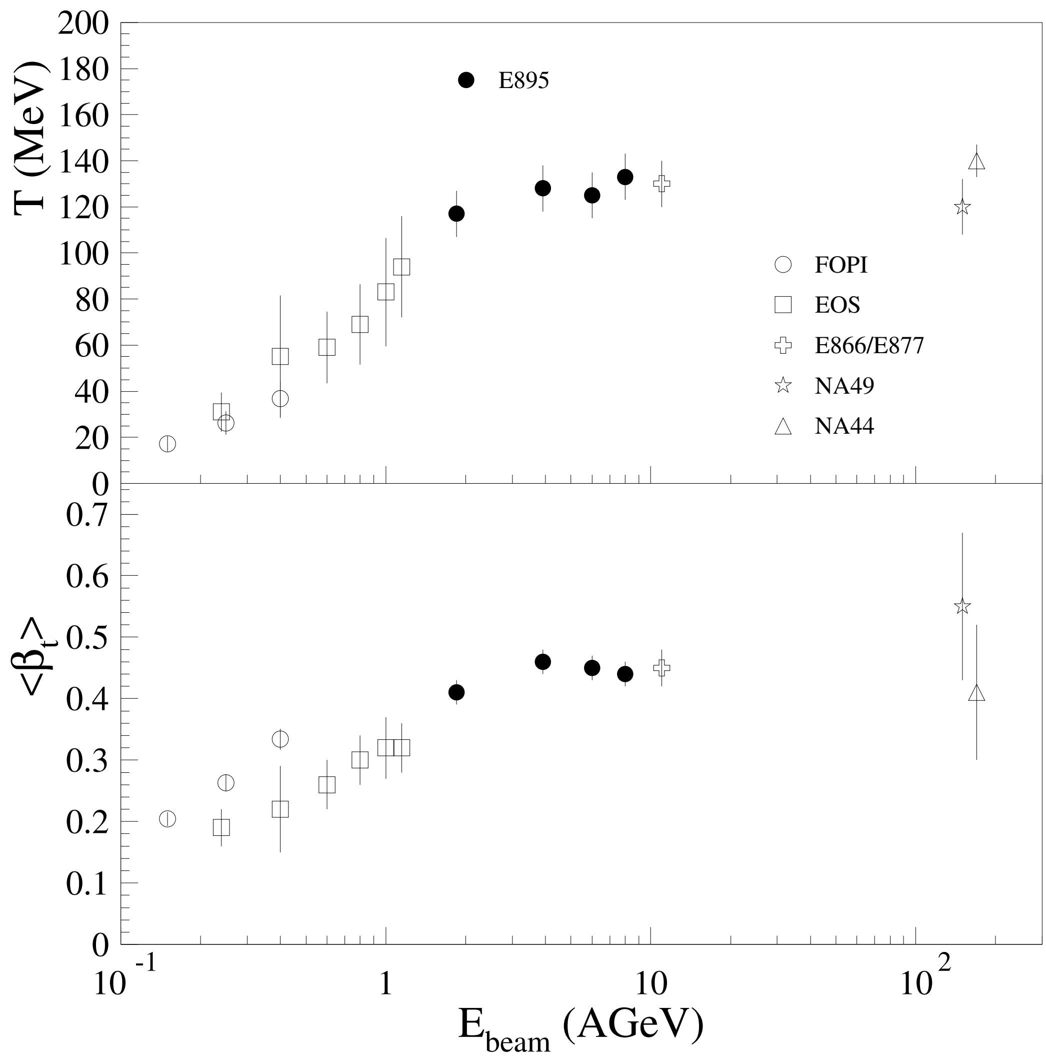

Figure 7.1: Comparison of radial flow data. The error bars come from 1-σ contours analogous to the 99% contours in Fig. 6.1.

7.3 Summary

We have presented the central, mid-rapidity, transverse, momentum spectra from the E895 experiment. The spectra shapes are distorted from a simple thermal distribution, and are consistent with a thermal plus "blast-wave" description. The data were fit with the Siemens and Rasmussen model that has worked well on this experiment and on others. The temperature and expansion velocities that are extracted over the 2-8 AGeV beam energies smoothly fit between the measurements of other experiments. Considering the data from this experiment and others, it appears that the freeze-out temperature is leveling off near 120 MeV within the energy range of this experiment. It will be interesting to follow the results of similar analysis in the colliders that will soon turn on, and see whether the trend continues.

Appendix A

Efficiency and Momentum Corrections

These are the efficiency and momentum corrections for all species (see section 5.2).

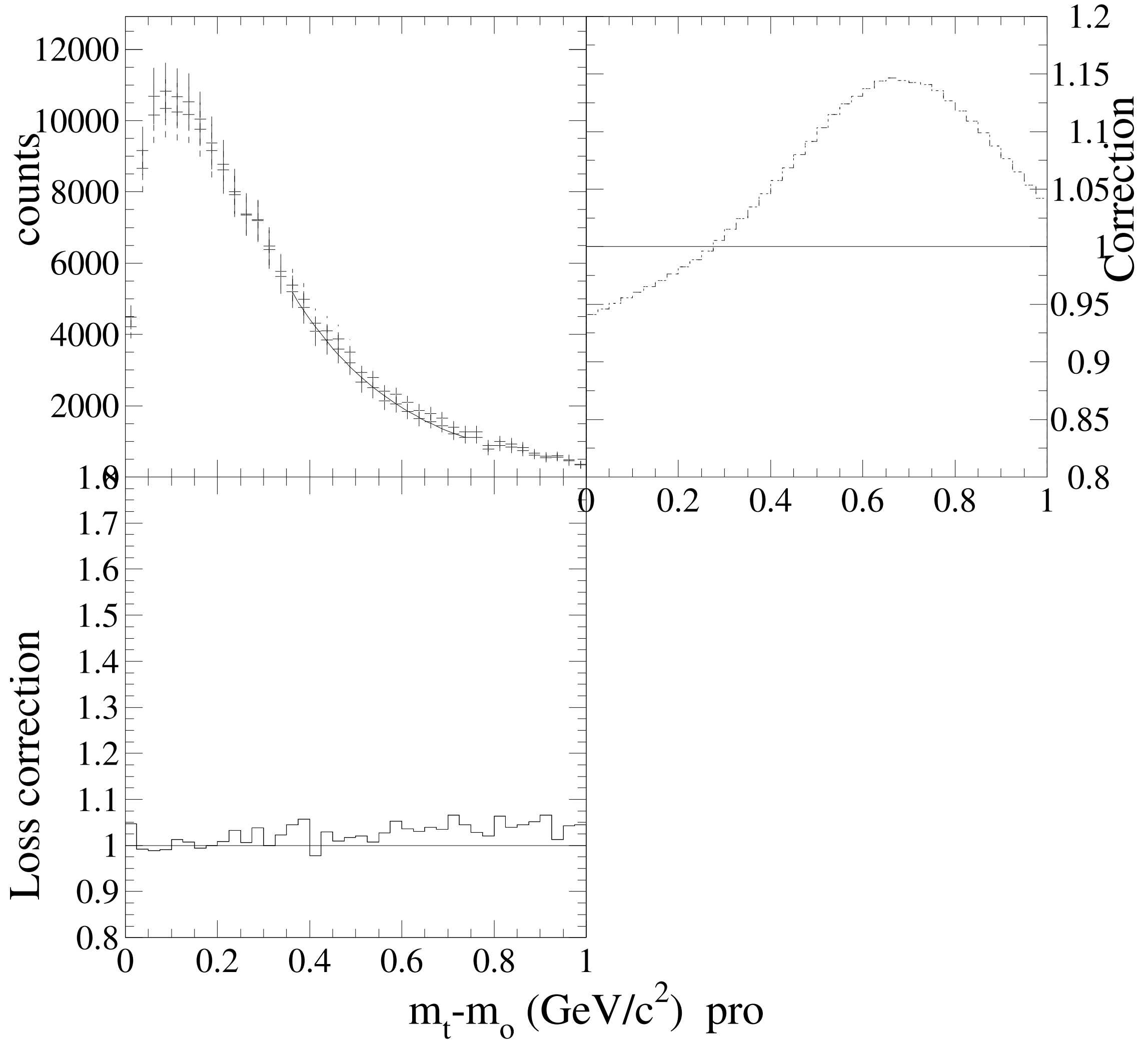

Figure A.1: 2 AGeV Protons

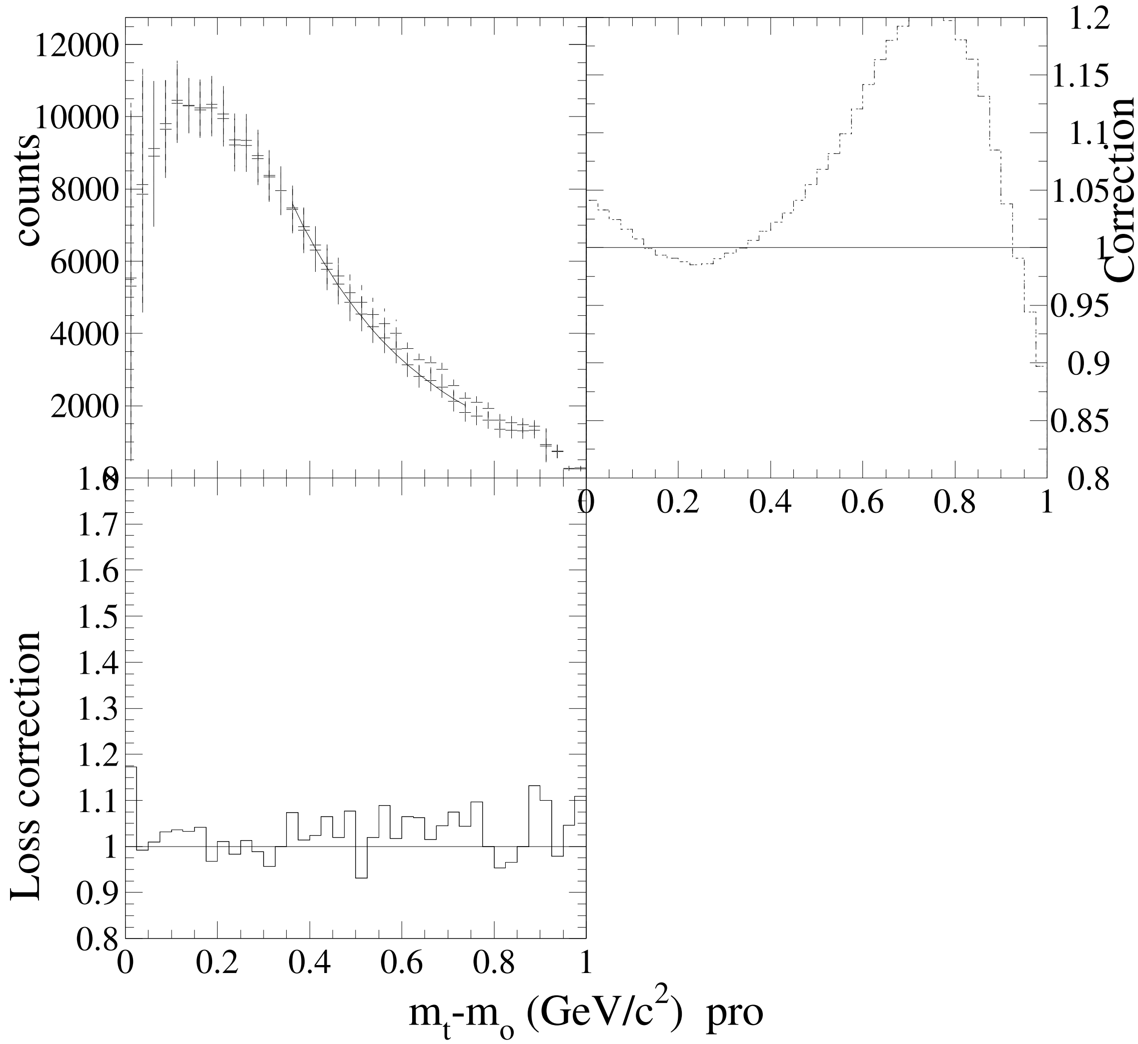

Figure A.2: 4 AGeV Protons

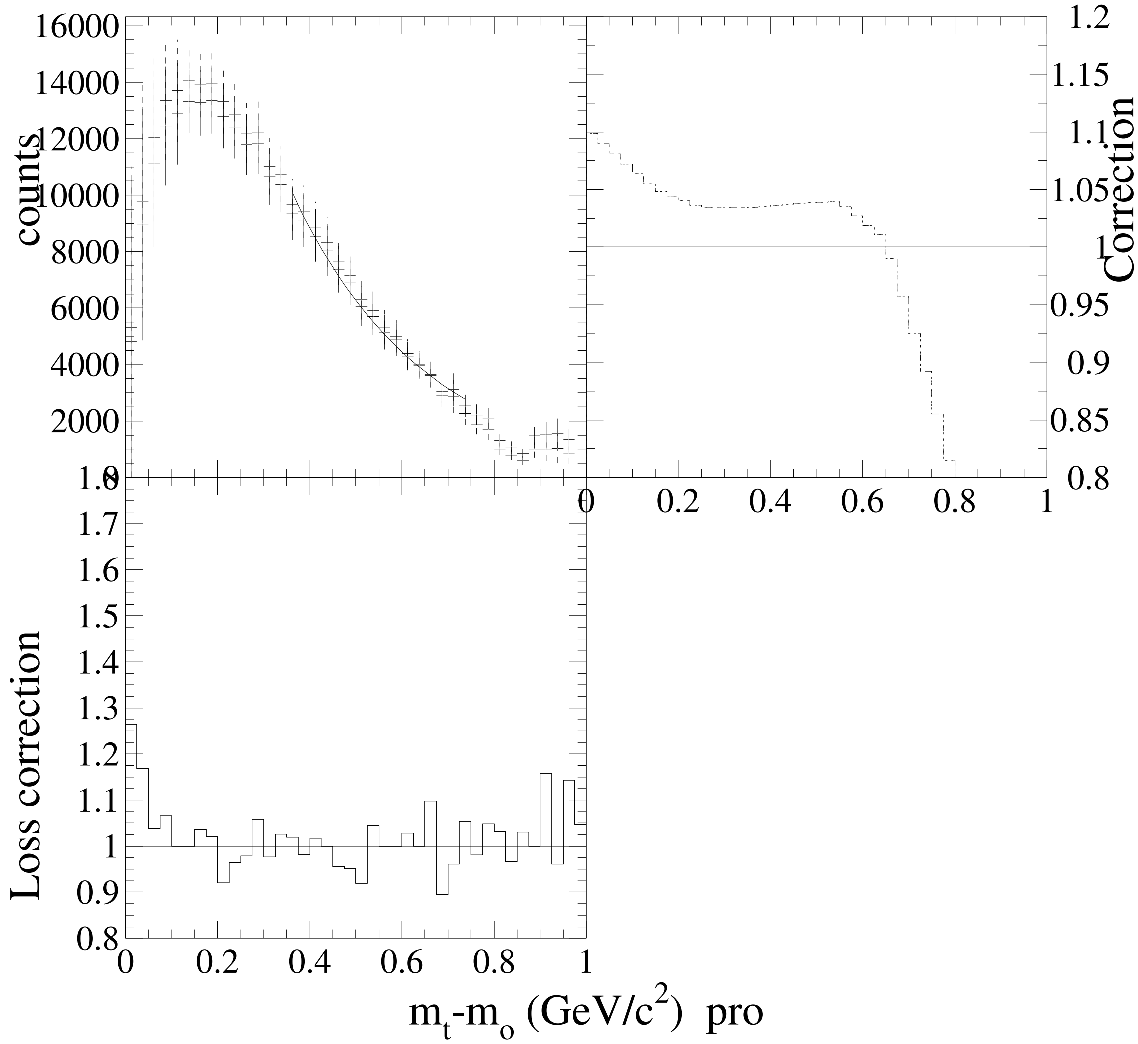

Figure A.3: 6 AGeV Protons

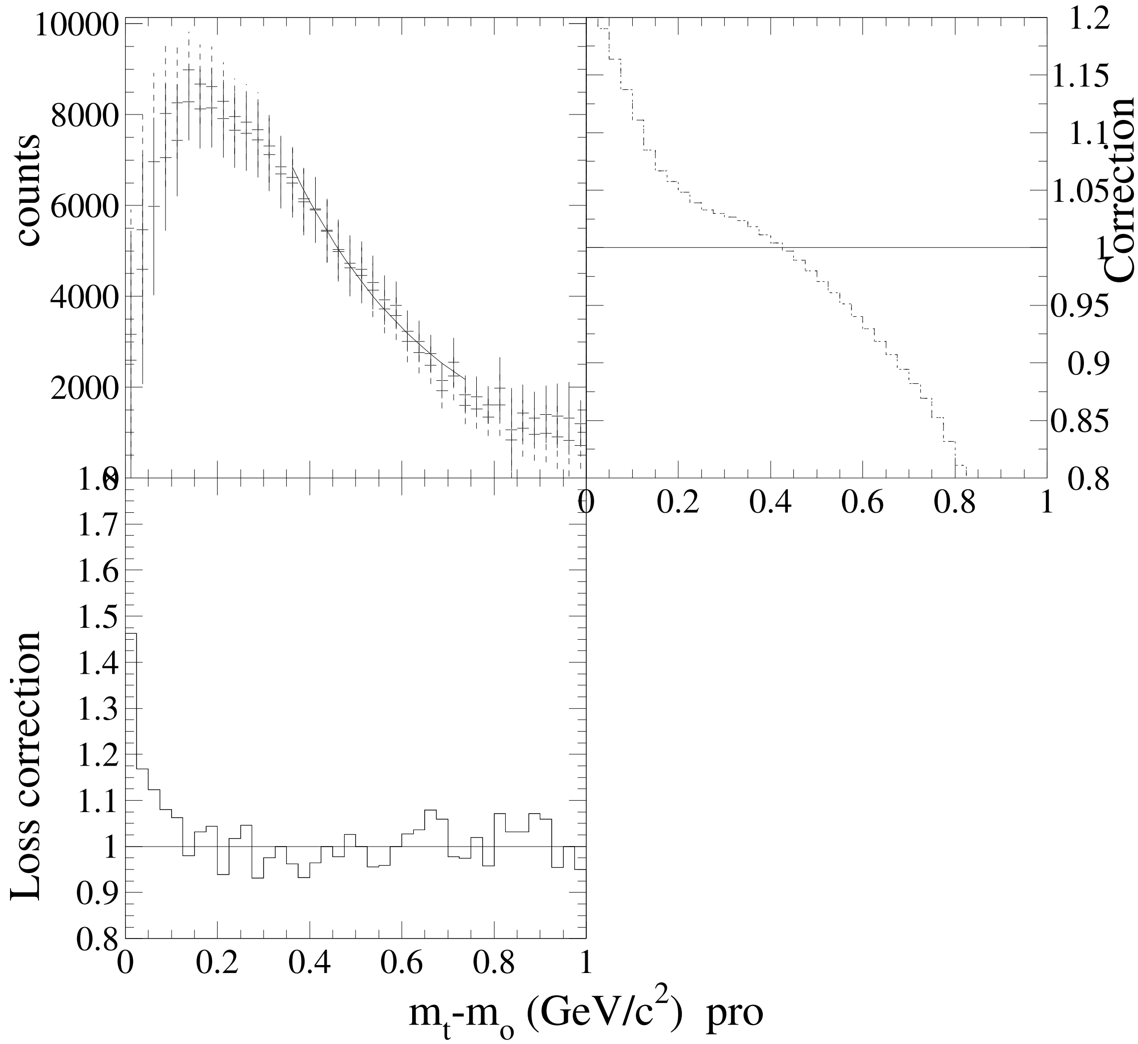

Figure A.4: 8 AGeV Protons

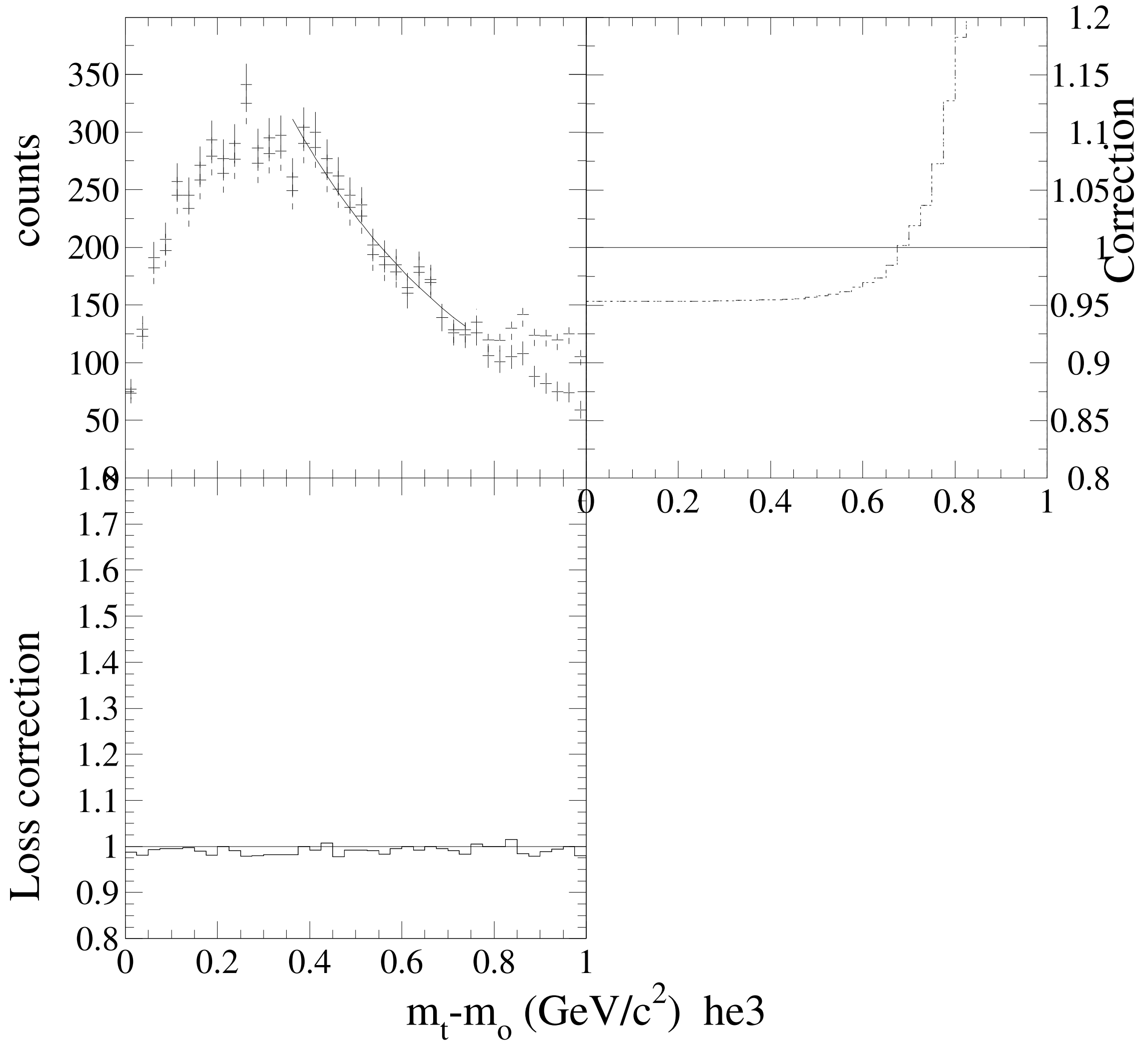

Figure A.5: 2 AGeV Helions

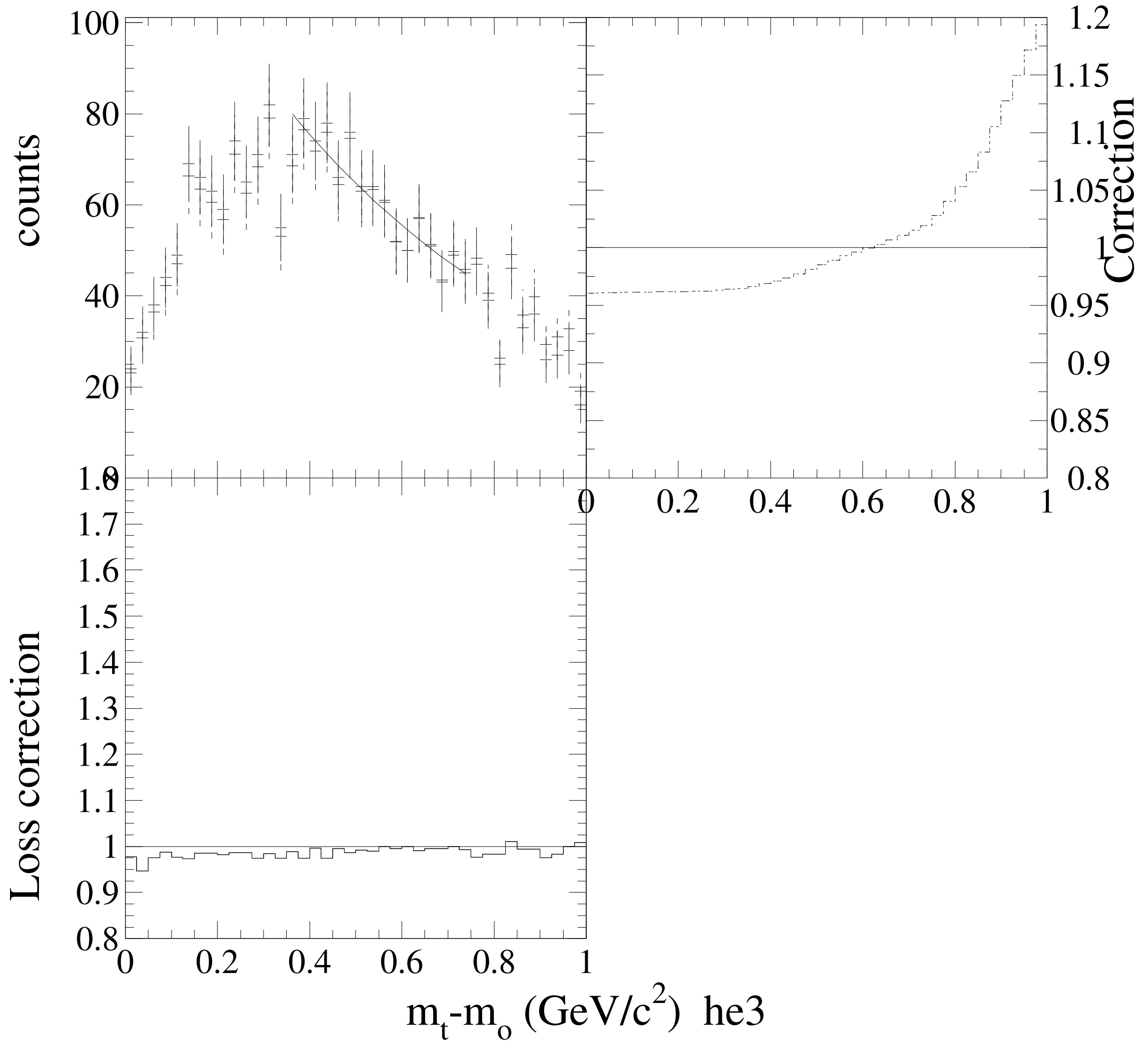

Figure A.6: 4 AGeV Helions

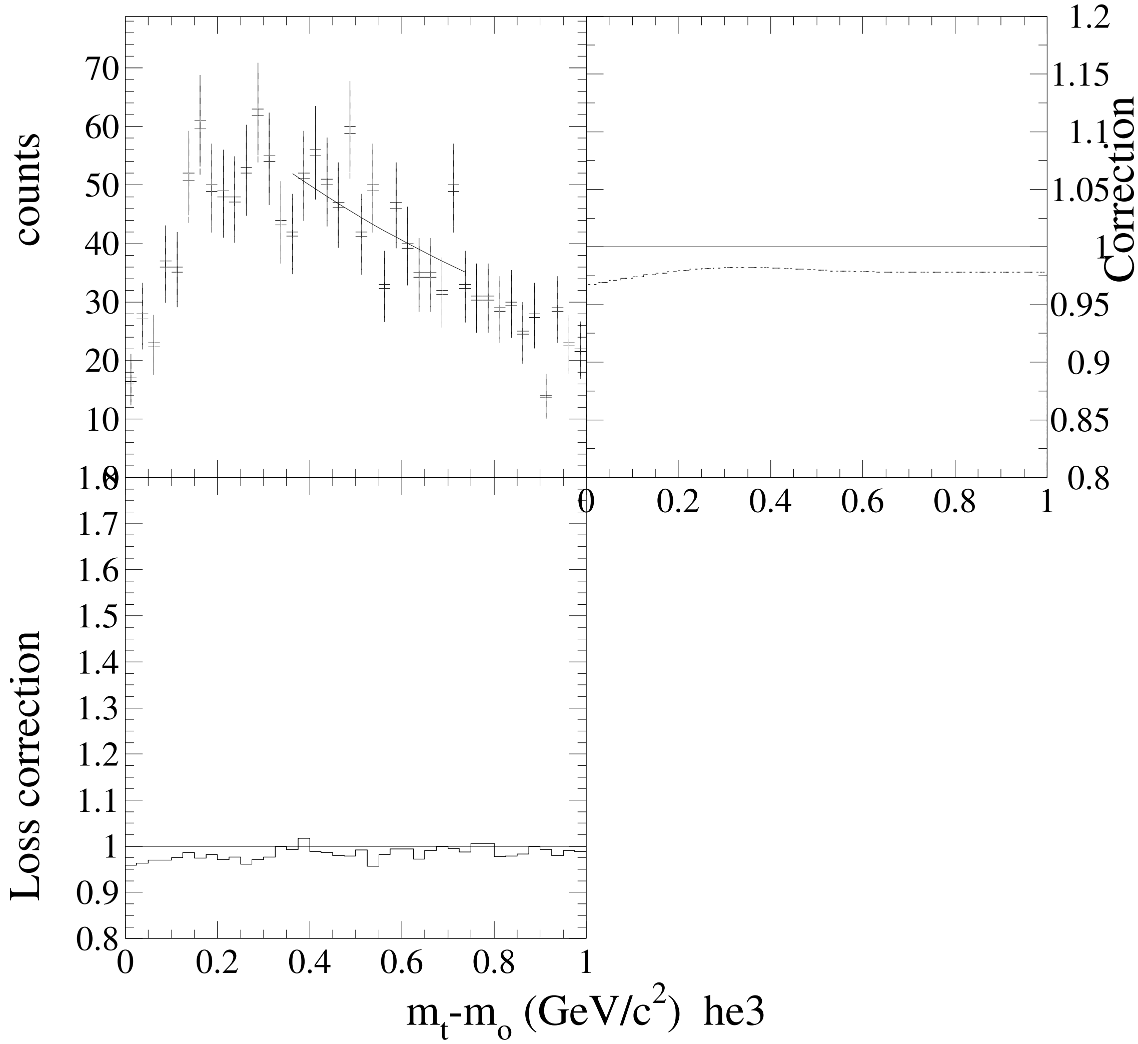

Figure A.7: 6 AGeV Helions

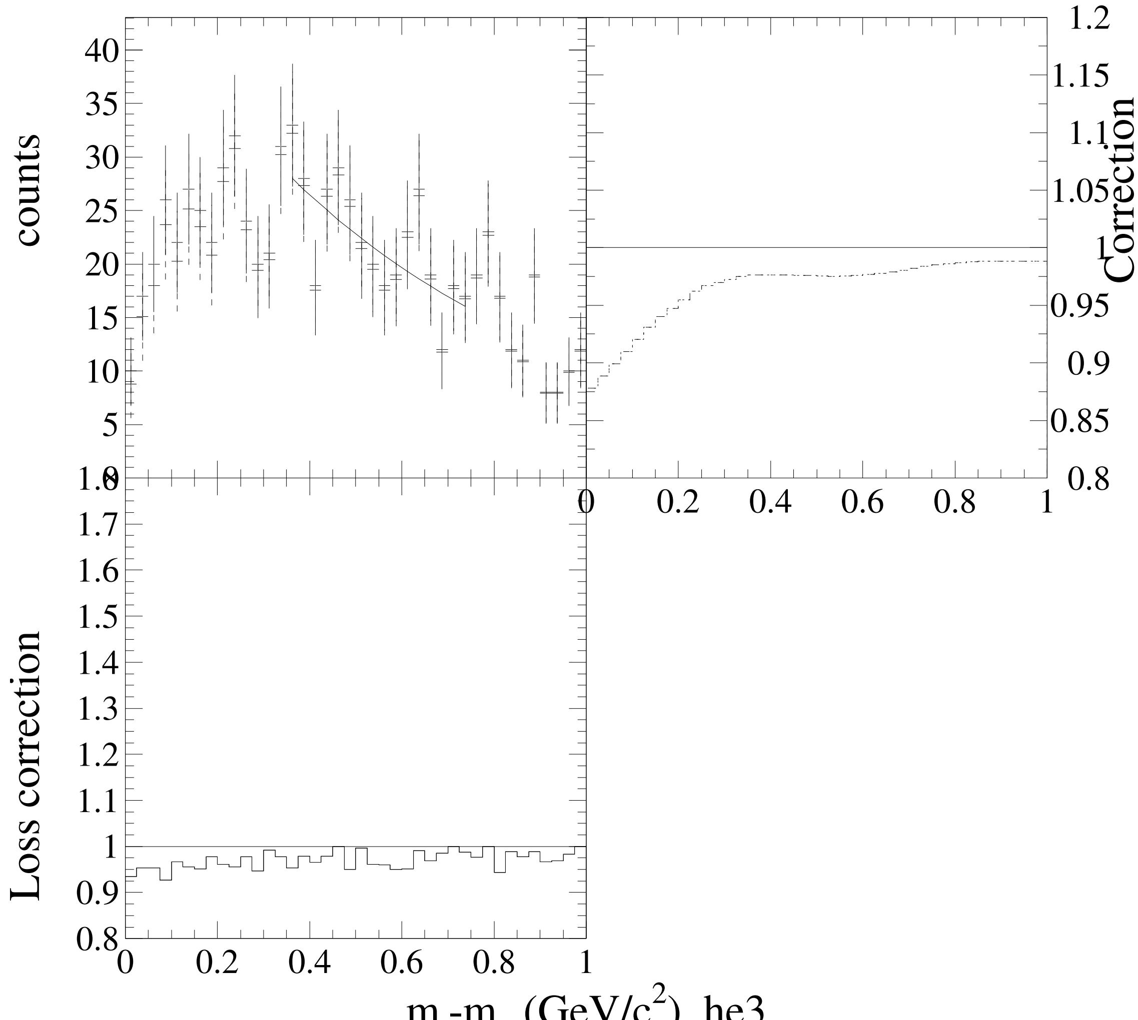

Figure A.8: 8 AGeV Helions

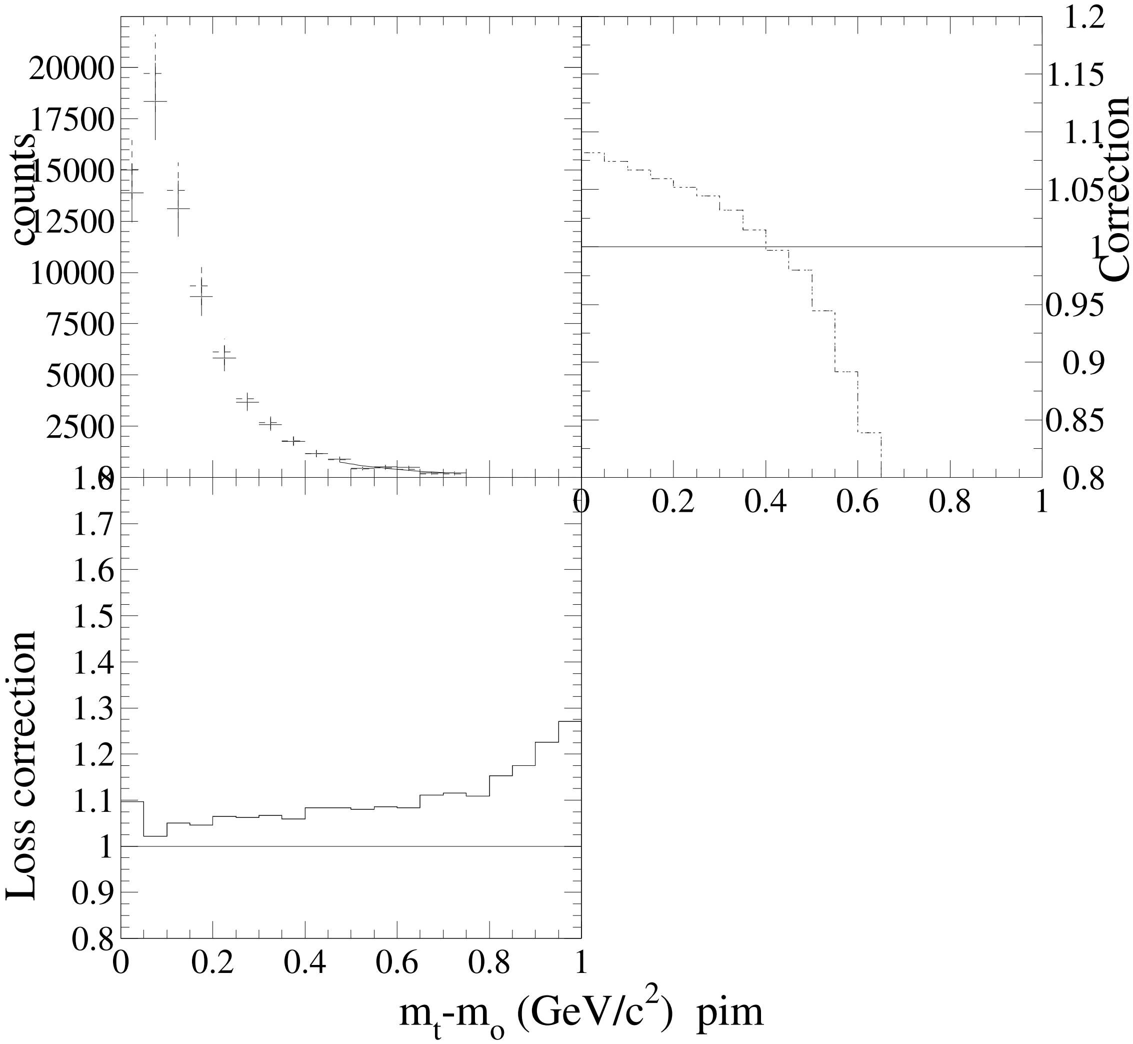

Figure A.9: 2 AGeV Negative Pions

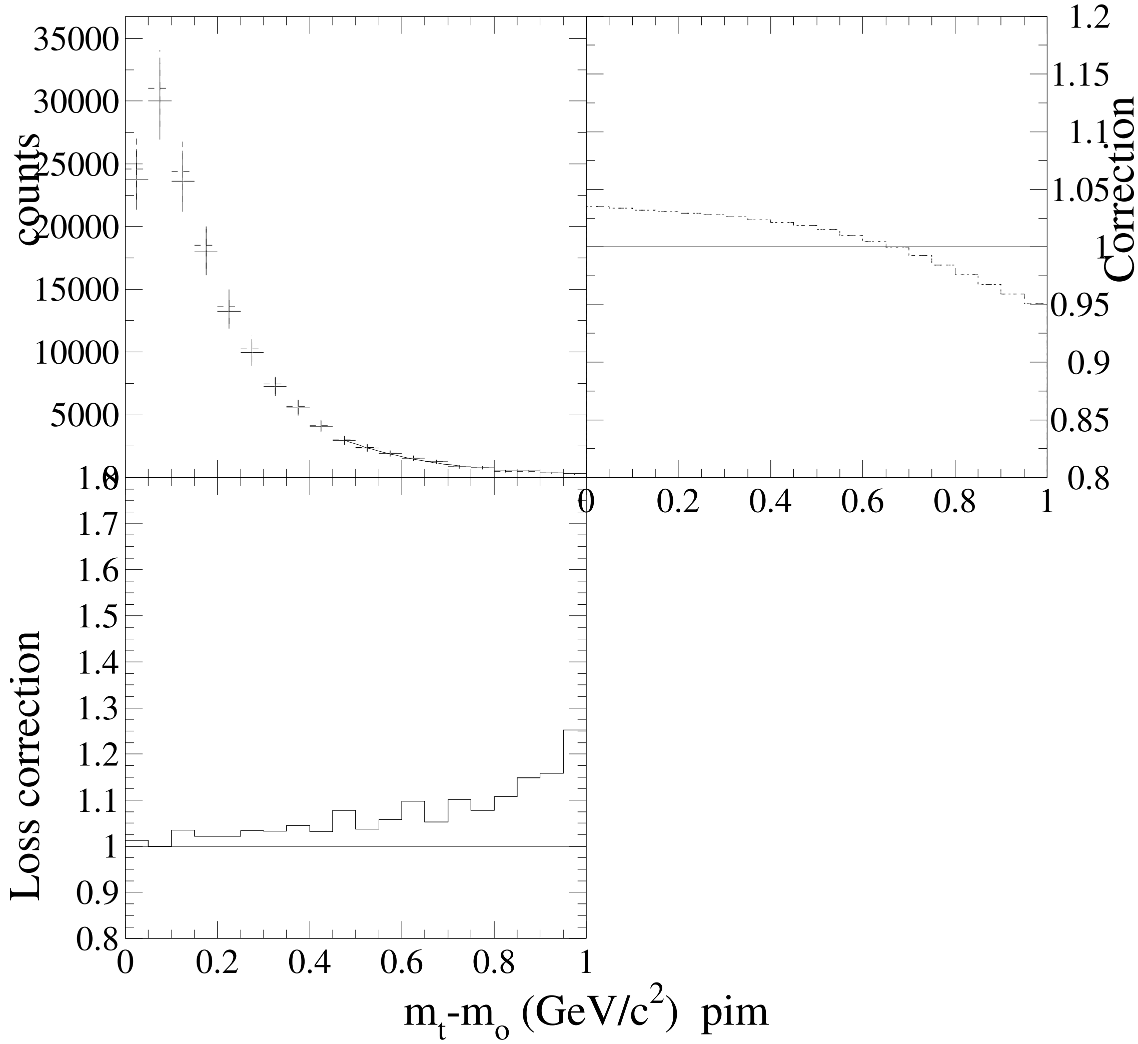

Figure A.10: 4 AGeV Negative Pions

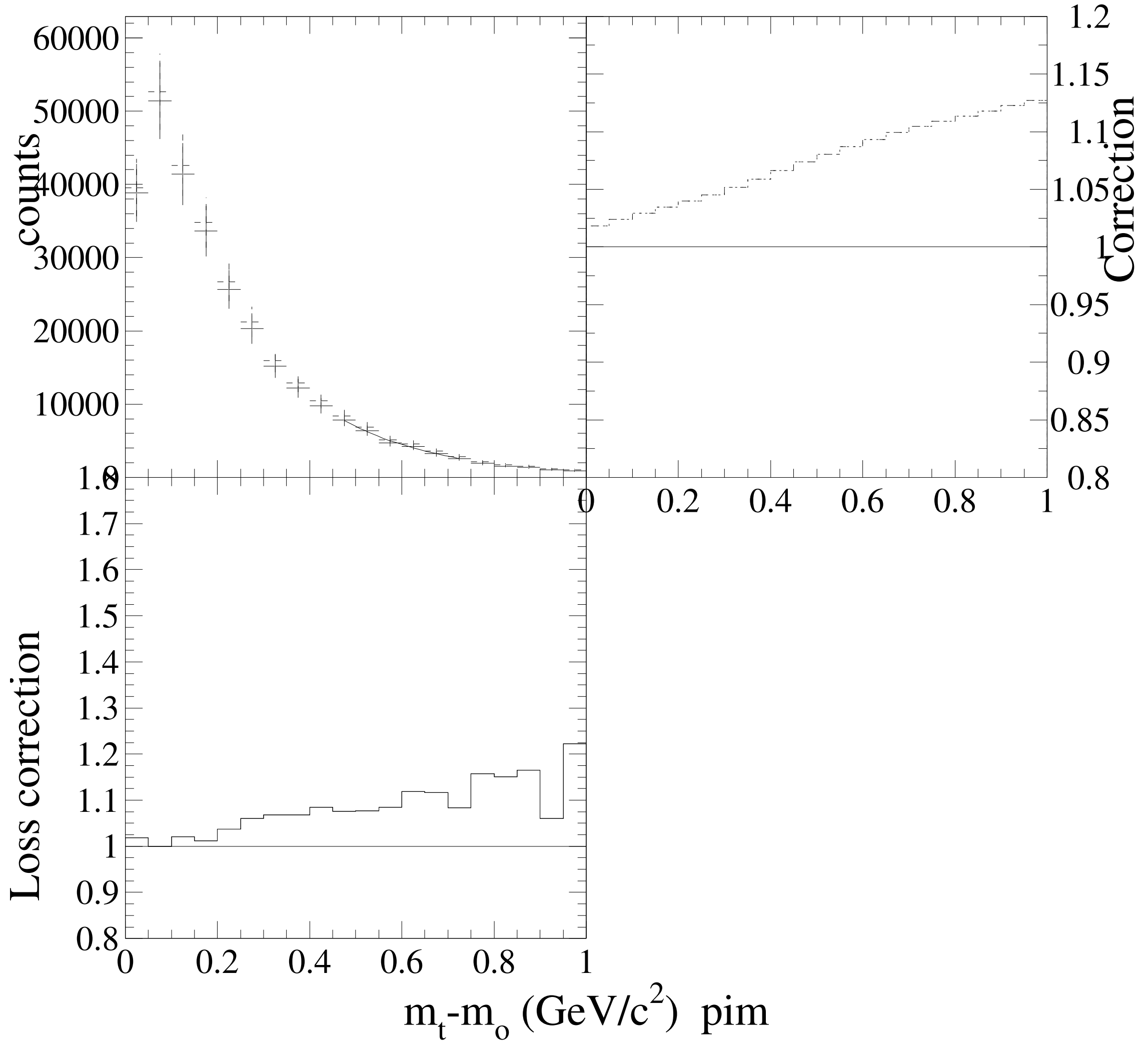

Figure A.11: 6 AGeV Negative Pions

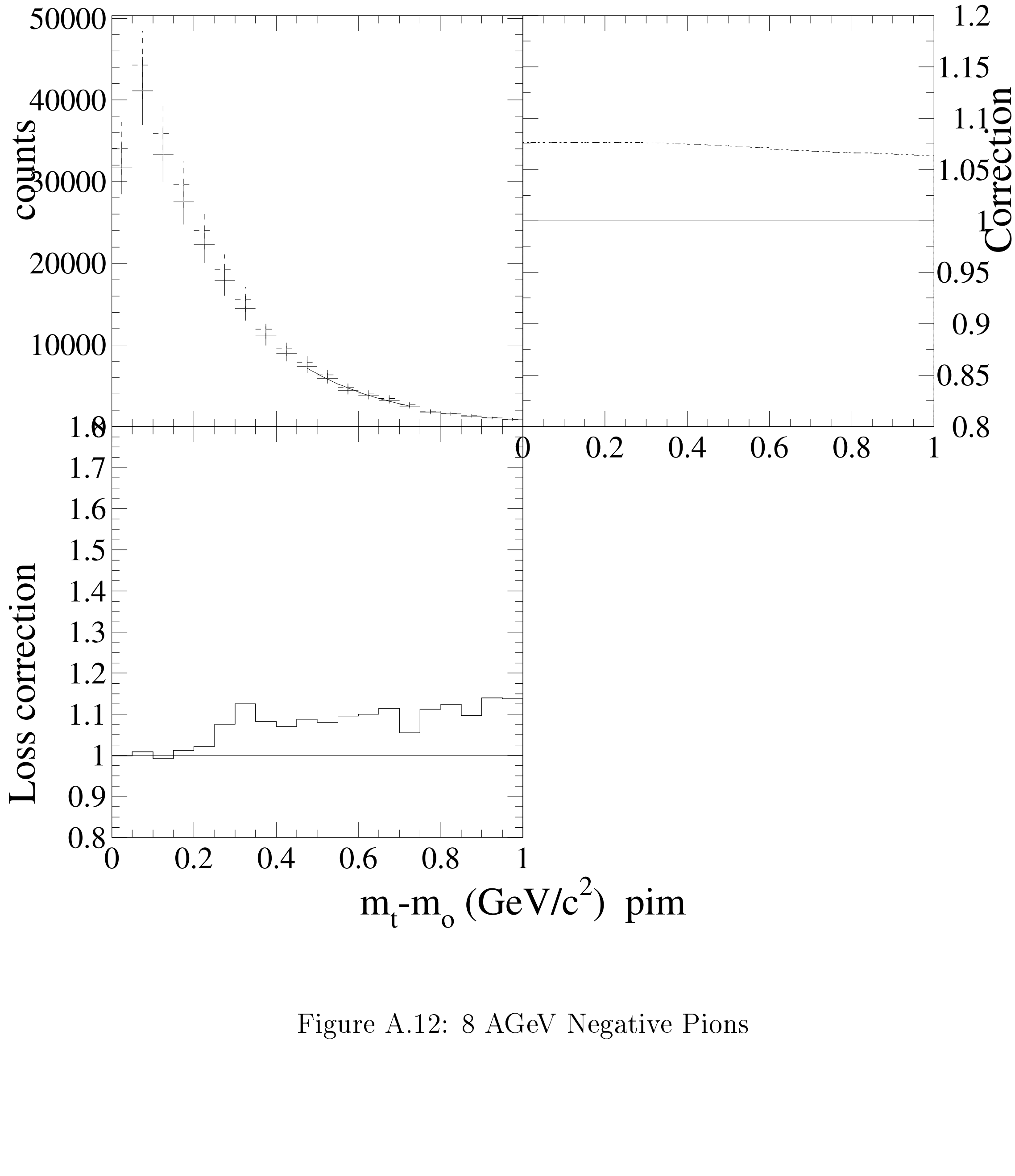

Figure A.12: 8 AGeV Negative Pions

Appendix B

Computer Farm and Monte Carlo Simulations

Running detailed simulations of the TPC detector requires a large amount of computing power. For this reason, a computer farm was constructed at UCDavis to compute the efficiency and momentum resolution of the detector and its reconstruction software. The farm consisted of 21 Hewlett Packard (HP) workstations, that are from the old PDSF computing farm located at Lawrence Berkeley National Lab (LBNL). Of the roughly 50 computers that we received, only 21 were in a condition to run, and the collection of working computers was not homogeneous. The make-up of the farm is shown in Table B.1. These RISC based computers ran the HP-UX 10.2 operating system, and the relative processing speed is directly related to the clock speed. So

	HP735	HP730	HP720
Number	10	6	5
Clock Speed	100 MHz	66 MHz	50 MHz

Table B.1: The number of computers in the farm and their speed.

for example the HP720s are half as fast as the HP735s. The equivalent number of HP735s is then 16.5 from the 21 running computers.

The computers were connected through standard Ethernet connections, and each node (computer work station) has its own IP address. One concern with this setup would be an overload of the network. It turns out that the jobs that we run spend much more time in the processing of data than moving it around. This fact is what allows this system to work without completely slowing down the network for all users. Jobs are dispatched through the Condor Batch System. One of the farm machines (izar.ucdavis.edu) runs the condor server software for the farm. This computer is responsible to look at the jobs in the queue and computers in the farm, and decide when to start a job, keep track of running jobs, and also run jobs on itself. The jobs are all submitted from a computer that is not part of the farm (rigel.ucdavis.edu), but has the software to have a queue and submit jobs. The files after processing are on Rigel from where they were submitted.

Some of the large files that are needed for this simulation would not fit on the farm or Rigel. These files are stored on zosma.ucdavis.edu, and are accessed by Rigel with NFS setup in a read-only mode. Zosma has a large (27Gb) drive that makes the storage much more manageable, and the NFS only adds a very small amount of network traffic overhead.

The process of simulation works as follows. Four tracks are simulated by GEANT to produce hits in the TPC. The effects of electrons drifting in the TPC are then simulated with a module called the slow simulator. The raw TPC data that are simulated in this way are embedded in a real event and the combination is then processed by the reconstruction software. The four tracks that were put in are then searched for in the final output, as described on page 58. The GEANT software that is used to simulate a track must follow a track through all of the detector material step by step determining how the different physical processes effect the path of the particle. Full tracking of the event with the embedded tracks adds a substantial amount of processing. The multiplicity of an event effects the time to reconstruct substantially. The total time to simulate an event with four test particles is about 62 min/event/HP735 machine for 8 AGeV data and about 23 min/event/HP735 machine for 2 AGeV.

Submitting jobs to the queue is described in detail in the Condor manual, see http://www.cs.wisc.edu/condor/. For our system **all** jobs are submitted from Rigel even though they can in principle be submitted from any machine in the farm. The reason for this is that only jobs in your local queue can be seen, and the slow simulation software is located on Rigel. This keeps the system from becoming too disorganized.

All of the files needed to submit a slow simulation job are located, for example, in the directory /scratch6/mheffner/slowsim/run1. I will explain each of these directories.

cal	This is where the calibration files are for the distortion correction (distortions to the straight line path of drifting electrons caused by misaligned electric and magnetic fields) and magnetic field.
cmd	These command files are what you submit to Condor. They contain the instructions to condor about what executable to run, what file to use for input, and where to put the output. The instructions in these files are detailed in the condor manual.
frs	This is where the input tracks are generated. All of the files are generated automatically with the *"go"* script. This script calls the program ptysim_mike that actually makes the file of tracks to embed.
input	These are the scripts that run by the cmd files. They are generated with the script "generateInput".
kumac	These are the kumacs that run the slow simulator.
log	Log files are written here.
out	Standard output from the job is written here.
ref_calib	Calibration files.

ref_kumac Calibration kumacs.

xdfoutput Simulation output. These are the product of the simulation that are analyzed to determine the efficiency.

The procedure to run a job is to set up the files above and then issue the command, condor_submit *command filename.* It is as simple as that. Some other commands of great utility are, condor_q and condor_status. They allow one to see what is in the queue and what state the farm is in, respectively.

Appendix C

Kaon Contamination

The kaon contamination of both the pions and protons is estimated in this appendix. Kaons are measured at the beam energies of this experiment by other experiments, and this appendix uses that information to estimate the kaon contamination in the spectrum measured in this work. All of the information about the kaon abundances are from reference [Ogil98]. First we start with the K^- contamination in the π^-. Figure 5 in reference [Ogil98] shows a dN/dy spectrum for K^- at 10.8 AGeV for Au+Au. The mid-rapidity for a kaon (and all other particles) in these collisions is y=1.6, but a kaon with the same momentum in the z-direction as a pion at mid-rapidity would be at y=0.66. Looking at Fig. 5 from reference [Ogil98] we can read off that the dN/dy for kaons is about 0.85. Now we need to know the dN/dy for all four energies studied 2, 4, 6, 8 AGeV. The energy dependence is not in [Ogil98], but since the K^- contamination is a small effect we can make some good approximations. We know that at 2AGeV the K^- production is subthreshold, and from Fig. 2 in reference [Ogil98] we see that the K^+ production as a function of energy is roughly linear with energy. From this information, one could roughly approximate the K^- dN/dy as a function of energy by a linear interpolation to zero at 2AGeV. The second column in Table C.1 shows the result of this interpolation.

To estimate the contamination we compare the pion dN/dy measured in E895 with that of the K^- determined above. This gives one the contamination. We see that the contamination is small so any errors in the above assumptions will have little effect on the results. We want to determine how the contamination changes as a function of p_t. There are two issues here, the relative shape of the pions and kaons and the region of crossover in the dE/dx curves. We know the shape of the pion spectrum from this work (see Fig.5.2) and the kaon spectral shape is known from the [Ogil98]. The shapes (slopes) of the K^- and the π^- are similar so the ratio of kaons to pions would not change much as a function of p_t, and therefore the percent contamination would be constant as a function of p_t. Looking at the dE/dx vs. rigidity plots we see that the kaons and pions are only crossing at larger momenta. So only the upper bins ($m_t - m_o \geq$0.8) of the pion spectra are effected. Table C.1 shows a summary of the contaminations.

Now we follow the same method to estimate the K^+ contamination in the protons.

Beam Energy	dN/dy Kaons	dN/dy Pions	% contamination
10.8 AGeV	0.85	n/a	n/a
8 AGeV	0.58	48	1.2%
6 AGeV	0.39	40	0.98%
4 AGeV	0.19	33	0.58%
2 AGeV	0	18	0

Table C.1: Percent of K^- contamination in the π^- spectrum.

Beam Energy	dN/dy Kaons	dN/dy protons	% contamination
8 AGeV	5.0	65	7.8%
6 AGeV	3.5	65	5.4%
4 AGeV	1.5	70	2.1%
2 AGeV	0.17	65	0.26%

Table C.2: Contamination of K^+ in the protons.

The contamination is larger, but we have more information to do a better job in the estimation, namely Fig. 2 from reference [Ogil98]. This figure gives us the dN/dy as a function of the beam energy. We start off again asking what rapidity kaon would contaminate the mid-rapidity protons, and this is y=2.6. Looking at Fig. 5 we see that the dN/dy spectra drops off from the peak at 8.2 to 5.5 at y=2.6. If we assume that this shape is similar for all energies, we can scale Fig. 2 by 5.5/8.2 to get the number of kaons in the protons. This is shown in Table C.2 with the proton dN/dy and the percent contamination.

Appendix D

Effect of nhits Cut

The purpose of this appendix is to describe the effects of the nhit cut on the data with respect to the momentum resolution and efficiency corrections. Both of these corrections are studied with the used of a detailed simulator embedding tracks into real events. The nhit variable is the number of hits on a track. This can vary from 7 (tracking minimum) to 128 (number of pad rows in the TPC). Figures D.1,D.2,D.3,D.4,D.5 show the momentum resolution of tracks in the TPC for different windows of the nhits variable. The obvious feature is that the momentum resolution improves with more hits on a track. This makes sense since the track is sampled more times and therefore there is less statistical error in the measurement of the curvature. The lines on the plots represent the theoretical momentum resolution for the TPC assuming a position resolution of $750\mu m$. The upper line is the resolution assuming the minimum number of hits in the window, and the lower line is the maximum number of hits in the window. The data that falls in the nhits window should fall below the two lines.

With only the momentum resolution to look at, one could incorrectly assume that we should impose a cut such that each track should have the maximum number of hits. This strict requirement would improve the momentum resolution and related distortions to the spectrum. The reason that such a cut is not made is that the efficiency of the detector worsens rapidly with an increasing nhits cut. This effect is demonstrated in Fig. D.6 and D.7; the plots are showing the efficiency correction for some rather small nhits cuts (30 and 18). One can see that the correction that is needed is larger for the spectrum cut on nhits than a spectrum including all tracks with nhits$>$7 (see Appendix A). From this investigation it was decided not to impose a nhits cut over the tracking minimum.

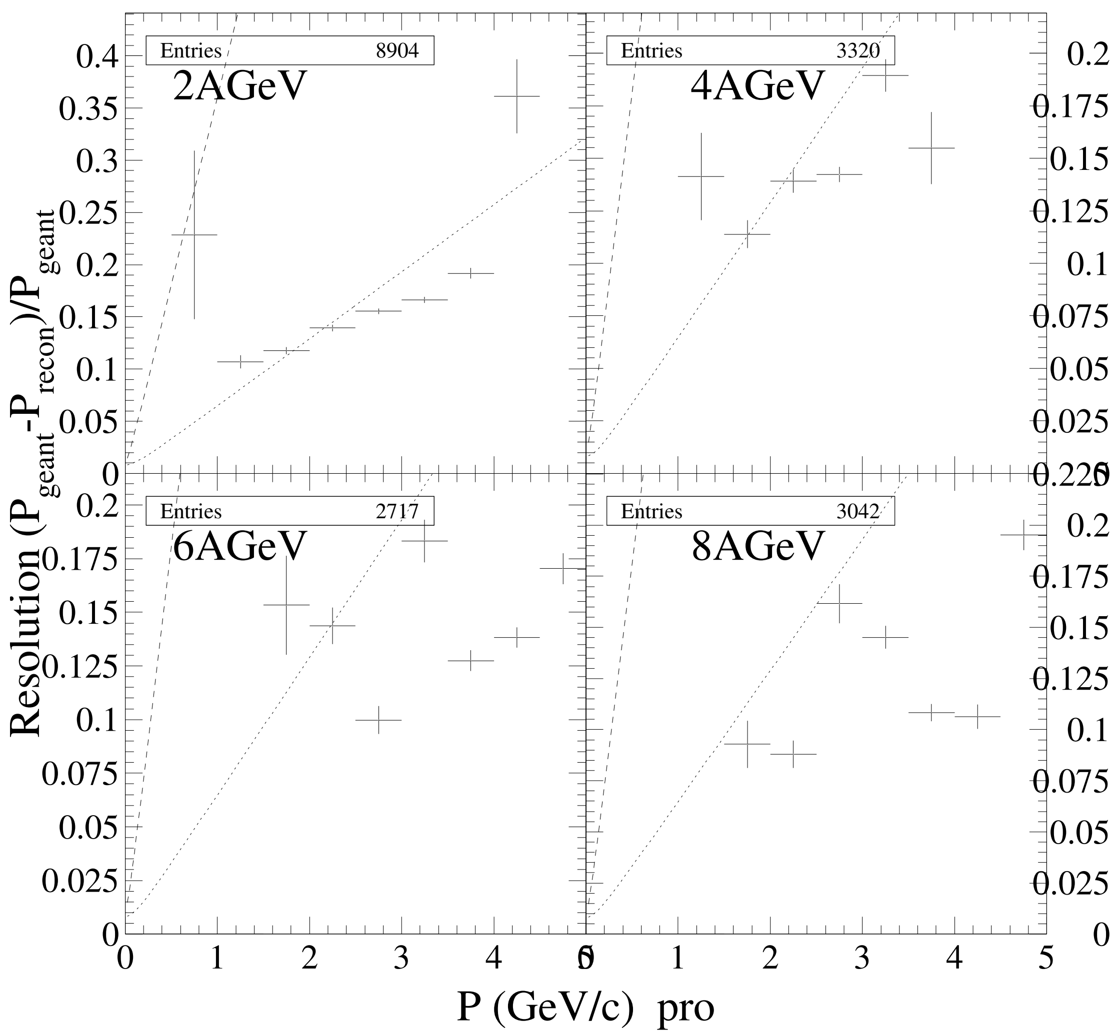

Figure D.1: Resolution for nhits cut of 15-30.

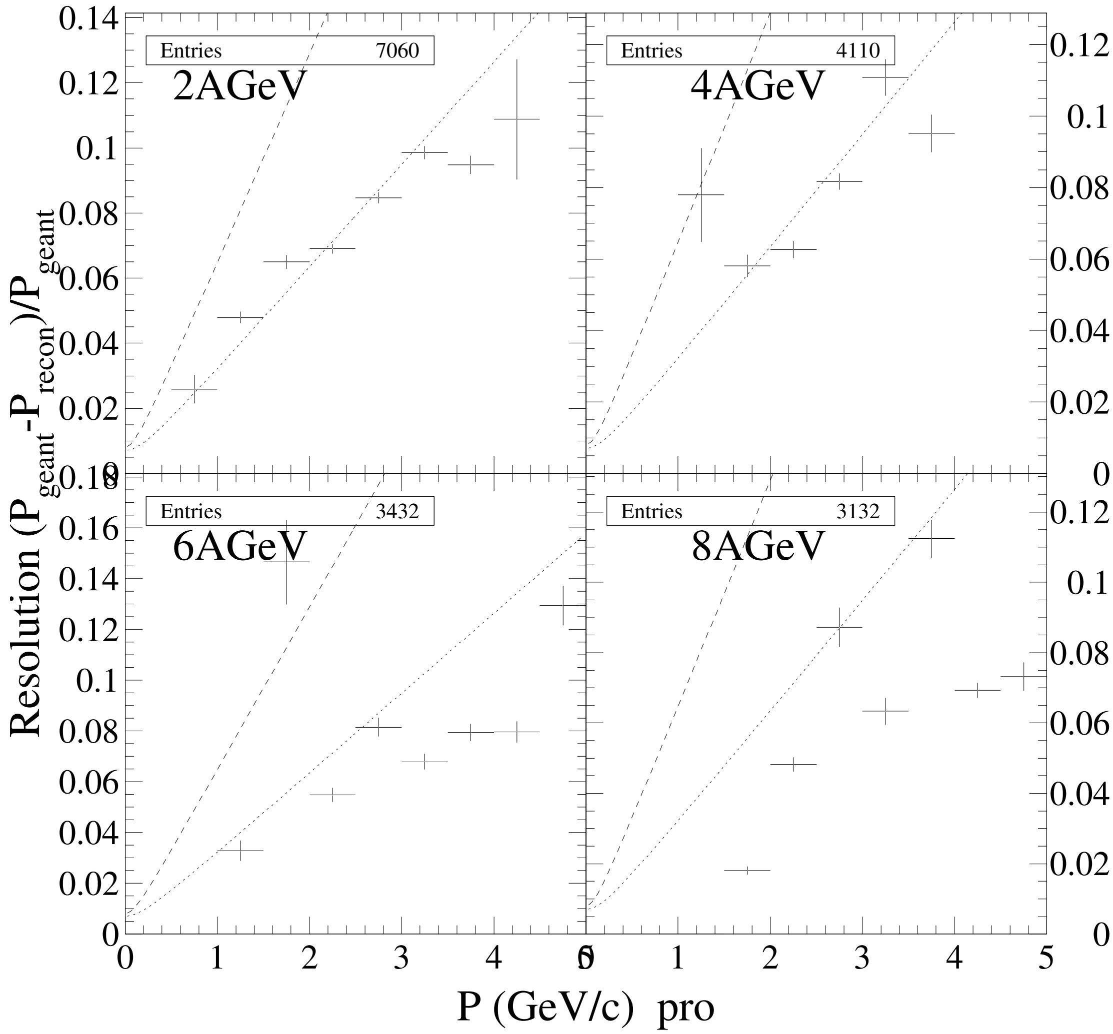

Figure D.2: Resolution for nhits cut of 30-40.

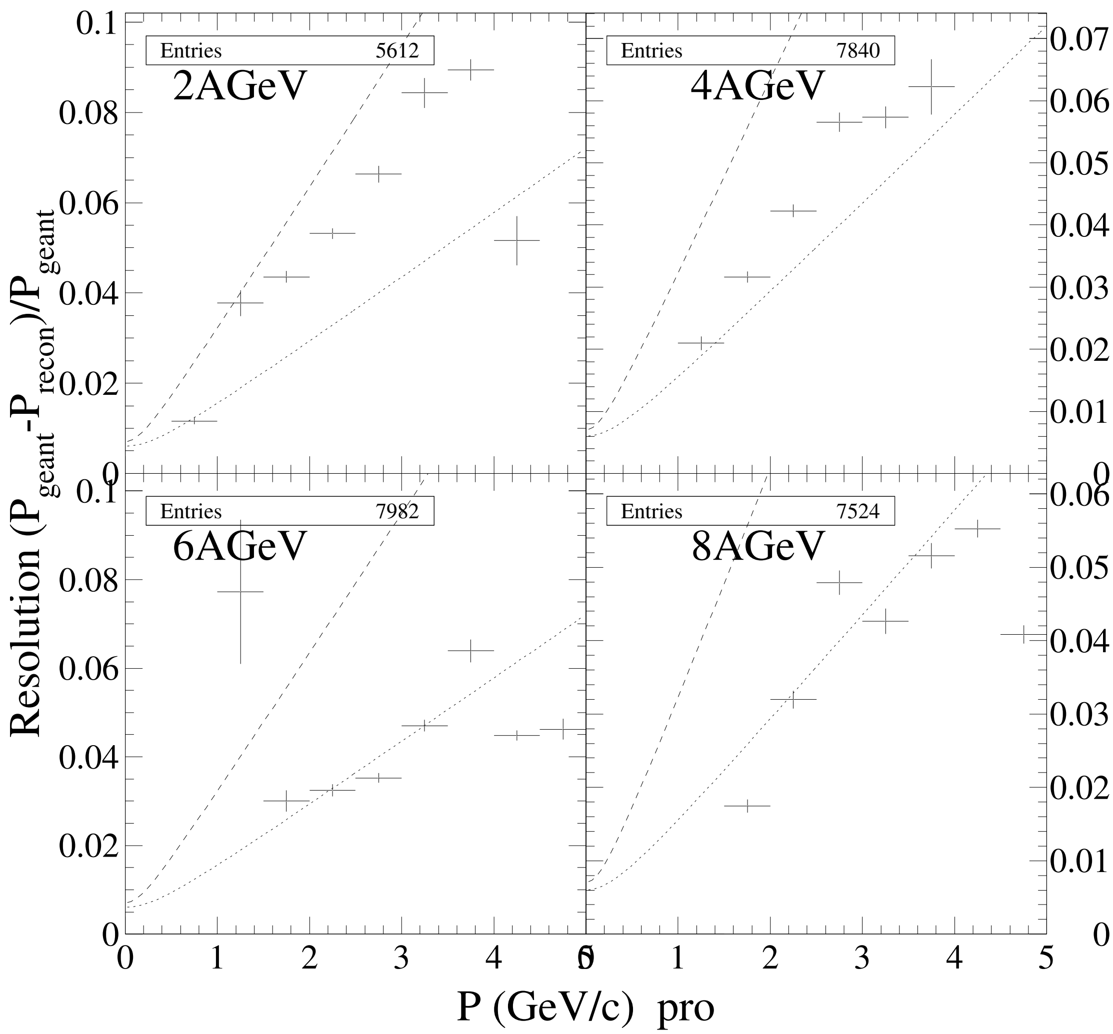

Figure D.3: Resolution for nhits cut of 40-55.

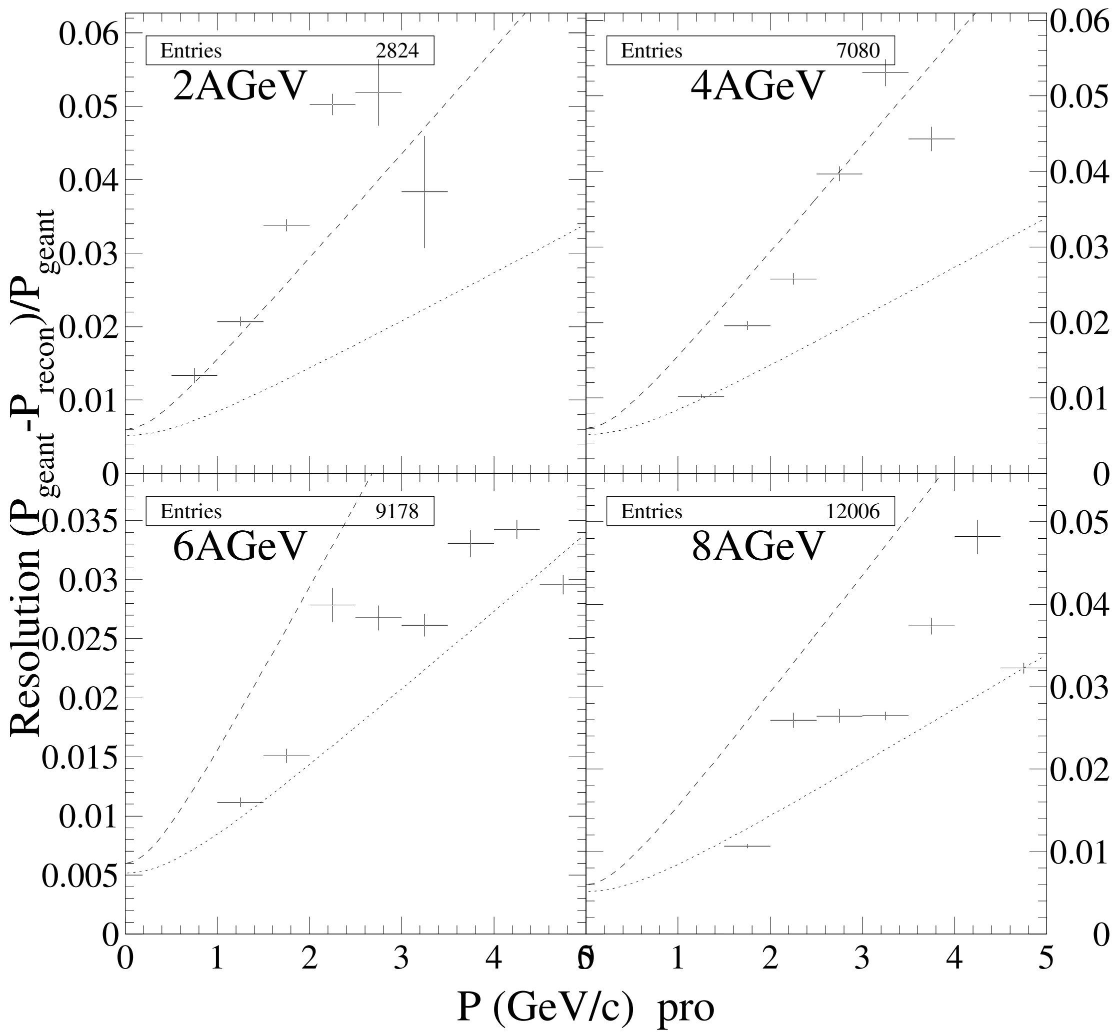

Figure D.4: Resolution for nhits cut of 55-75.

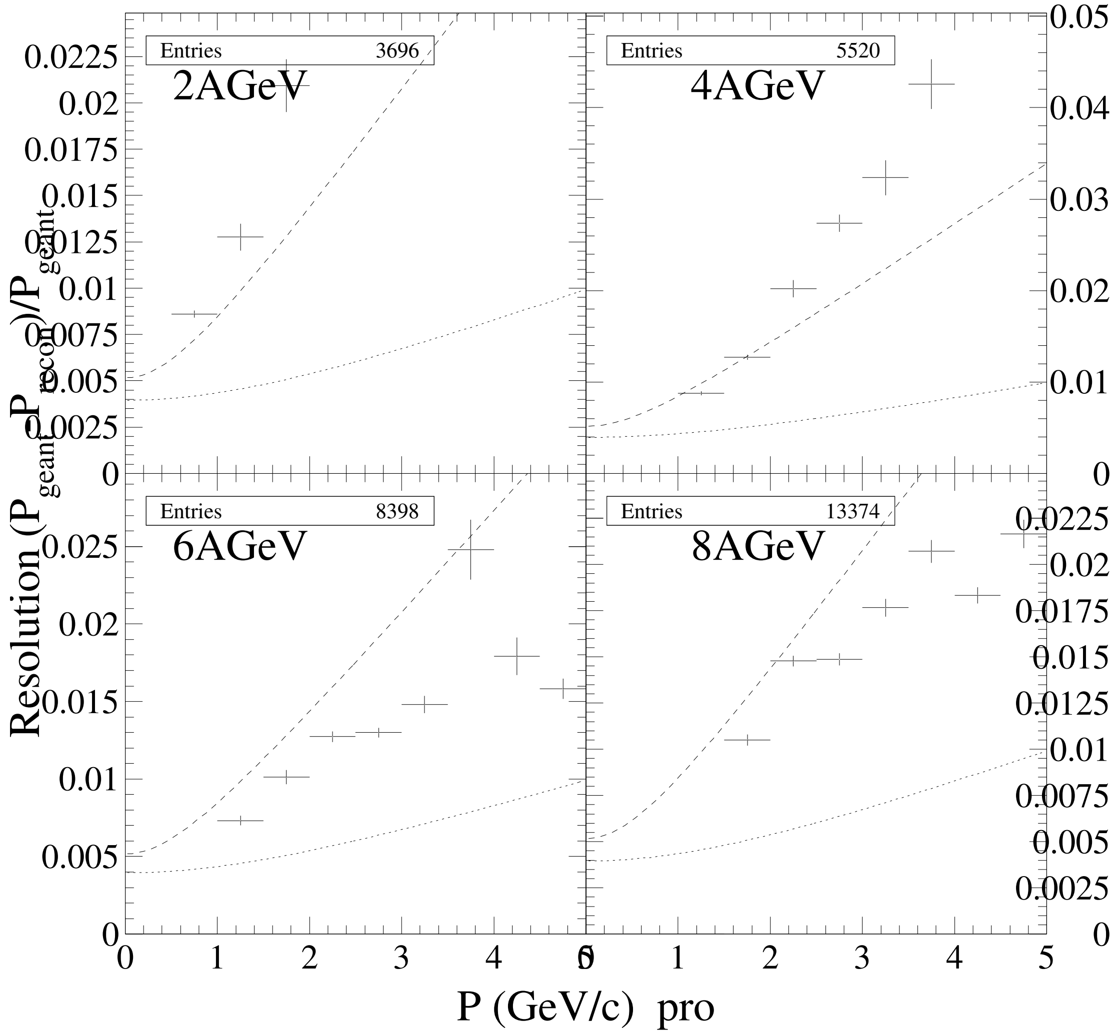

Figure D.5: Resolution for nhits cut of 75-128.

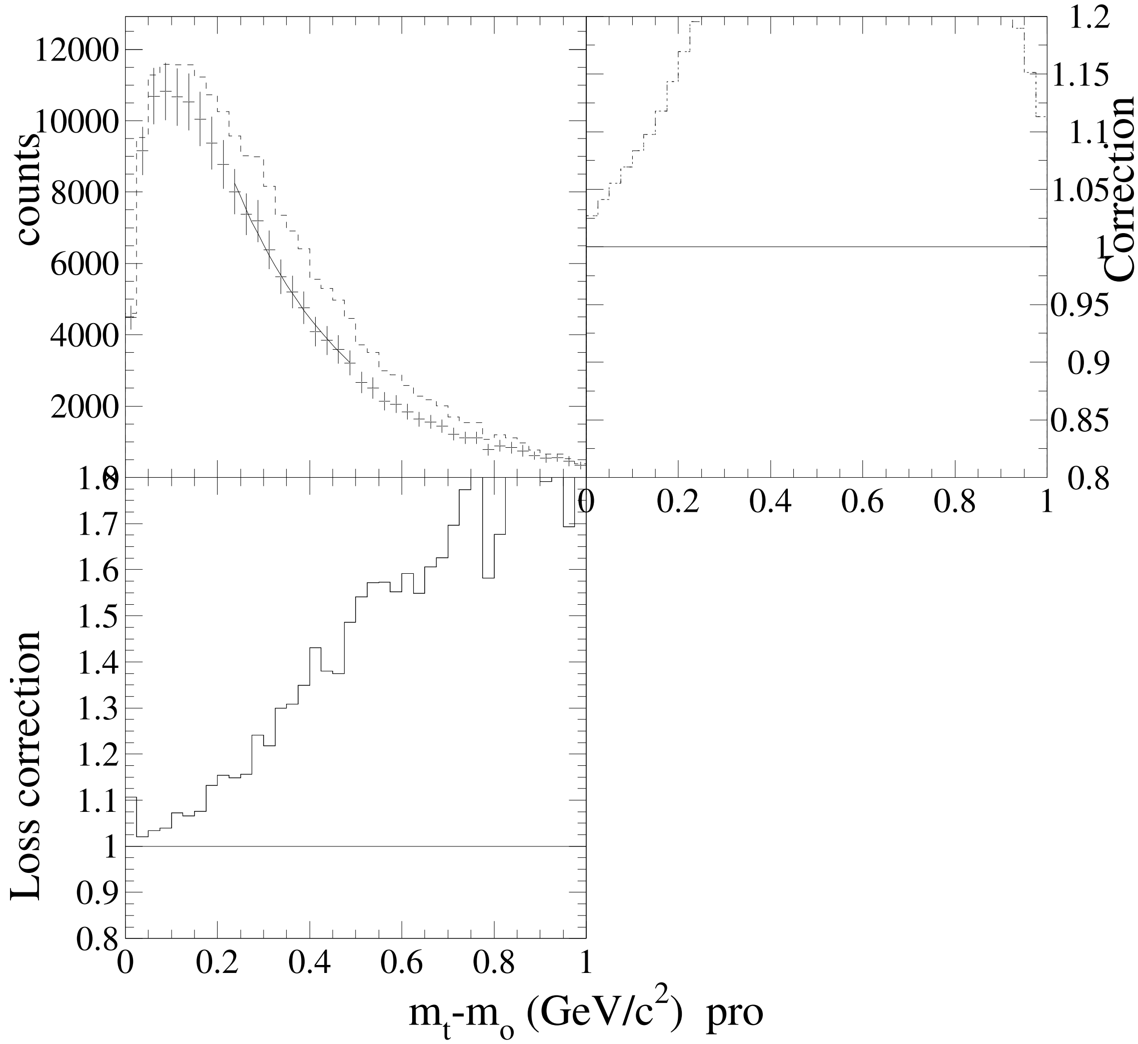

Figure D.6: Correction for a nhits cut of 30. 2 AGeV protons.

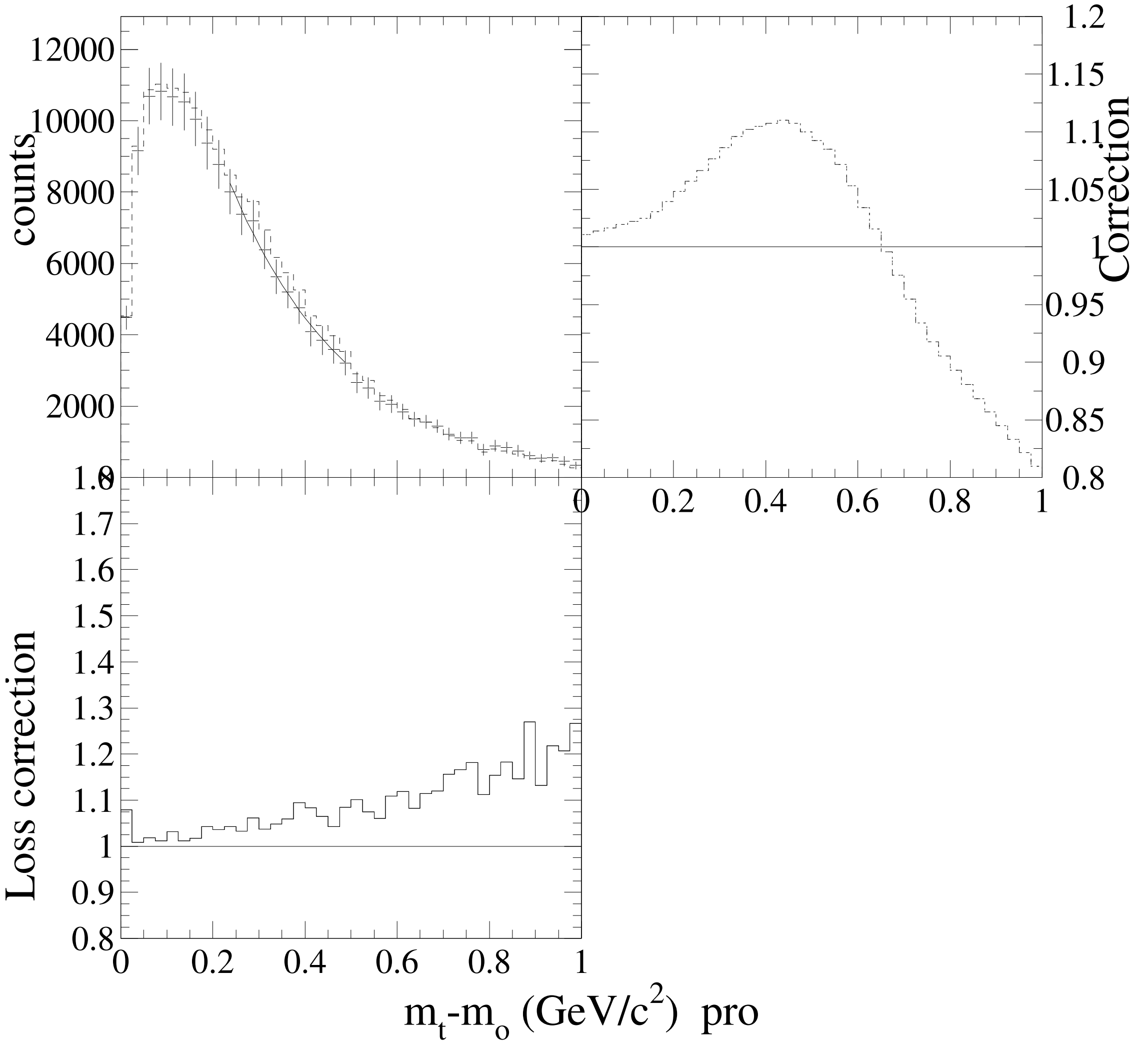

Figure D.7: Correction for a nhits cuts of 18. 2AGeV protons.

Bibliography

[Akib96] Y. Akiba *et al.*, *Particle Production in Au+Au collisions from the BNL E866*, Nuclear Physics **A610**, 139c (1996)

[Agga99] M. Aggarwal *et al.*, *Freeze-Out Parameters in Central 158 A GeV Pb+Pb Collisions*, Physical Review Letters **83**,926 (1999)

[Albe95] T. Alber *et al.*, *Transverse Energy Production in Pb+Pb Collisions at 158 GeV per Nucleon*, Physical Review Letters, **75**, 3814 (1995)

[Appe98] H. Appelshauser *et al.*, *Hadronic Expansion Dynamics in Central Pb+Pb Collisions at 158 GeV per Nucleon*, Nuclear Physics **A638**, 91c (1998)

[Ayal99] A. Ayala *et al.*, *Size of fireballs created in high energy heavy ion experiments as inferred from Coulomb distortions of pion spectra*, Physical Review **C59**, 3324 (1999)

[Barr95] J. Barrette *et al.*, *Measurement of pion enhancement at low transverse momentum...*, Physics Letters **B351**, 93 (1995)

[Barz97] H. Barz *et al.*, *Freeze-out time in ultrarelativistic heavy ion collisions from Coulomb effects in transverse pion spectra*, Physical Review **C56**,1553 (1997)

[Barz98] H. Barz *et al.*, *Coulomb effects on particle spectra in relativistic nuclear collisions*, Physical Review **C57**, 2536 (1998)

[Bear97] I.G. Bearden, *et al.*, NA44, *Collective Expansion in High Energy Heavy Ion Collisions*, Physical Review Letters, **78**, 2080 (1997)

[Belk98] M. Belkacem, *et al., Equation of State, Spectra, and Composition of Hot and Dense Infinite ...*, Physical Review **C58**, 1727 (1998)

[Bert94] G. Bertsch, *Meson Phase space Density in Heavy Ion Collisions from Interferometry*, Physical Review Letters, **72**, 2349 (1994)

[Blum93] W. Blum, L. Rolandi, *Particle Detection with Drift Chambers*, Springer-Verlag (1993)

[Bock90] R. Bock, *et al.*, *Data analysis techniques for high-energy physics experiments*, Cambridge University Press (1990)

[Chap95] S. Chapman, J. Nix, U. Heinz, *Extracting source parameters from Gaussian fits to two-particle correlations*, Physical Review **C52**, 2694 (1995)

[Cook63] B. Cook, *Lease Structure Solution of Photonuclear Yield Functions*, Nuclear Instruments and Methods, **24**, 256 (1963)

[Cser94] L.P. Csernai, *Introduction to Relativistic Heavy Ion Collisions*, John Wiley & Sons (1994)

[Daff96] F. Daffin, K. Haglin, W. Bauer, *Collective radial expansion in Au+Au reactions from 0.25 to 2 GeV/nucleon*, Physical Review **C54**, 1375 (1996)

[Dani98] P. Danielewicz *et al.*, *Disappearance of Elliptic Flow: A New Probe for the Nuclear Equation of State*, Physical Review Letters, **81**, 2438 (1998)

[Dobl99] H. Dobler, J. Sollfrank, U. Heinz, *Kinetic freeze-out and radial flow in 11.6 A GeV Au+Au collisions*, Physics Letters **B457**, 353 (1999)

[Fere99] D. Ferenc *et al.*, *Universal Pion Freeze-out Phase Space Density*, Nuclear Physics **A661**, 374 (1999)

[Fern92] R.Fernow, *Introduction to Experimental Particle Physics*, Cambridge University Press (1992)

[Hage70] R. Hagedorn, *Remarks on the Thermodynamical Model of Strong Interactions*, Nuclear Physics **B24**,93 (1970)

[Harr98] J.W. Harris, *Relativistic Heavy Ion Physics and the Relativistic Heavy Ion Collider*, lectures given at the Lake Louise Winter Institute on QCD 15-21 February, 1998, Lake Louise Alberta, Canada.

[Homb99] A. Hombach *et al.*, *Analysis of flow effects in relativistic heavy-ion collisions within the CBUU approach*, European Physical Journal **A 5**, 157 (1999)

[Hong98] B. Hong *et al.*, *Stopping and radial flow in central Ni+Ni collisions between 1 A and 2 A GeV*, Physical Review **C57**, 244 (1998)

[Jaco00] M. Jacob, U. Heinz, *A new State of Matter*, CERN Press Release Feb10,2000

[John80] M. Johnson, *Thick Target Corrections for Charged Particle Spectra*, Nuclear Instruments and Methods, **169**, 179 (1980)

[Kaha96] S. Kahana, D. Kahana, Y. Pang, T. Schlagel, *Modeling Relativistic Heavy Ion Collisions at the AGS*, Annual Reviews Nuclear and Particle Science, **46**, 31 (1996)

[Kran88] K.S. Krane, *Introductory Nuclear Physics*, John Wiley & Sons (1988)

[Laca96] R. Lacasse *et al.*, *Hadron yields and spectra in Au+Au collision at the AGS*, Nuclear Physics, **A610**, 153c (1996)

[Leo94] W.R. Leo, *Techniques for Nuclear and Particle Physics Experiments*, Springer-Verlag (1994)

[Li96] B. Li, C. Ko, *Excitation functions in central Au+Au collisions from SIS/GSI to AGS/Brookhaven*, Nuclear Physics **A601**, 457 (1996)

[Lisa00] M. Lisa *et al.*, *Bombarding Energy Dependence of pions Interferometry at the Brookhaven AGS*, Physical Review Letters, **84**, 2798 (2000)

[Lisa95] M. Lisa *et al.*, *Radial Flow in Au+Au Collisions at E=(0.25-1.15)A GeV*, Physical Review Letters, **75**, 2662, October 1995

[Liu00] H. Liu *et al.*, *Sideward Flow in Au + Au Collisions Between 2A GeV and 8A GeV*, Physical Review Letters, **84**, 5488 (2000)

[Naka91] M. Nakamura et al., *Low Power Shaper Amplifier for the EOS TPC Detector*, IEEE Trans. on Nucl. Science, **38**, 50 (1991)

[Ogil98] C. Ogilvie, *Au+Au Reactions at the AGS: Experiments E866 and E917*, Nuclear Physics **A638**, 57c (1998)

[Osad96] T. Osada et al., *What information can we obtain from the yield ratio* $\frac{\pi^-}{\pi^+}$ *in heavy-ion collisions*, Physical Review **C54,** 2167 (1996)

[Petr95] M. Petrovici *et al.*, *Cluster Formation during Expansion of Hot an Compressed...*, Physical Review Letters **74**, 5001 (1995)

[Phil62] D. Phillips, *A Technique for the Numerical...,* Ass. Comp. Mach., **9**, 84 (1962)

[Pink99] C. Pinkenburg *et al.*, *Elliptic Flow: Transition from out-of-plane to in-plane Emission in Au+Au Collisions*, Physical Review Letters, **83**, 1295 (1999)

[Rai90] G. Rai *et. al.*, *A TPC Detector for the Study of High Multiplicity Heavy Ion Collisions*, IEEE Trans. on Nucl. Science,**37**, No2, pp 56-64, April 1990

[Reis97] W.Reisdorf *et. al.*, FOPI, *Central collisions of Au on Au at 150,250, and 400 AMeV*, Nuclear Physics **A612**, 493-556 (1997)

[Ruth11] E. Rutherford, Phil. Mag. **21**, 669 (1911)

[Stac96] J. Stachel, *Tests of Thermalization in Relativistic Nucleus-Nucleus Collisions*, Nuclear Physics **A610**, 509c-522c (1996)

[Siem79] P. Siemens, J. Rasmussen, *Evidence for a Blast Wave from Compressed Nuclear Matter*, Physical Review Letters, **42**, 880, April 1979

[Sing93] C.P. Singh, *Signals of Quark-Gluon Plasma*, Physics Reports, 236, No. 3, 147-224, (1993)

[Toma99] B. Tomasik, *Reconstructing the Freeze-out State in Pb+Pb Collisions at 158 AGeV/c*, Preprint LANL server, nucl-th/9907096 (1999)

[Twom65] S. Twomey, *The Application of Numerical Filtering...*,Journal of the Franklin Institute,**279**, 95 (1965)

[Volo97] S. Voloshin, *Transverse radial expansion and directed flow*, Physical Review **C55**, 1630 (1997)

[wang95] S. Wang *et al.*, *Light Fragment Production and Power Law Behavior in Au+Au Collisions*, Physical Review Letters, **74**, 2646 (1995)

[Wein93] S. Weinberg, *The First Three Minutes*, BasicBooks (1993)

[Wong94] C. Wong, *Introduction to High-Energy Heavy-Ion Collisions*, World Scientific (1994)